5-6-2016

# Experimental Studies on Flow Field and Flame Stabilization of a Premixed Reacting Jet in Vitiated Crossflow

Jason A. Wagner
*University of Connecticut - Storrs*, jason.wagner@uconn.edu

Experimental Studies on Flow Field and Flame Stabilization of a Premixed Reacting Jet in Vitiated Crossflow

Jason Allen Wagner, PhD

University of Connecticut, 2016

The reacting jet in crossflow (JICF) configuration has been extensively studied over the past decades, due mostly in part to its relevance to practical combustion systems. Though geometrically simple, the interaction between jet and crossflow generates a complex flow field and strong mixing processes that have been shown to help reduce harmful $NO_x$ emissions exhausted from gas turbine combustors. The work presented in this dissertation examines the flow field and flame stabilization of lean and rich premixed jets injected into a hot vitiated crossflow composed of fuel-lean combustion products. Until recently, much of the reacting JICF research has focused on non-premixed configurations; the detailed study on the premixed JICF configuration here is one of the first to be conducted.

The jet was injected perpendicular to the crossflow in a rectangular duct with jet-to-crossflow momentum flux ratios ranging from 5 to 23 and jet equivalence ratios ranging from 0.8 to 1.2. For examining the premixed JICF flame and flow field behavior several different diagnostic techniques were employed, including: high speed chemiluminescence imaging, high speed particle image velocimetry (PIV), and simultaneous PIV, formaldehyde ($CH_2O$) Planar Laser Induced Fluorescence (PLIF), and hydroxyl (OH) PLIF. Laminar flame computational analyses were also conducted to further examine the flame behavior and assess the accuracy of the diagnostic methods.

The flow field behavior was compared for a non-reacting and reacting jet in vitiated crossflow. Increased dilatation caused by combustion increased the strength of the jet such that, shear layer vorticity and jet penetration were higher for the reacting jet. Power law correlations for non-reacting JICF trajectory, taken from the literature, were found to over-predict the experimental non-reacting jet

trajectories due to the strong degree of confinement present in the experimental configuration. New jet trajectory correlations were developed, to fit both the experimental non-reacting and reacting trajectory data, to account for the effects of confinement.

In the case of reacting JICF, the flame was found to have two separate stabilization points, one on either side of the jet centerline. The windward flame stabilization was characterized by three distinct behaviors: complete flame attachment, an unsteady lifted flame, and windward blowoff. The average windward flame edge was lifted for all momentum flux ratios tested and the liftoff height showed strong dependence on both momentum flux ratio and jet equivalence ratio. The leeward flame branch consistently stabilized above the jet exit. Simultaneous PLIF-PIV imaging showed that both the windward and the leeward flame branch anchored in the jet shear layer; however, for stoichiometric and rich equivalence ratios the flame surfaces away from the anchoring point were able to separate from the shear layer. High speed PIV measurements suggested that auto-ignition was the most likely stabilization mechanism for the windward flame branch, when the flame resided in the shear layer. This was further confirmed by visualization of auto-ignition kernels in the chemiluminescence and PLIF images. Premixed flame propagation was determined to be the mechanism controlling flame stabilization when the flame resided away from the shear layer. Recirculation of hot combustion products in the jet wake was thought to be the primary mechanism supporting flame stabilization along the leeward shear layer.

Computational analyses were performed to assess the use of two-dimensional dilatation for heat release marking. The presence of chemical reaction led to an increase in dilatation; however, the dilatation and heat release behavior was not consistently proportional as both temperature gradients and heat release affected the overall dilatation. Both strain-rate and dilution of jet reactants by crossflow fluid caused a decrease in the peak dilatation from the unstretched, undiluted laminar flame condition.

# Experimental Studies on Flow Field and Flame Stabilization of a Premixed Reacting Jet in Vitiated Crossflow

Jason Allen Wagner

B.S., Trinity College, **2011**

A Dissertation

Submitted in Partial Fulfillment of the

Requirements for the Degree of

Doctor of Philosophy

at the

University of Connecticut

2016

APPROVAL PAGE

Doctor of Philosophy Dissertation

Experimental Studies on Flow Field and Flame Stabilization of a
Premixed Reacting Jet in Vitiated Crossflow

Presented by

Jason Allen Wagner, B.S.

Major Advisor _____
Baki M. Cetegen

Associate Advisor _____
Michael W. Renfro

Associate Advisor _____
Chih-Jen Sung

University of Connecticut
2016

# Acknowledgements

First and foremost, I would like to thank Prof. Baki Cetegen for providing me with the opportunity to work with him for my doctoral research; I have enjoyed every part about being an experimental combustion researcher. I would like to thank both Prof. Cetegen and Prof. Michael Renfro, for the advice, guidance, and support they provided me with throughout grad school. I was truly fortunate to have such accomplished advisors. I would like to thank Prof. Jackie Sung for generously loaning several key pieces of lab equipment, without which I would not be able to produce most of the results that make up this dissertation. I would also like to thank Prof. Sung, Prof. Tianfeng Lu, and Prof. Xinyu Zhao for their support as my advisory committee members.

I would like to thank the all members of the Cetegen lab, Bikram, James, George, and Sayan, for their help with this accomplishment. I believe that most of my combustion knowledge was gained through our countless lengthy discussions in the lab, and for that I am grateful. I would also like to thank the members of the Renfro lab for their help in the lab and frequent comic relief.

I would like to acknowledge UTC Pratt and Whitney for project funding support. I would also like to acknowledge Tom Mealy for his help with experimental design and machining; his assistance was crucial for implementing all the different rig design changes that occurred over the last five years.

My most sincere gratitude goes to my parents, Doreen and Craig. Their continued love and support has kept me motivated through all my academic endeavors.

The final acknowledgement is for Ashley. I am so grateful for all her advice, patience, and love the past five years. Her support and companionship kept me inspired and ultimately made this thesis possible.

# Table of Contents

# List of Tables

# List of Figures

# CHAPTER ONE:

# 1. Introduction

### Introduction

In the past several decades, experimental research on reacting Jet-In-Cross Flow (JICF) has been conducted primarily for non-premixed systems where the jet fluid is pure fuel or oxidizer. Understanding of such flow configurations has been vital for the development of current combustion technologies such as the GE Twin Annular Premixed Swirler (TAPS) and Rich-Burn, Quick-Quench, Lean-Burn (RQL) combustors [1], [2]. In these practical combustors, the JICF has played a key role in reducing the formation of harmful $NO_x$ pollutants. However, stricter regulations on acceptable pollutant emission levels are being put in place, and as a result new technologies must be developed to meet these new emission standards.

Currently, engineers are investigating the feasibility of developing combustors that operate at lean, premixed conditions [3]. Control over the stoichiometry in the combustor is important, as it allows for increased control over the pollutant emissions formation throughout the combustor. Conceptually, lean premixed combustion systems offer advantages in terms of pollutant emissions including soot, however, concerns exist in the safety and reliability of operating a combustor at lean, premixed conditions. Flame flashback, blowoff, and acoustic instabilities can arise with lean, premixed (LPM) combustion. Additionally, in practical applications, air entering the combustor is highly heated such that auto-ignition in the premixed injector can occur. The experiment presented in this paper is a novel configuration, in which a premixed jet is injected into a cross flow composed of the hot products of fuel-lean combustion. The interaction of the premixed jet with hot crossflow generates a highly complex

turbulent reacting flow field, and so to properly understand and study this system, knowledge of general JICF behavior, turbulent premixed reacting flows, and auto-ignition is required.

In this dissertation results from an in-depth analysis of the flow field and flame stabilization behavior for premixed reacting jet in a vitiated crossflow will be provided. The premixed JICF has been studied experimentally through use of advanced optical diagnostic techniques including, high speed chemiluminescence imaging, high speed particle image velocimetry (PIV), and simultaneous PIV, hydroxyl (OH) Planar Laser Induced Fluorescence (PLIF), formaldehyde ($CH_2O$) PLIF. The diagnostics employed allowed for visualization of flame structure, flame location, and flame-flow field interactions. The effects of jet equivalence ratio $\phi_j$ and jet-to-crossflow momentum flux ratio ($J$) on flame behavior were examined. The most significant experimental efforts were devoted to understanding of the underlying flame stabilization mechanism(s). Additionally, the effect of lateral confinement on the JICF flow field was studied, as JICF applications in practical combustors are often constrained by space requirements. To aid in interpretation of the experimental results, numerical simulations were also performed. The laminar flame simulations provided necessary insight into premixed flame propagation, auto-ignition, and flame extinction behaviors.

The remainder of the Introduction section will include a brief review of the physics of non-reacting JICF (1.1), an explanation of premixed flames (1.2) and auto-ignition (1.3), a brief review of up-to-date reacting JICF research (1.4), and a description on the utilization of simultaneous $OH/CH_2O$ PLIF imaging in reacting flows (1.5).

### 1.1 Non-Reacting Jets-In-Crossflow

Non-reacting JICF research has been conducted for the past several decades, which has led to the understanding of key physics in the highly complex flowfield. Several review papers have been published on the comprehensive non-reacting JICF research [4], [5]. In general, the non-reacting JICF

flow field is characterized by four dominant mixing structures, as shown in Fig. 1.1: the horseshoe vortex system, the jet shear layer vortices, the wake vortices, and the counter-rotating vortex pair (CVP) [6]. The horseshoe vortex system forms upstream of the jet exit and wraps around the main jet column. Because the jet acts as an obstacle to the crossflow, an adverse pressure gradient is created just upstream of the jet. This strong pressure gradient causes the crossflow boundary layer flow approaching the jet to separate and roll up. Advection by the crossflow pulls the vortex around the jet column creating the horseshoe like appearance, as pictured in Fig. 1.1 [6], [7]. The jet shear layer vortices are found in the jet-crossflow boundary, most noticeably along the windward shear layer. The behavior of these vortices is often compared with Kelvin-Helmholtz instability. The upright wake vortices appear as tornado-like vortices that stretch from the bottom wall to the main jet column, downstream of the jet exit. Through various smoke injection studies, Fric and Roshko [6] were able to visualize the wake vortices, and concluded that wake vortices result from entrainment of the crossflow boundary layer by the downstream region of the jet. Both the jet shear layer vortices and wake vortices are the primary mechanisms responsible for crossflow entrainment in the jet nearfield.

The CVP is responsible for a majority of the jet in crossflow mixing, specifically in the downstream region. The CVP forms as a result of the impulse that the jet imparts on the crossflow. The initial formation of the CVP is highly correlated with the jet shear layer behavior in the jet nearfield. As a result, the formation of the CVP is also linked with the efficiency of the jet near field mixing. The CVP structure continues to grow along the jet trajectory until it is the dominating flow structure downstream [6].

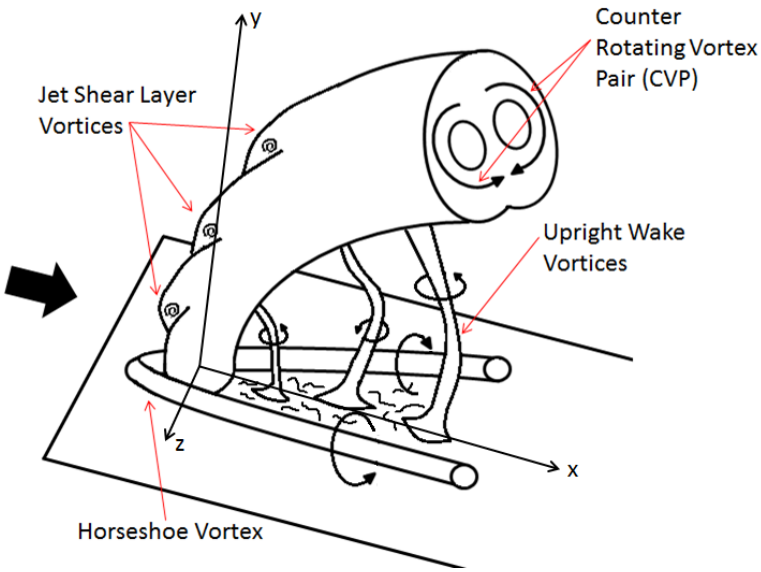


**Fig. 1.1: Four main flow structures observed in non-reacting JICF, adapted from [8].**

The primary parameter that has been used to characterize different behavior observed in non-reacting JICF experiments is the jet-to-crossflow momentum flux ratio, *J*:

$$J = \frac{\rho_j V_j^2}{\rho_\infty U_\infty^2} \qquad (1)$$

The jet fluid density is represented by $\rho_j$, the crossflow density is represented by $\rho_\infty$, and the jet and crossflow velocity are represented by $V_j$ and $U_\infty$, respectively. In flows where the jet and the crossflow mixtures have equivalent density, the jet-to-crossflow velocity ratio becomes the controlling parameter.

From non-reacting JICF experiments, correlations for the trajectories of maximum jet velocity, temperature maxima and minima, as well as other scalars have been developed. The most common correlation for describing jet trajectory was developed by Pratte and Baines [9], who found that the jet trajectory is a function of *J* and the jet diameter, *d*:

$$\frac{y}{\sqrt{J}d} = A\left(\frac{x}{\sqrt{J}d}\right)^{B} \qquad (2)$$

where *x* and *y* are the coordinates along the crossflow and jet directions, respectively, as shown in Fig. 1.1. In their experiment, Pratte and Baines [9] found that the values for A and B were 2.05 and 0.28 respectively, for *J* ranging from 25 to 1225; however, values of A and B reported in the literature can vary over the range of $1.2 < A < 2.6$ and $0.28 < B < 0.34$ [10]. Scatter in the values of the constants can be attributed to differences in the jet exit velocity profile, crossflow boundary layer behavior, and definitions used for the jet trajectory (i.e. jet center streamline, velocity maxima, scalar concentrations). Kamotani and Greber [11] proposed another correlation after finding that the value for A was also a function of *J*. Their correlation takes the form,

$$\frac{y}{\sqrt{J}d} = a\sqrt{J}^{c}\left(\frac{x}{\sqrt{J}d}\right)^{b} \qquad (3)$$

where a, b, and c are constants that depend on whether the velocity or concentration maxima is used to define trajectory. Kamotani and Greber [12] also studied the effect of confinement on jet trajectory for a single non-reacting jet in crossflow. In these experiments the velocity and temperature jet trajectories were compared for JICF configurations with no opposing wall, and an opposing wall providing lateral confinement to the jet penetration. It was found that the jet trajectory was relatively insensitive to opposing wall location for $J < 20$ and was only slightly affected for $J > 70$, when the jet collided into the opposing wall. In the experiment, lateral confinement was varied from 16 jet diameters down to 8 jet diameters. In addition, at the high momentum ratios, upstream jet flow recirculation was observed near the opposing wall.

## 1.2 Premixed Flames

An important first step in understanding the behavior of the premixed reacting JICF is to have a strong background in premixed flame behavior. In this section, a brief review on premixed flame theory is presented. The review will be limited such that it will focus only on the background information most pertinent to the premixed JICF experiment.

Understanding premixed flames starts with a look at structure of a one dimensional unstretched, laminar premixed flame, as pictured in Fig 1.2. The axial profiles of reactant concentration ($Y_{reactants}$), temperature, and heat release were computed for an ethylene-air mixture (equivalence ratio, $\phi$=1.2) using CHEMKIN-PRO 1-D PREMIX code [13], with the USCII mechanism [14]. In Fig. 1.2, two separate regions are highlighted, namely the preheat region and reaction zone. The preheat region is dominated by both heat and mass diffusion [15], with thickness denoted $\delta_D^0$. Mass diffusion is driven by the gradient of reactant concentration generated as a result of the consumption of reactants by the chemical reaction. Similarly, the heat diffusion is driven by temperature gradients generated as a result of the temperature increase due to reaction. A formulation for laminar thermal diffusion thickness was developed by Law [15] and in its simplest form is described as,

$$\delta_T^0 = \frac{T_b - T_u}{\left(dT/dx\right)_{max}} \qquad (4)$$

where, $T_u$ and $T_b$ represent the unburned mixture and the burned mixture temperatures, respectively.

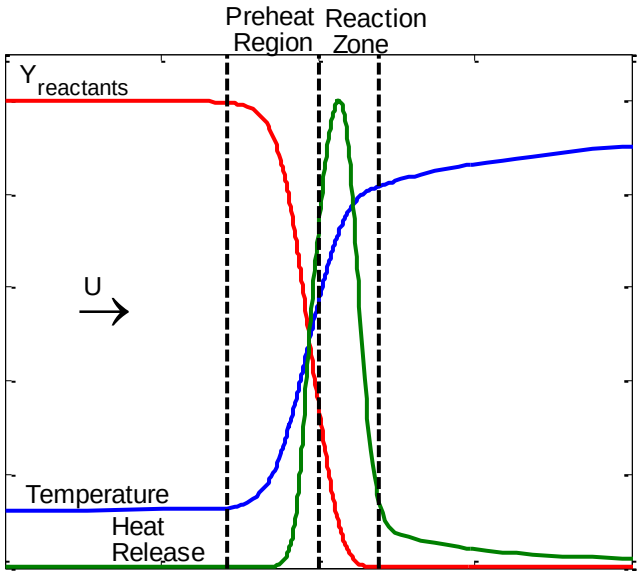


**Fig. 1.2: Axial profile of laminar premixed flame structure for an ethylene-air mixture (ϕ = 1.2) computed from CHEMKIN 1-D PREMIX simulation.**

The preheat zone is followed by the reaction zone, where the bulk of heat production occurs. The reaction zone is typically much thinner than the preheat zone, and it is the region in which reaction rates peak and the reactant concentration rapidly depletes. The thickness of the reaction zone is denoted $\delta_R^0$. The gradients of temperature and species are very large in the thin reaction region, and the gradients become the driving-forces that allow the flame to be self-sustaining. If the flame in Fig. 1.2 is fixed in a stationary reference frame, it is known that the unburned reactants approach the adiabatic, unstretched, laminar flame, at the laminar flame speed denoted $S_L^0$. For hydrocarbon flames, values for $S_L^0$ are typically on the order of 1-100 cm/sec [15].

In most practical situations, laminar flames are rarely adiabatic and unstretched. Non-adiabatic flames can result from a combination of radiative heat loss to the surrounding environment, conductive heat loss to the recant and product streams, and tangential conduction along the flame front. Non-uniformities in the flow field are primarily responsible for stretching the flame. In the limit where the

flame is much thinner than the hydrodynamic length scale of the accompanying flow, the flame can be treated as a single propagating surface ($\delta_D = 0$). The flame stretch for the condition where $\delta_D = 0$ is referred to as hydrodynamic flame stretch. Velocity gradients tangential to the flame surface cause the flame surface to change, and effectively alter the flame surface area. The flame surface is also affected by gradients in normal velocity, as the flame must adjust its position to achieve dynamic balance between its local flame speed $s_u$ and the flow velocity normal to the flame surface.

In the case in which the preheat zone and reaction zone thicknesses are considered, gradients in normal and tangential velocity can affect the transport of energy and species to and from the flame. By affecting the heat loss and mass flux, the burning intensity is also affected. This example of stretch is referred to as flame stretch [16]. The hydrodynamic stretch and flame stretch are ultimately coupled, as the former affects the stretch intensity within the flame surface, while the latter affects the propagating speed of the hydrodynamic flame surface.

Mathematically, stretch rate is defined as,

$$\kappa = \frac{1}{\delta A_f}\frac{D(\delta A_f)}{Dt} = \left(-\hat{n}\cdot(\hat{n}\cdot\nabla)\vec{u}_f + \nabla\cdot\vec{u}_f\right) + s_u\nabla\cdot\hat{n} \qquad (5)$$

where $\delta A_f$ is the area of a flame surface element, $\hat{n}$ is the flame surface normal pointing towards the reactants, $\vec{u}_f$ is the velocity field vector at the flame surface, and $s_u$ is the propagation speed of the flame surface element [17]. In eq. (5) the terms on the right hand side in parenthesis represent the tangential strain-rate that the flow exerts on the flame surface. Often times it is desired to compute this aero-dynamic strain-rate $\kappa_a$, from experimental data, and therefore a simpler expression for calculating this term has been developed,

$$\kappa_a = \left(-\hat{n}\cdot(\hat{n}\cdot\nabla)\vec{u}_f + \nabla\cdot\vec{u}_f\right) = \left(\delta_{ij} - n_{ij}n_{ij}\right)S_{ij} \qquad (6)$$

where $\delta_{ij}$ is the Kronecker delta function, $n_{ij}$ is the flame surface normal, and $S_{ij}$ is the local fluid-dynamic strain-rate tensor.

The second term on the right hand side of eq. (5) (not in parenthesis) represents the flame stretch-rate due to curvature of the flame. More specifically, this term represents the change in flame surface area due to the curved flame surface propagating normally to itself. This termed is represented by the variable $\kappa_c$, (*C* is for curvature) and can be simply rewritten as,

$$\kappa_c = s_u C \qquad (7)$$

The flame surface normal points towards the reactants and the curvature is defined as $\nabla \cdot \hat{n}$, so it follows that $C > 0$ when the flame is convex to the reactants and $C < 0$ when concave to the reactants. Positive curvature (and positive flame stretch) is associated with an increasing flame surface area, while negative curvature (and negative flame stretch) is associated with a decreasing flame surface area. Characterization of flame stretch becomes an increasingly important in turbulent premixed flows, where velocity gradients are high, causing increased aerodynamic strain-rate and flame surface wrinkling [18].

### 1.3 Auto-Ignition

One of the complexities involved with the premixed JICF experiment presented in this dissertation is the hot, vitiated crossflow. In gas turbines, flow recirculation of combustion products is often employed to assist in the continuous ignition of incoming reactants [19], [20]. Depending on the configuration of the combustor the temperature of the products at the fresh reactant injection location can vary. In the experiment presented here, the temperature of the vitiated crossflow was 1500K, which was high enough to provide for auto-ignition. Depending on the application, auto-ignition can be desired or can be something to avoid. In either instance, characterization of the auto-ignition behavior is critical to ensure safe system operability.

It is difficult to find a simple definition for auto-ignition; instead, it is more feasible to describe the typical auto-ignition process. Auto-ignition begins with the mild consumption of reactants and slight increase in mixture temperature. At these moderate temperature conditions, concentrations of pre-ignition species peak [21]. For hydrocarbon fuels, $CH_2O$ is one of the most commonly used species for identification of pre-ignition behavior [22]. The second phase of the auto-ignition process is associated with thermal runaway and rapid destruction of the pre-ignition and reactant species. The final phase of auto-ignition is also associated with the rapid formation of OH; it is for this reason that simultaneous OH PLIF and $CH_2O$ imaging techniques are often employed to study auto-ignition behavior [22]. In reacting flow fields auto-ignition behavior is often observed as localized kernels (independent of any stabilized flame) [22]–[25]. In the case of the premixed jet in vitiated crossflow, kernel formation can occur as a result of jet reactants mixing with the hot, vitiated crossflow prior to combustion. The kernel size and structure can vary depending on a number of flow conditions, however turbulence in particular has been shown to have a significant effect on ignition kernel structure [26].

Simulations using a homogenous reactor configuration have shown that there is an ideal mixture fraction, the most reactive mixture fraction, in which auto-ignition time is the fastest for a given fuel and oxidizer mixture [27]. In most configurations either the oxidizer is heated, or recirculation of hot combustion products is employed, to provide energy necessary for auto-ignition. From these simulations it has been observed that there is a mixture fraction, denoted the most reactive mixture fraction, at which the ignition delay time reaches a minimum. For configurations in which the oxidizer is hot and the fuel is cold, the most reactive mixture fraction is most often leaner than the stoichiometric mixture fraction [27].

The effect of turbulence on auto-ignition behavior can vary, depending on the turbulent conditions. Weak turbulence can aid auto-ignition, as the mixing between reactants and hot stream (e.g.,

oxidizer, vitiated products) is increased relative to a laminar flow. The faster mixing ultimately increases the rate at which auto-ignition occurs in the flow. On the other hand, high turbulence can inhibit auto-ignition. High scalar dissipation rate, associated with highly turbulent flows, can lead to excessive heat loss (or loss of radical species) during the initial phase of auto-ignition and prevent the auto-ignition process from completing [26].

Turbulence can also change the structure of the ignition kernel. Figure 1.3, taken from Im et al. [26], shows the auto-ignition behavior for an $H_2$-$O_2$ non-premixed system under weak turbulence. At this weak turbulence condition Fig. 1.3(a), auto-ignition occurs across the most reactive mixture fraction in the form of a single auto-ignition kernel. Under higher turbulence Fig. 1.3(b) auto-ignition still occurs along the most reactive mixture fraction; however, there is no longer a continuous ignition kernel but instead, there are several independent kernels that appear in the flowfield. The highly turbulent flow field leads to localized regions of high scalar dissipation which in turn, leads to more isolated auto-ignition kernels.

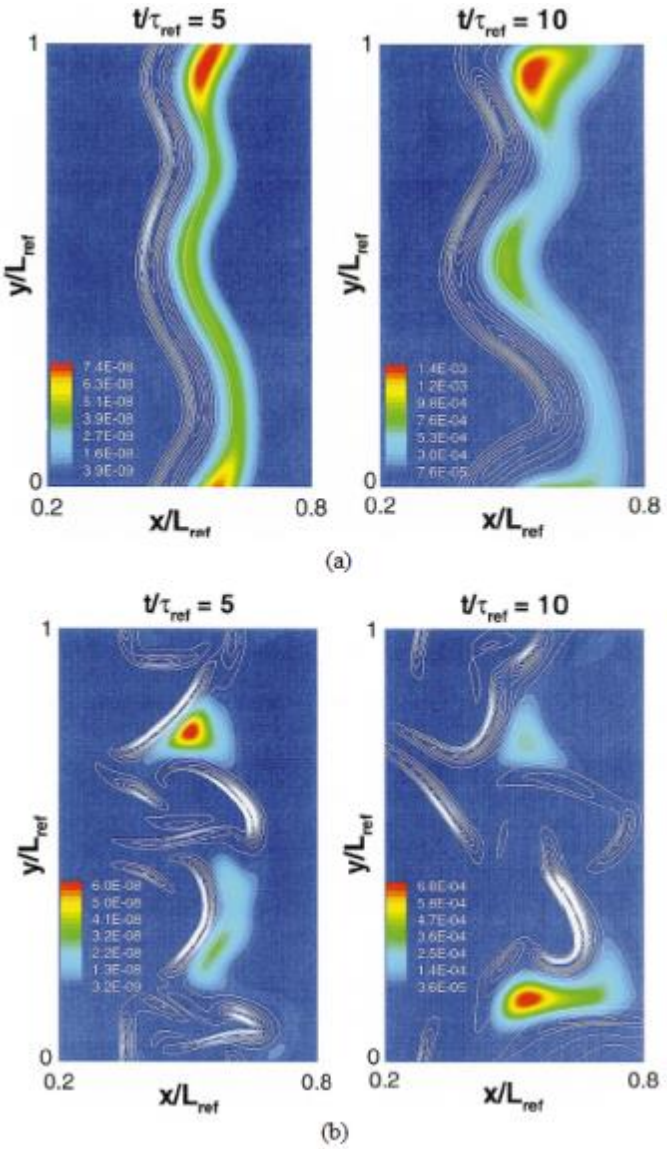


**Fig 1.3: $H_2$-$O_2$ auto-ignition kernel under (a) low turbulence and (b) high turbulence. White contours are for the H radical mole fraction and color contours are for H radical mass fraction. The two times series in (a) and (b) represent different instances during the ignition process. Figure adapted from [26].**

Experimental studies on auto-ignition in turbulent flows are conducted most commonly using the fuel jet in hot air or hot, vitiated coflow configuration. Auto-ignition in reacting JICF flow fields has not been studied extensively; however, chemical interaction between reactants and vitiated flows in jet-in-coflow experiments mimics the chemical processes of JICF auto-ignition, without the added flowfield

complexities. Cabra et al. [28], [29] are credited with conducting the first significant studies on fuel/premixed jets in vitiated co-flow. The sensitivity of the jet liftoff height to parameters such as jet velocity, co-flow velocity, and co-flow temperature suggested that flame stabilization occurred as a result of both auto-ignition and edge flame propagation.

Gordon et al. [22] expanded on the work of Cabra et al. presented in [28], [29] using a similar experimental configuration combined with simultaneous OH PLIF, $CH_2O$ PLIF, and Rayleigh imaging. The simultaneous imaging of OH, $CH_2O$, and temperature allowed for visualization of the formation of auto-ignition kernels. In the acquired images three primary behaviors were observed: (1) build-up of $CH_2O$ radical pool, (2) initiation of reaction where $CH_2O$ peaks, and (3) formation of steady flame where OH peaks. An example of the results obtained in [20] is shown in Fig. 1.4. The images in Fig. 1.4 capture examples of all the observed behaviors in the experiment. The first set of images in the top row shows examples of "$CH_2O$ only" behavior, where there is build-up of pre-ignition species and temperature has only slightly increased. At this instance the ignition has not completed. The next four images show examples of auto-ignition kernels, where localized region of strong $CH_2O$, OH and temperature are seen away from the lifted flame base. Three different ignition kernel sizes were observed: small kernel, medium kernel, and large kernel. These images are examples of a completed ignition sequence. The final two images show the stable flame behavior, away from the lifted flame base, and indicate that diffusion-flame behavior was primarily observed along the stabilized region of the flame. In [30] the authors studied the flame stabilization behavior of a diluted ($H_2$, $N_2$, or Air) ethylene jet in a highly preheated and diluted $O_2$ co-flow. Similar to the results in [22], upstream of the lifted flame base strong $CH_2O$ signal was observed, which indicated the occurrence of pre-ignition reactions.

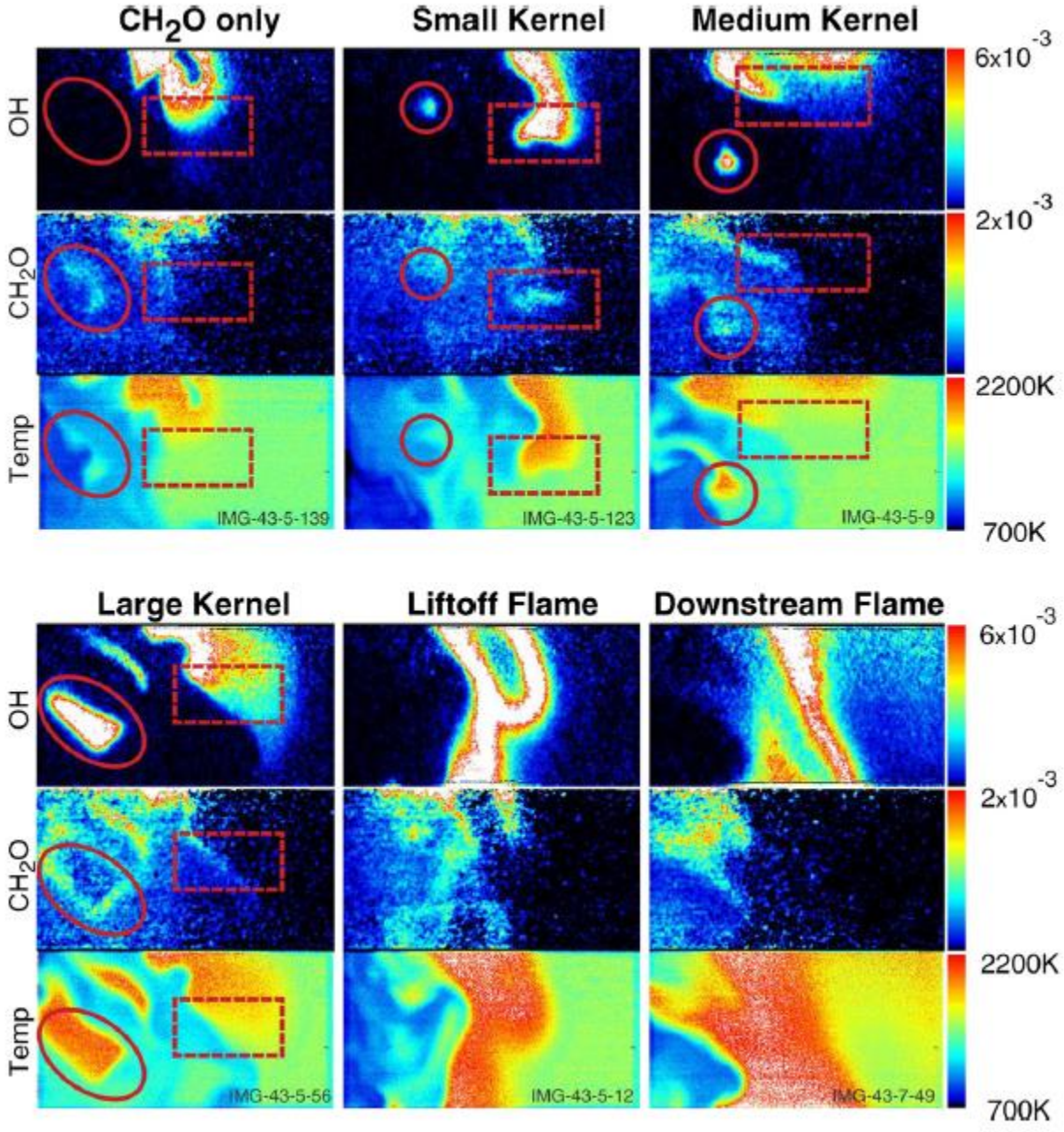


**Fig 1.4: OH PLIF, $CH_2O$ PLIF, and Rayleigh images acquired for a methane jet in vitiated coflow. This figure has been adapted from [22].**

Studies on fully premixed jet in vitiated coflow are not as common as non-premixed jet-in-coflow studies. Dunn et al. [31] used OH PLIF and Rayleigh scattering techniques to examine the flame behavior of a premixed methane-air jet ($\phi$=0.5, 0.6, 0.8) in vitiated coflow. The premixed flame

stabilized, lifted above the burner exit. The lifted flame structures resembled those of typical premixed flames and no investigation of the behavior upstream of the flame base was conducted. The work presented in this dissertation and in [31] adds an interesting feature to traditional non-premixed lifted flames studies, in that the reactant stream contains a combustible mixture. Non-premixed jets require mixing with coflow regardless of temperature; however for premixed jets mixing between reactant stream and coflow (or crossflow) is not necessarily required. As will be shown in this dissertation, the behavior of lifted premixed flames in vitiated crossflow is both similar to, and different than the behavior of lifted non-premixed flames.

## 1.4 Reacting JICF

### *1.4.1 Introduction*

The most extensive experimental reacting JICF research conducted thus far has focused on non-premixed systems, in which the jet is either pure fuel or pure oxidizer [32]–[49]. Currently, use of non-premixed JICF configurations in practical combustors is more widespread than premixed configurations, and as a result the research has trended towards further understanding of these non-premixed systems. The RQL combustor is one of the most notable combustors that utilize a non-premixed JICF system [2]. In the RQL combustor, stable combustion and low emissions of $NO_x$ are achieved through the use of staged combustor technology, as depicted in Fig. 1.5. In the Quick-Mix stage of the RQL combustor, jets embedded in the combustor walls are used to inject air into the fuel-rich combustion products exiting the Rich-Burn zone, wherein the injected air jets behave as jets in crossflow. The use of air jets in the Quick-Mix zone allows the combustor to rapidly transition from fuel-rich conditions to fuel-lean conditions, thereby bypassing stoichiometric combustion conditions that are associated with high temperatures and $NO_x$ production rates. The Quick-Mix zone is then closely followed by the Lean-Burn

zone where combustion reactions are driven to completion as a result of the mixing between the injected air and Rich-Burn combustion products.

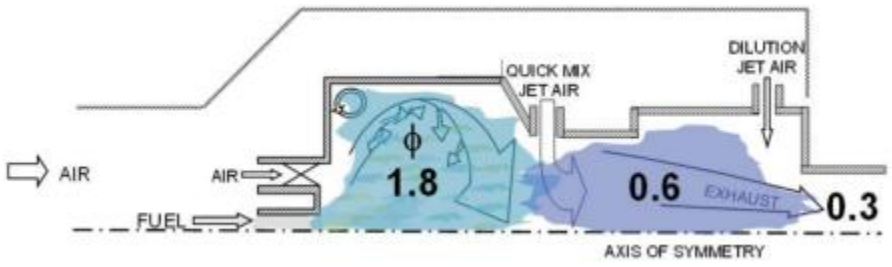


**Fig. 1.5: Schematic of RQL combustor, where ϕ represents the equivalence ratio in each combustor stage, adapted from [2].**

Increasing awareness of climate change behavior has led to stricter regulations on acceptable pollutant emission levels from combustion technology. To achieve this task, focus in combustion engineering has shifted toward developing combustion technology that utilizes premixed combustion. Premixed operating conditions allow for better control of combustor temperature, and ultimately $NO_x$ emissions, however premixed combustion schemes can result in stability issues within the combustor. The limited research currently available on premixed JICF and the need for further characterization of premixed combustor stability are the two motivating factors for the work presented in this dissertation. In the next two sections a literature survey of both non-premixed and premixed JICF research is presented. The literature survey will help to outline all the current knowledge on JICF flame behavior as well as highlight the areas where further information/studies are needed.

### *1.4.2 Non-premixed JICF*

In general, non-premixed JICF flames can be characterized by two distinct behaviors: attached and lifted flames. For non-premixed combustion systems, mixing between fuel and oxidizer is required for combustion to occur; therefore, the mixing behavior between jet and crossflow directly relates to the

flame stabilization. The non-premixed JICF research presented in this section will examine how different experimental parameters (i.e. *J*, jet injection angle, jet composition, crossflow conditions) affect flame stabilization.

Hasselbrink and Mungal [48] used simultaneous PIV and OH PLIF imaging to study the flame behavior at various locations in a JICF experiment. In the experiment, a non-premixed methane jet was injected into an air only crossflow at ambient temperature conditions. The JICF flame was completely lifted from the exit of the jet tube. OH PLIF measurements indicated that both the leeward and windward flame bases were highly wrinkled, and even broken at some locations. The width of the flame base on the leeward edge was significantly larger than the windward flame base suggesting a larger region of flammable mixture existed ahead of the flame at the leeward location. The thickness and wrinkled nature of the OH layer led the authors to conclude that partial premixing between jet fuel and crossflow air was occurring ahead of the flame base. Thus, at the stabilization location partially-premixed flame propagation was the most dominant stabilization mechanism. Flame surfaces at mid-flame locations (away from the leading stabilization points) were found to be considerably smoother, which was attributed to a reduction in effective Reynolds number caused by the heat release. Additionally, this observation suggested that at mid-flame locations the flame acted as a diffusion flame, as opposed to the partially-premixed behavior at the flame base.

Han and Mungal [47] performed a similar experiment with angled jets injected as -45°, 0°, and 45° from the wall normal. CH PLIF and PIV measurement techniques were used. Positive two dimensional dilatation along the flame surface indicated regions where the flame behaved as a premixed flame. As the injection angle increased in the downstream direction (45°) the length of the flame edge with positive dilatation increased, indicating that increasing the injection angle allowed for more fuel-air premixing prior to reaction.

Steinberg et al. [46] also used simultaneous PIV and OH PLIF measurements to study a JICF system consisting of a preheated $H_2/N_2$ fuel jet injected into a heated air crossflow. Raman scattering was used to extract temperature and mixture fraction information in the experiment. The *J* values in the experiment were varied from 2 to 8.4. In each case tested, two distinct flame branches were observed in the OH PLIF measurements. The first branch, referred to as the lee stabilized branch was the steadier of the two branches. In this region slightly downstream of the leeward jet exit, flow recirculation caused by flow wrapping around the jet column created a low speed region in which the flame could consistently stabilize. The second flame branch, referred to as the lifted flame branch, was located along the upper side of the jet trajectory (windward jet boundary). The lifted flame branch exhibited highly unsteady features, including times when it was barely lifted from the windward jet exit and times when it was pushed back to the flame tip, as seen in Fig. 1.6. Raman scattering measurements revealed that there was a large variation in the mixture fraction present at the various lifted flame stabilization locations, indicating that the flame exhibited stratified premixed flame behavior including triple flames. Additionally, it was found that the position of the flame was highly dependent on the position and shape of the principal aerodynamic strain-rate field, as depicted in Fig 1.6.

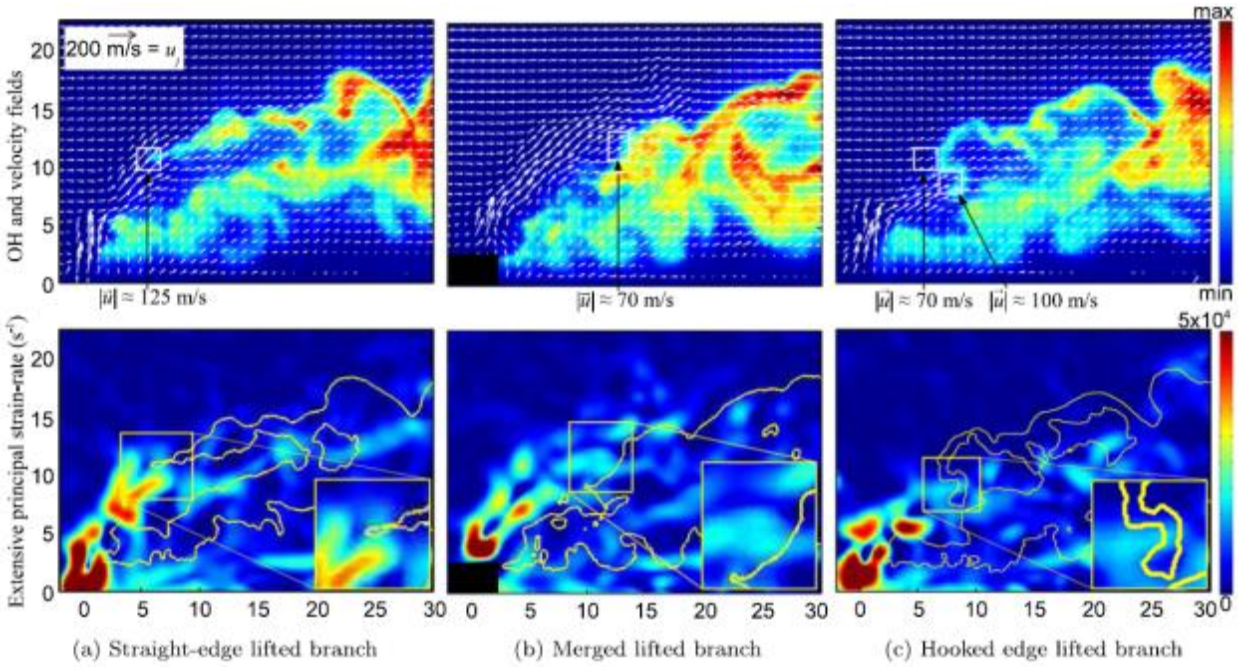


**Fig. 1.6: Figure adapted from Steinberg et al. [46] showing three commonly observed flame behaviors for $N_2/H_2$ jet injected into heated air crossflow. OH flame contour marked by yellow contour in extensive principal strain-rate images.**

Sullivan et al. [45] studied the flame stabilization behavior of a reacting fuel jet injected into a 1775K vitiated fuel-lean crossflow. The *J* values tested ranged from 1 to 240. For most configurations tested, the flame stabilized downstream of the jet exit; however for the jet with $CO/H_2$ fuel blend, the flame remained attached at the jet injector. Flame liftoff heights were found to vary between 0 and 10 jet nozzle diameters. Experimental ignition flow times, calculated using the known jet velocity and flame liftoff height, compared well with numerically computed ignition delay times suggesting that auto-ignition was the dominant flame stabilization mechanism.

Fleck et al. [35] studied the auto-ignition behavior of an $H_2/N_2$ jet injected into a vitiated air crossflow. Crossflow temperature was found to have the most significant impact on whether ignition occurred in the particular JICF configuration. At low crossflow velocities, pressure had no impact on JICF ignition whereas at high velocities and high pressure no ignition was observed. The experimental

ignition delay times were significantly shorter than those calculated using kinetic simulations. Mixing between jet and high temperature crossflow, enhanced by turbulence in the JICF flow field, was thought to assist in auto-ignition, such that the ignition delay time was reduced compared to the homogenous system in the kinetic simulations. Micka and Driscoll [39] found that in the case of a 50% $C_2H_4$/50% $H_2$ fuel jet injected into a high speed, high temperature crossflow, strong $CH_2O$ signal upstream of the stabilized flame front indicated the presence of an auto-ignition region. The lifted JICF flame base exhibited premixed flame behavior assisted by the upstream auto-ignition region.

Reacting non-premixed JICF has also been studied using various numerical techniques. In [50] DNS was used to analyze the flame stabilization behavior of an $H_2$ jet injected into a heated air crossflow. It was found that the leeward flame branch stabilized within 1.5-2 jet diameters downstream of the jet exit, and that the flame stabilization region was at a location where the average flow velocity was low and the average mixture fraction was stoichiometric. Kolla et al. [51] used DNS to analyze non-reacting JICF flow fields to identify regions that could support flame stabilization. Local flow velocity and mixture composition (temperature and equivalence ratio) were used to identify regions suitable for flame anchoring. As the jet was angled from 90° to 70° (facing the downstream direction), the size and number of regions suitable for flame stabilization decreased. This suggested that as the jet angle increases further in the downstream direction, flame stabilization became increasingly more difficult, which was supported by the experimental findings of Han and Mungal [47]. Kolla et al [51]verified the results from the non-reacting JICF DNS by performing a reacting JICF DNS at the same conditions. As predicted, the transition of jet injection angle from 90° to 70° resulted in flame blowout. As the injection angle decreased, the leading flame edge moved farther downstream until the flame base faced normal to the crossflow velocity which ultimately resulted in flame blowout.

### *1.4.3 Premixed JICF*

Currently, there have been very few published studies on premixed JICF behavior [8], [52], [53]. Schmitt et al. [52] conducted JICF experiments on a premixed propane-air jet injected into a fuel-lean 1775K vitiated crossflow. OH chemiluminescence imaging showed that the flame ignited immediately upon interaction with the crossflow, for *J* ranging from 4-10 and jet equivalence ratios ranging from 0.05-0.77. For the jet equivalence ratio at 0.77, the flame extended into the jet tube as a result of the horseshoe vortex drawing hot crossflow fluid into the jet nozzle. At low jet equivalence ratios the flame length was longest and the flame boundaries were not well defined, as shown in Fig. 1.7. At higher jet equivalence ratios fast reaction rates led to reduced flame length and a sharper flame boundary. Compared to the high crossflow temperature in [52] the crossflow temperature in the experiment presented in this dissertation was 1500K. At this crossflow temperature, a wider range of flame stabilization behaviors was observed including both attached and lifted flames.

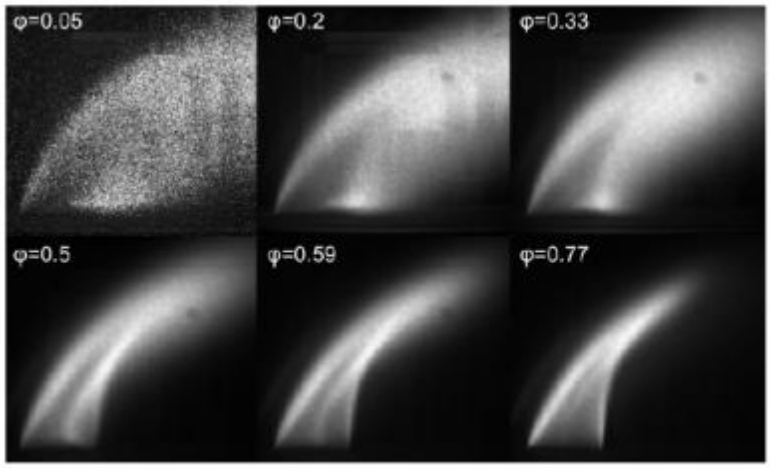


**Fig. 1.7: OH* Chemiluminescence images of *J* = 6 propane-air JICF flame. Adapted from Schmitt et al. [52].**

The experiment presented in [53] continued the work of Schmitt et al. [52] by examining a broader range of JICF parameters: including jet and crossflow, temperature, velocity and equivalence ratio. The primary goal in [53] was to characterize the flame stabilization location (i.e. liftoff height) based upon laminar flame speed or ignition delay scaling. Mixing between jet and crossflow upstream of the lifted JICF flame meant that the liftoff behavior could not be characterized singularly by flame speed or auto-ignition delay. Ultimately, it was determined that both premixed flame propagation and auto-ignition contribute to flame stabilization and flame liftoff scaling was achieved by considering both mechanisms and devising an empirical relationship.

### *1.4.4 Reacting JICF Literature Summary*

For the several non-premixed reacting JICF studies presenting, lifted flame behavior was most commonly observed. Stabilization of the lifted flame front was supported by partial premixing between the jet and crossflow, such that the leading flame edge displayed premixed flame propagation behavior. In the case of crossflow temperatures on the order of 1775 K, auto-ignition behavior was the dominant flame stabilization mechanism for both non-premixed and premixed configurations. The premixed JICF experiment presented in this thesis will examine how the stabilization behavior changes when the crossflow temperature is hot enough to support auto-ignition, however sufficiently less than 1775 K such that flame propagation behavior must also be considered. Additionally, the premixed JICF results will be compared to the non-premixed configurations in that the importance of jet-and-crossflow mixing ahead of the flame stabilization locations will be examined. Understanding the role of the crossflow in the flame stabilization in the premixed JICF system is important when considering how to develop the next generation combustion technology.

### 1.5 OH and $CH_2O$ PLIF Imaging

In this section, the theory behind OH PLIF and $CH_2O$ PLIF will be detailed as well how these techniques can be utilized for analysis of turbulent reacting flows. The value of Laser Induced Fluorescence (LIF) imaging for combustion analysis is well known, as it is a non-intrusive way to image/measure species within a reacting flow. The use of simultaneous OH PLIF and $CH_2O$ PLIF for imaging the heat release zone was first realized by Najm et al. [54] and Paul and Najm [55]. Najm et al. [54] first showed that HCO was a good marker, spatially and temporally, for heat release. The production of HCO occurs at a finite-rate, while the consumption of HCO occurs much more rapidly. Because of this, the concentration of HCO is directly proportion to its production rate. Heat production via combustion occurs primarily through the formation of $CO_2$ and $H_2O$, not HCO; however, most of the carbon in hydrocarbon combustion follows a reaction pathway that leads to $CO_2$ formation via HCO. Because the concentration of HCO is directly proportional to its production rate, it can be measured using LIF and is directly proportional to the rate of heat production.

Useable HCO LIF signal is difficult to obtain, as HCO concentration is low and has a short fluorescence lifetime and low fluorescence quantum yield [55]. Paul and Najm [55] suggesting using simultaneous OH PLIF and $CH_2O$ PLIF measurements for heat release imaging in place of HCO PLIF. The OH and $CH_2O$ react to form HCO through the reaction $CH_2O + OH \Rightarrow H_2O + HCO$. The reaction proceeds at a forward reaction rate $k(T)[CH_2O][OH]$, where $k$ is the temperature dependent rate constant and $[CH_2O][OH]$ is the product of the number density of the two species. From LIF measurements the following relation has been developed, $S_{CH_2O}S_{OH} \propto f(T)[CH_2O][OH]$, where $S_{CH_2O}S_{OH}$ is the spatial product of $CH_2O$ and OH LIF measurements and $f(T)$ is the combined temperature dependence of the $CH_2O$ and OH LIF signals. Over a specific range of temperatures, it is possible to obtain $f(T)$ that mimics $k(T)$ such that the spatial product of OH and $CH_2O$ LIF is

equivalent to the forward reaction rate $k(T)[CH_2O][OH]$. The strong fluorescence quantum yield of OH and $CH_2O$ eliminate the issues associated with HCO PLIF, and make simultaneous OH PLIF and $CH_2O$ PLIF a suitable alternative for heat release imaging.

An additional benefit of conducting $CH_2O$ PLIF measurements is visualization of the flame preheat region. Characterization of preheat zone structure becomes increasingly important in turbulent reacting flows and flows where auto-ignition occurs. Li et al. [56] investigated turbulence-combustion interaction in a piloted premixed flame configuration using simultaneous PLIF imaging of CH, OH, and $CH_2O$. The $CH_2O$ was consistently observed in the inner region of the flame, toward the unburned reactant stream, whereas OH was observed in more broad regions, forming along the outer flame edge. This indicated that $CH_2O$ was a good marker for the preheat zone. The thin spatial overlap of the OH and CH2O PLIF signals were then used to identify the regions of heat release. Turbulence interaction with the flame was shown to affect the preheat zone structure, in that increasing turbulence caused broadening of the $CH_2O$ signal in the direction of the preheat zone. The increased mixing between combustion products and cold reactants caused by high turbulence has been shown to also create distributed regions of high temperatures in the reactant stream , which resemble thickened preheat zones [57].

Pre-ignition behavior can also lead to increased $CH_2O$ presence upstream of flame. Medwell et al. [58] studied the influence of $CH_2O$ on ignition delay time, for analysis of lifted jet flame stabilization. The results showed that addition of small quantities of $CH_2O$ in the reactant stream led to faster ignition delay times. In [22] pre-ignition $CH_2O$ formation was observed experimentally for a lifted jet in vitiated coflow. Isolated islands of $CH_2O$ indicated pre-ignition behavior which then led to the formation of auto-ignition kernels, marked by the simultaneous presence of OH. For the premixed

jet in vitiated crossflow, simultaneous $CH_2O$ PLIF and OH PLIF will be employed, for studying turbulence effects on flame structure as well as identification of possible auto-ignition behavior.

### 1.6 Summary

Previous research on reacting jet-in-crossflow has been conducted primarily for non-premixed configurations. The rapid and thorough mixing between jet and crossflow has been found to be a critical component in the reduction of harmful $NO_x$ pollutions produced in practical combustors. The jet and crossflow mixing is also directly related to flame stabilization behavior in these non-premixed configurations. Diffusion flame behavior, partially premixed flame behavior, and auto-ignition were the flame stabilization mechanisms observed in non-reacting JICF experiments. More stringent pollutant emission regulations have led to an increased interest in JICF for lean-premixed (LPM) combustion technology; however there is lack of premixed JICF research available. Thus, the goal of the research conducted for this dissertation was to address the following questions regarding the flame stability and flowfield characteristics for a premixed jet in vitiated crossflow:

1. What are the general flame behaviors for a premixed jet injected into a vitiated crossflow? What effect, if any, do $J$ and $\phi_j$ have on flame stabilization?

2. What are the dominant flame stabilization mechanisms?

3. How is the JICF flowfield affected by the presence of combustion? Can non-reacting JICF scaling arguments be applied to a reacting JICF under highly-confined flow conditions?

4. How can premixed JICF flame behavior be modeled? Can laminar flame simulations, (premixed flame, opposed flow configuration, or plug flow reactor) be used to analyze JICF flame stabilization?

# CHAPTER TWO

# 2. Experimental Test Rig & Diagnostic Techniques

## 2.1 Experimental JICF Test Rig

The facility used for conducting the vitiated JICF experiments was similar to that described in [59], [60]. A CAD rendering of the experimental test rig is shown in Fig. 2.1. The test rig used for the JICF experiments consisted of three main sections: a swirl burner, transition section, and jet mixing section.

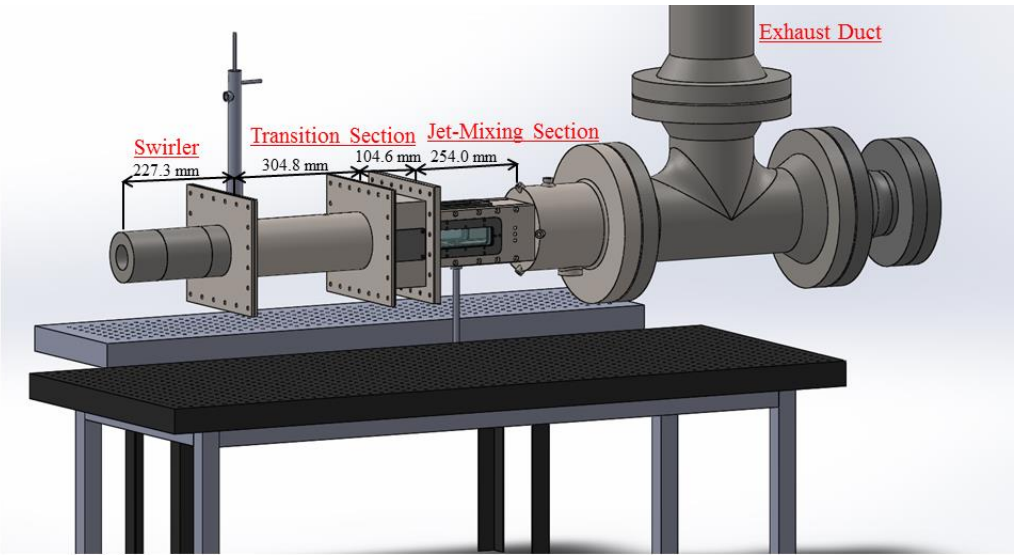


**Fig. 2.1: CAD rendering of vitiated JICF experimental test rig.**

The swirl burner was used to generate the hot, vitiated crossflow conditions. Vitiated crossflow was used, versus preheated air, for example, to create crossflow conditions similar to that which may exist in the secondary stage of a staged combustor system. A CAD rendering of the swirl burner exit is shown in Fig. 2.2. Compressed, dry air (at ambient temperature conditions) was supplied to the swirler through a choked orifice flow (O'keefe Controls Co.). Propane (Airgas, Industrial Grade) was injected

into the swirling air at the throat near the swirler exit, via a 3.19mm I.D. stainless steel tube. The propane flow was metered using a Parker mass flow controller (Porter Model 251 0-50 SLPM). The swirl stabilized flame was ignited using a torch flame, (same igniter described in [60]).

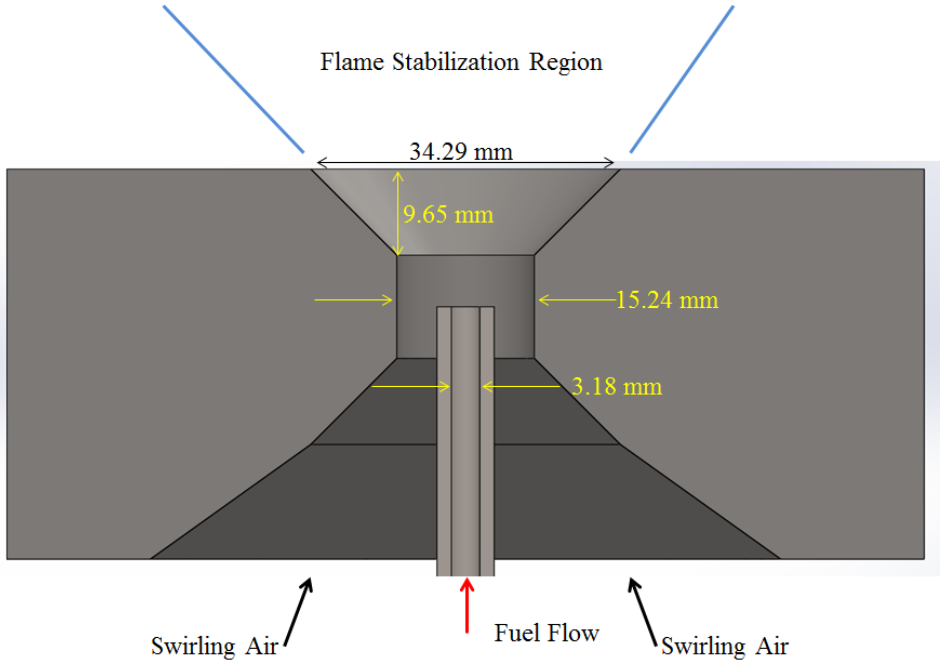


**Fig. 2.2: CAD rendering of swirl burner exit design.**

In the transition section, the 38.1 mm circular cross-section at the exit of the swirl burner was gradually transitioned to a 38.1 mm x 76.2 mm rectangular cross-section. The stainless steel transition section was lined with Kast-o-lite 97L refractory to reduce heat losses. To construct the transition section the Kast-o-lite was mixed with water then poured and packed around a smooth Styrofoam insert molded specifically for the desired cross-sectional profile. Once the Kast-o-lite dried, the Styrofoam insert was removed and the resulting Kast-o-lite surface, making up the transition section inner wall, was smooth. The outer stainless steel surfaces of the transition section were wrapped with ceramic fiber blankets (Thermal Ceramics, Cerablanket), held in place by woven ceramic tape (Cotronics, Thermez 397T), to further reduce heat loss. A 12.7 mm thick ceramic honeycomb (Induceramic - 56 cells per 100mm) was placed at the end of the transition section to straighten the flow entering the jet mixing

section. The swirl flame extended approximately 150 mm into the transition section, keeping the flame approximately 260 mm from the upstream face of the honeycomb.

The stainless steel jet-mixing-section (also referred to as the test section) is depicted in Fig 2.3(a). Three of the test section walls contained fused-silica quartz windows to allow for optical access. The jet tube was press fit into a stainless steel blank of same dimensions as the fused-silica windows, as shown in Fig 2.3(b). The jet exit was centered along the stainless steel blank and held in place with a set screw. This design was chosen so that jet tubes with various diameters could easily be inserted into the blank. For the JICF configuration studied here the jet diameter was maintained constant at $d_j$=9.525 mm. The fused-silica window and stainless steel blanks were held in place using a series of gaskets, as described in detail in [60]. The jet tube assembly was made of stainless steel and the tube length exceeded 200 mm (>20$d_j$). The jet contained fully premixed ethylene (Airgas, Ultra High Purity) and air. The ethylene-air premixing length exceeded 1 m (>100$d_j$) to ensure complete premixing. The flow rate of the jet fuel and air were metered separately using choked orifices (O'keefe Controls Co.).

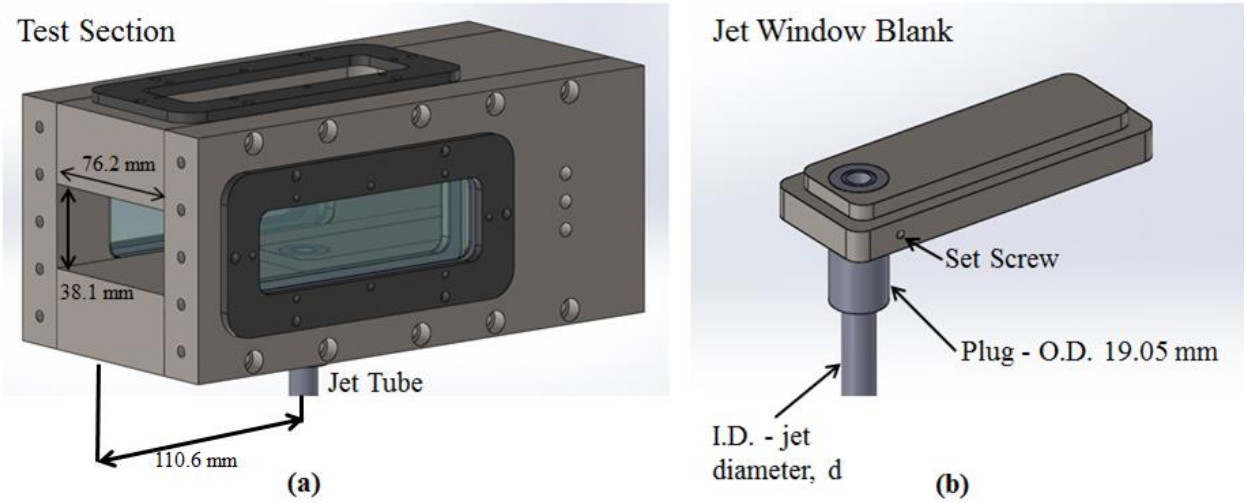


**Fig. 2.3: (a) Test section and (b) stainless steel window blank with jet tube.**

Combustion products from the JICF experiment were exhausted to the atmosphere by way of an exhaust stack that was open to the outdoor environment. The base of the exhaust stack is depicted in Fig. 2.1. Downstream of the jet-mixing section was a dump chamber, Fig 2.4, where water cooling could be employed if necessary. For the JICF experiment flow rates were low, relative to [60], and thus the water cooling was not required.

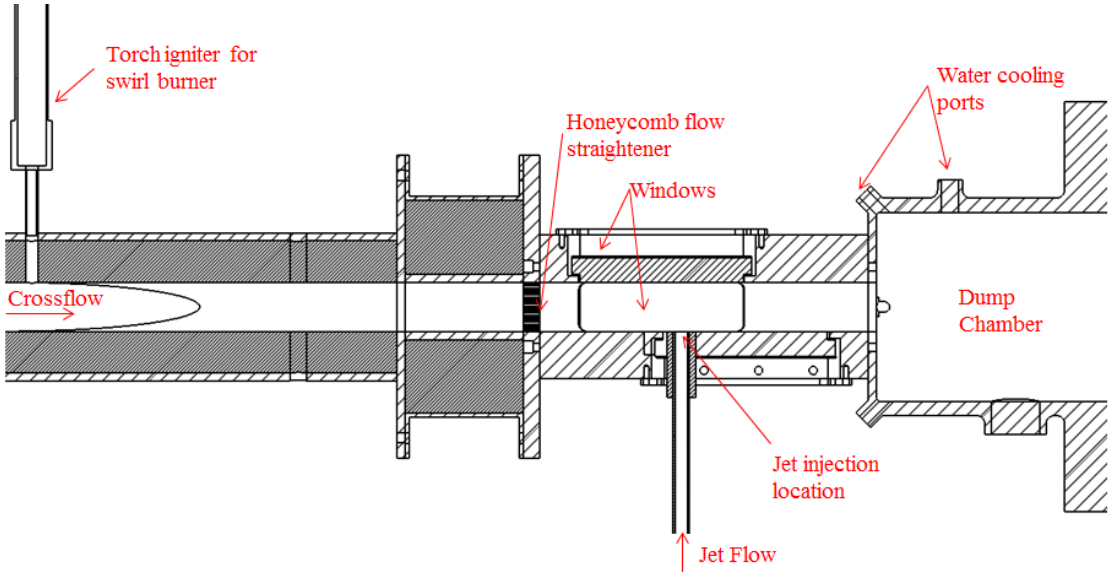


**Fig. 2.4: Sectional view of test rig configuration, including the dump chamber downstream of the jet mixing section.**

## 2.2 Characterization of Crossflow

Proper characterization of crossflow conditions is essential for any JICF experiment. This includes characterization of the crossflow velocity profile, composition, and temperature. Throughout experimentation the crossflow conditions were maintained constant. The velocity profile for the crossflow was measured experimentally using PIV. The setup for PIV measurements will be described in further detail in *Section 2.2*. The velocity measurements were made along the test section centerline which aligns with the jet center. Figure 2.5 shows the velocity profile, at the windward jet edge, along the test section lateral direction. The crossflow is characterized by mean velocity $U_\infty$ = 7.6 m/s with approximately ±3% variation along the lateral direction. The two visible peaks in the velocity profile are a result of the flow behavior generated by the swirler. To remove these peaks and make the profile more uniform a longer transition section would be required. In order to minimize heat losses from the vitiated flow, the transition section was not extended, and the ±3% variation along the lateral velocity profile was deemed acceptable.

Equation (1) was used for calculation of $J$. The jet velocity, $V_j$ was computed using the known mass flow rates of ethylene and air in the jet, and verified by PIV measurements. Jet density was computed using the known mixture composition and temperature. The crossflow velocity was $U_\infty$ and the crossflow density was computed using the experimentally measured crossflow temperature and numerically calculated equilibrium composition.

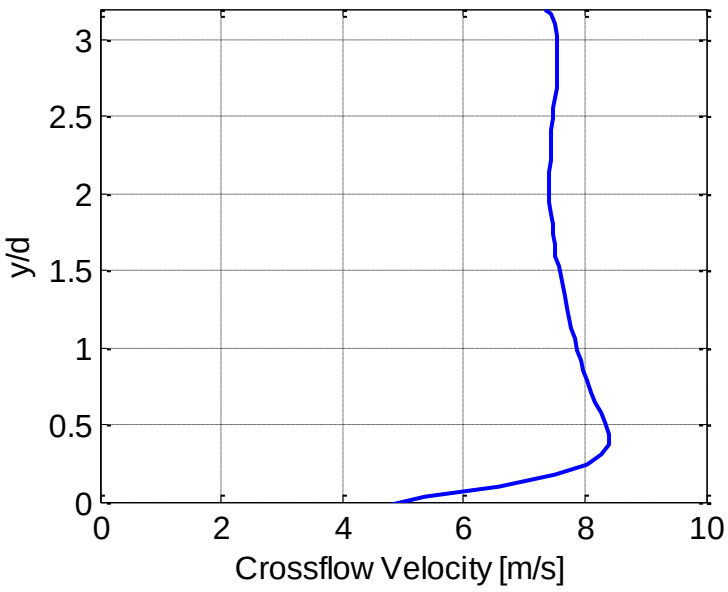


**Fig. 2.5: Crossflow velocity profile at the windward jet edge.**

The equivalence ratio of the propane-air mixture in the swirl burner was approximately $\phi_\infty = 0.87$. The goal was to maintain fuel-lean crossflow conditions while ensuring the crossflow temperature at the jet exit location was 1500K. The crossflow temperature was measured using an R-type thermocouple (TC), with an exposed bead. The thermocouple was inserted into a suction pyrometer to reduce radiation heat loss to and from the TC bead, as described in further detail in [46]. Temperature measurements along the lateral span of the test section were taken at the jet exit location. The equivalence ratio of the propane-air mixture in the swirler was effectively increased until the mean temperature along the lateral direction at the windward jet edge was 1500K.

During the crossflow temperature tests, the equivalence ratio was increased only when temperature appeared unchanged after approximately 5 minutes time. For $\phi_\infty = 0.87$ steady-state temperature was reached after 20 minutes of running the vitiated flow and the average crossflow temperature at the upstream jet edge was found to be 1500 K with ±1% non-uniformity along the lateral span of the test section. Streamwise temperature measurements were not conducted due to there being

no probe access away from the jet centerline. The crossflow temperature profile measured laterally at the windward jet exit is shown in Fig. 2.6b. While the profile is flat for $d_j$ >1, below this limit the temperature quickly drops. This behavior was attributed to an issue with the suction pyrometer, rather than non-uniformity in the crossflow temperature. As the suction pyrometer moved closer to the test section floor, the strength of suction was reduced which ultimately affected the temperature reading. Thus, only data taken for $d_j$ > 1 were included in analysis of crossflow temperature. Based on the temperature measurements it was also determined that the vitiated flow in the test rig needed to be run for 20 minutes to reach steady-state conditions; therefore, before conducting any JICF experiments the vitiated flow was run for the full 20 minutes.

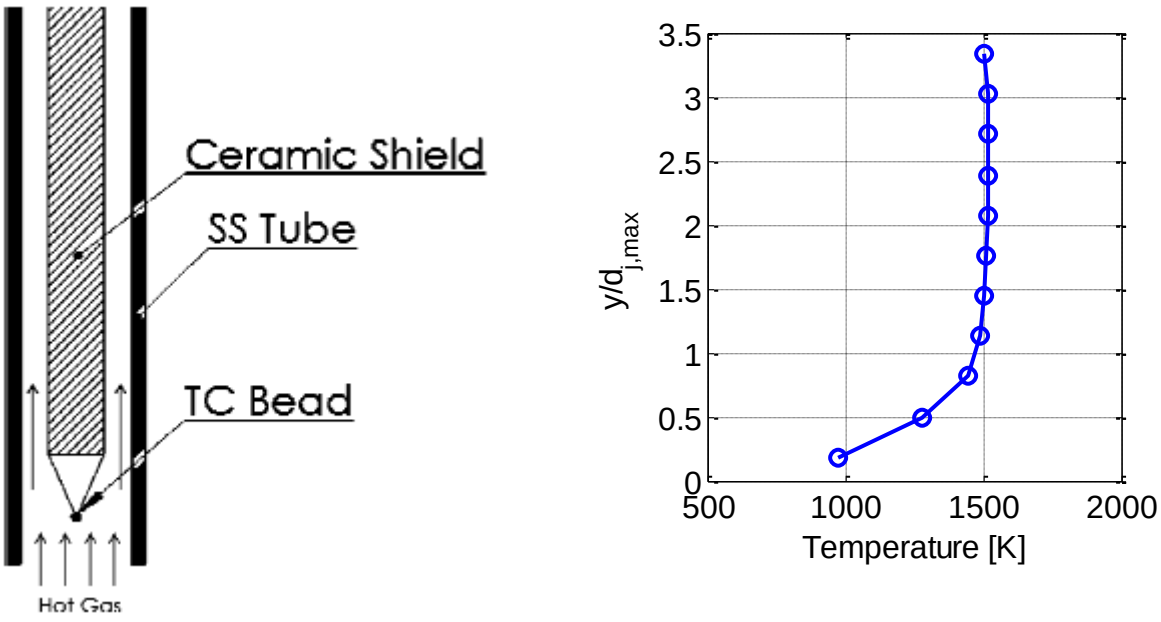


(a) (b)

**Fig 2.6: (a) Drawing of suction pyrometer used to measure crossflow, adapted from [46]. (b) Crossflow temperature profile along lateral direction at windward jet edge for $\phi_\infty$ = 0.87.**

The composition of the crossflow was determined using CHEMKIN Equilibrium solver with the USC-II mechanism. The equilibrium solver was run for the $\phi_\infty$ = 0.87 propane-air mixture and the resulting products from the solver are presented in Table 2.1. For the numerical simulations presented in Chapter V, the equilibrium mole fractions of the species shown in Table 2.1 were used to estimate the crossflow composition. The equilibrium temperature for the $\phi_\infty$ = 0.87 propane-air mixture was 2140 K; therefore, when using the equilibrium results to simulate crossflow conditions in the auto-ignition calculations (presented in Chapter 5), the temperature was adjusted to match the experimental value of 1500 K.

**Table 2.1: Crossflow composition computed from equilibrium calculations.**

| Species | Inlet Mole Fraction | Equilibrium Mole Fraction |
|---|---|---|
| $N_2$ | 0.762 | 0.735 |
| OH | 0.000 | 0.003 |
| $H_2$ | 0.000 | 0.001 |
| $H_2O$ | 0.000 | 0.133 |
| $O_2$ | 0.203 | 0.027 |
| CO | 0.000 | 0.002 |
| $CO_2$ | 0.000 | 0.099 |
| $C_3H_8$ | 0.035 | 0.000 |

## 2.3 Jet Composition

The jet composition was varied from lean to rich jet conditions. The three jet equivalence ratios examined were $\phi_j$ = 0.8, 1.0, 1.2. The motivation for varying the jet equivalence ratio from lean to rich conditions was two-fold. As previously mentioned, the premixed JICF configuration is a novel concept; and so for fundamental analysis of the premixed JICF flame stabilization, characterization of the effect of $\phi_j$ is a useful first step. Secondly, the degree of premixing between fuel and air in a practical jet injector is unknown. In this JICF experiment, the jet fuel and air were perfectly premixed; however, in a practical injector this may not be the case. Varying jet equivalence ratio in the experiments helped to

isolate the effect of different equivalence ratios, which is useful in the case that equivalence ratio gradients exist in an actual jet injector.

A JICF global equivalence ratio was determined using the formulation,

$$(aC_3H_8 + bC_2H_4) + c(O_2 + 3.76N_2) \rightarrow (3a + 2b)CO_2 + (4a + 2b)CO_2 + 3.76cN_2 \quad (8)$$

where *a*, *b*, *c* are the number of moles of propane, ethylene, and air, respectively. The value of *a* was determined using the total mass flow rate of crossflow fluid and the crossflow equivalence ratio. The value *b* was dictated by *J* and $\phi_j$. Two different *c* values were required for determination of $\phi_{JICF}$: $c_{stoich}$ and $c_{exp}$. At each *J* and $\phi_j$ condition, the value $c_{stoich}$ was computed assuming complete consumption of air in the reaction, in order to determine the stoichiometric fuel-air ratio. The value $c_{exp}$ was computed based on the total air supplied in the crossflow and jet for the given *J* and $\phi_j$. Ultimately, $\phi_{JICF}$ was a measure of the overall system equivalence ratio based upon the total fuel and air supplied. Table 2.2 shows the global equivalence ratio $\phi_{JICF}$ for the experimental values of $\phi_j$ and *J*. The system remained lean for all $\phi_j$ and *J*, operating as low as 0.85 and as high as 0.93. As previously mentioned, the work in this dissertation is motivated by the need for LPM combustion; the test matrix of $\phi_j$ and *J* allowed for an extensive study on flame stabilization behavior while still maintaining globally fuel lean conditions.

**Table 2.2: Global equivalence ratio $\phi_{JICF}$ for varying experimental conditions.**

| $\phi_j$ | ***J* Value** | | | |
|---|---|---|---|---|
| | **5.2** | **8.7** | **15.7** | **22.7** |
| **0.8** | 0.86 | 0.86 | 0.86 | 0.85 |
| **1** | 0.88 | 0.89 | 0.89 | 0.89 |
| **1.2** | 0.90 | 0.91 | 0.92 | 0.93 |

Laminar flame properties for $\phi_j$ were calculated using the CHEMKIN Premix code [13]. The USC-II mechanism was used for the calculations and the premixed mixture was varied based on the experimentally employed values of $\phi_j$. The calculations considered no mixing between jet and crossflow, such that the inlet mixture temperature was 300 K; results are presented in Table 2.3. Dilatation was calculated by differentiating the one-dimensional premixed flame velocity profile with respect to axial distance such that $\nabla \cdot u = \frac{du}{dx}$.

**Table 2.3: Laminar flame properties for experimental jet mixtures.**

| **Jet Equivalence Ratio** $\phi_i$ | **Adiabatic Flame Temperature [K]** $T_{ad}$ | **Laminar Flame Speed [cm-s$^{-1}$]** $S_L^0$ | **Laminar Flame Thickness [mm]** $\delta_T^0$ | **Maximum Heat Release [kJ-cm$^{-3}$-s$^{-1}$]** $q_{max}$ | **Maximum Dilatation [s$^{-1}$]** $(\nabla \cdot \vec{u})_{max}$ |
|---|---|---|---|---|---|
| **0.8** | 2170.67 | 50.03 | 0.33 | 5.97 | 9939.42 |
| **1** | 2367.69 | 64.13 | 0.29 | 8.93 | 16405.41 |
| **1.2** | 2364.91 | 65.46 | 0.28 | 8.92 | 17441.35 |

## 2.4 Diagnostic Techniques

### *2.4.1 High Speed Chemiluminescence Imaging*

High speed chemiluminescence images were acquired using a Photron Fastcam SA5 high speed camera. The camera was focused using a 35 mm, f/1.4 Nikkor lens in combination with a +4 macro lens attachment. The macro lens allowed no UV light to pass through, therefore no OH* signal was detected by the camera. Tests were performed with a CH bandpass filter centered at 430nm +/-10nm. There were no significant differences observed in the chemiluminescence signal when the filter was used; this suggested that most of the chemiluminescence acquired without the filter was CH*. Because

the bandpass filter allowed for only 40% transmissivity, the acquisition of the final chemiluminescence data was done so without the use of any filter. The chemiluminescence images were line-of-sight integrated and the camera was situated perpendicular to the crossflow, with the jet injection from the bottom of the test section, as depicted in Fig. 2.7. Frame rate varied from 8.4 - 12 kHz; for all $\phi_j$ and $J$, measurements were conducted at 8.4 kHz and for the richer, more luminescent flame, measurements were also taken at 12 kHz. Approximately 0.5 seconds worth of images were acquired (~6000 frames at 12kHz and ~4200 frames at 8.4kHz) at each test condition and saved at the 16-bit maximum resolution of the camera.

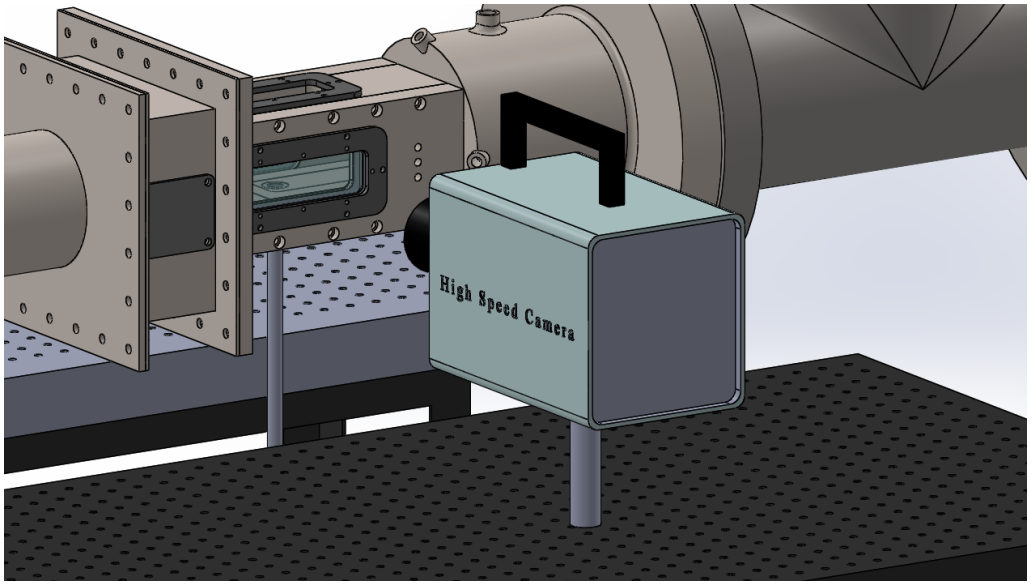


**Fig. 2.7: Camera location for high speed chemiluminescence imaging experiments.**

### *2.4.2 Particle Image Velocimetry*

For high speed PIV measurements conducted on the JICF configuration, the laser source was a dual-cavity Nd:YLF (Neodymium-doped yttrium lithium fluoride) diode laser from Litron Lasers

(model LDY304-PIV 10 mJ per pulse, 1 kHz repetition). Nd:YAG mirrors (Thorlabs NB1-K08) were used for aligning the optical path of the PIV laser beam. A planar laser sheet was formed with a spherical lens assembly and Galilean Telescope, and aligned with the jet center as shown in Fig. 2.8. The laser sheet covered the entire height of the test section, spanning from x/d~-1.4 to x/d~3, and was approximately 1 mm thick. The camera used to capture the Mie scattering was a Vision Research Phantom v710 high speed CMOS camera. An f/4, Nikkor 105 mm lens in combination with a +4 macro lens was attached to the camera to focus on the laser sheet. The acquisition rate was 3500 frames per second (double frame, double exposure), with the full camera chip (1280 x 800 pixels) being utilized. A target plate with 1 mm diameter dots spaced 4 mm apart was placed along the jet centerline in alignment with the laser sheet, for proper calibration of the Mie scattering images. Dynamic Studio v.3.41 software was used to control the data acquisition, including the timing of the PIV system.

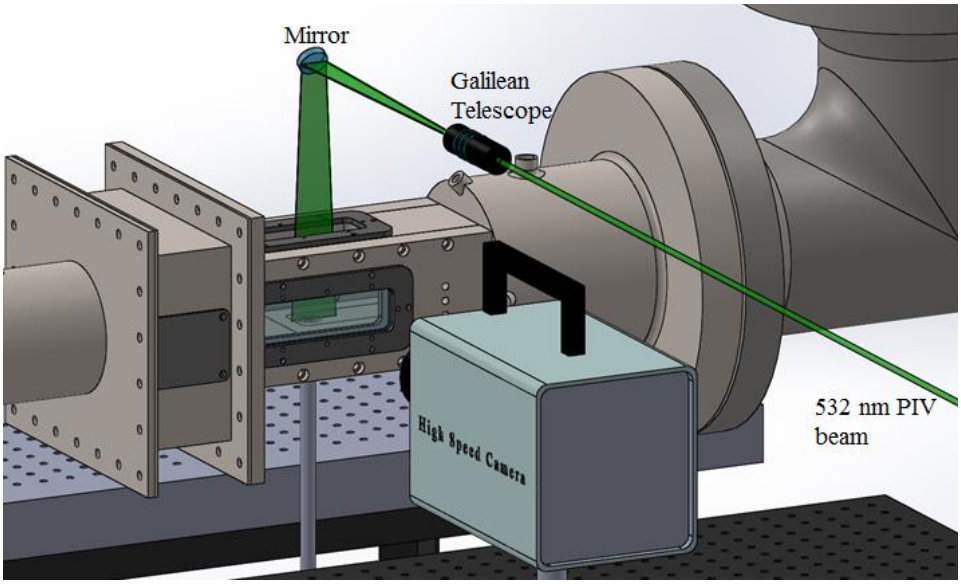


**Fig. 2.8: Experimental setup for high speed PIV measurements.**

The Mie scattering images were processed using LaVision DaVis 7.2 software. A multi-pass cross-correlation algorithm was used starting with a 128x128 interrogation window size and reducing to a final interrogation window size of 32x32 with 50% overlap. The final vector field resolution was 0.65

mm. The time between laser pulses was chosen as 30 μs, which ensured the particles in the flow traveled roughly one quarter width of the interrogation window (32x32 pixels).

For the simultaneous PLIF and PIV measurements, a New Wave (Solo PIV III) dual-cavity Nd:YAG laser (50 mJ/pulse at 10 Hz) was used to provide 532 nm laser pulses for Mie scattering. The Mie scattering images were collected using a Flow Master 3S 1024x1280 CCD Camera. The camera was equipped with an f/4 Micro-Nikkor 200-mm focal length lens and a 532 ±1 nm bandpass filter (Andover 532FS02-50). An f=-20mm cylindrical lens mounted to the Nd:YAG laser head generated the PIV laser sheet. The laser sheet spanned the entirety of the test section height and was approximately 1 mm thick. The time between laser pulses was chosen as 23 μs, which ensured the particles in the flow traveled roughly one quarter width of the final interrogation window size. The Mie scattering images were processed using LaVision DaVis 7.2 software. A multi-pass cross-correlation algorithm was used with a single interrogation window size of 32x32 with 50% overlap. The resulting vector field resolution was 0.27 mm.

For both PIV measurements Alumina particles (K.C. Abrasive Co.) ~1 μm in diameter were used to seed the jet and crossflow simultaneously during PIV experiments. To control the seed density, bypass valves were used upstream of the swirl burner and jet air supply lines. Air flow through the two seeders could be controlled independently so that the seed density of the flow could be increased or decreased as needed. The jet air stream was seeded with particles upstream of where the jet air and ethylene were mixed, so that the fuel-air mixing length was kept constant between PIV and non-PIV experiments.

Vector post-processing was performed using Matlab software. Central differencing discretization was used for calculating vector field derivatives. For high speed PIV measurements 7000 Mie scattering images were collected at each test condition. Convergence studies were performed on the

high speed PIV data to reduce vector processing time. Pdfs for two-component velocity, vorticity, strain, and dilatation were computed for each instantaneous PIV image for non-reacting and reacting PIV. The instantaneous pdfs were then averaged over 100, 500, 1000, and 2000 image increments. The pdfs converged within 1% by 1000 images; therefore 2000 of the 7000 images were processed for vector field statistics shown in this thesis. For simultaneous PLIF-PIV measurements, the acquisition rate was ~1Hz therefore only 500 Mie scattering images were collected. All 500 images were included for data analysis.

The planar PIV measurements allowed for calculation of derivatives in two dimensions (*x* in the cross flow direction and *y* in the normal direction). For the JICF flame analysis the flow field quantities of particular interest were 2-D dilatation $\nabla \cdot \vec{u}$, vorticity $\omega_z$, and *x*-direction normal strain $S_{xx}$, *y*-direction normal strain $S_{yy}$, and shear strain-rate $S_{xy}$, which were computed using equations (9a)-(9e) respectively.

$$\nabla \cdot \vec{u} = \frac{du}{dx} + \frac{dv}{dy} \tag{9a}$$

$$\omega_z = \frac{dv}{dx} - \frac{du}{dy} \tag{9b}$$

$$S_{xx} = \frac{du}{dx} \tag{9c}$$

$$S_{yy} = \frac{dv}{dy} \tag{9d}$$

$$S_{xy} = \frac{1}{2}\left(\frac{du}{dy} + \frac{dv}{dx}\right) \tag{9e}$$

### *2.4.3 $CH_2O$ PLIF*

For $CH_2O$ PLIF measurements, the frequency-tripled 355 nm output beam (250 mJ/pulse at 10 Hz) from a Spectra Physics Pro-230 Nd:YAG was used to excite transitions in the $4_0^1$ band of $CH_2O$. A Princeton PI-Max II intensified camera with 1024x250 pixels was used to acquire the $CH_2O$ PLIF

signal. The camera was gated to 150 ns and equipped with an f/2.8 Micro-Nikkor 55-mm focal length lens and a filter (Omega Optical Inc. 450DF70D) allowing over 60% transmission at wavelengths between 425-485 nm.

### *2.4.4 OH PLIF*

For OH PLIF measurements a Continuum Surelite I Nd:YAG laser at 532nm (200 mJ/pulse at 10 Hz) was used to pump a Sirah Precision Scan Dye laser with Rhodamine 590 dye, which provided a 566 nm beam. This beam was frequency doubled to obtain a beam with 2 mJ/pulse at 282.67 nm. This allowed for excitation of the OH $Q_1(5)$ transition in the $A^2\Sigma^+ \leftarrow X^2\Pi$ (1,0) band. This transition was selected based on its line strength and relatively low Boltzmann fraction sensitivity between temperatures of 1000-2500 K. A Princeton PI-Max I intensified camera, 1024x1024 pixels, equipped with an f/4.5 UV-Nikkor 105 mm lens and a 320+/-20 nm bandpass filter (Semrock Bright Line filter FF01-320/40-25) was used to collect the OH fluorescence. The intensifier was gated for 300 ns to minimize any interference with flame chemiluminescence.

### *2.4.5 Simultaneous $CH_2O$ PLIF, OH PLIF and PIV*

The experimental setup for the simultaneous $CH_2O$ PLIF, OH PLIF and PIV measurements was complex and involved alignment of the three lasers and three camera systems temporally and spatially. The Q-switch output signal from the Spectra-Physics Nd:YAG laser ($CH_2O$ PLIF) was the master signal for control of the PLIF-PIV timing. The signal went to a delay generator (Stanford DG535) that sent triggers to the Continuum Nd:YAG laser (OH PLIF) and to the PI-Max I camera (OH PLIF). The PI-Max I was the limiting factor for the PLIF-PIV data acquisition rate, at approximately 1 Hz. An output TTL signal taken from the PI-Max I camera was sent to a second delay generator (Stanford DG535) and was used to trigger the PI-Max II camera and the PIV system. The trigger signal sent to the PIV system, triggered a Programmable Timing Unit (PTU) that separately controlled the timing of the PIV laser and

camera system. An oscilloscope was used to view signals from the three lasers and three cameras simultaneously to ensure that the timing was appropriately synchronized. The timing diagram from the PLIF-PIV system is shown in Fig. 2.9. The timing separation between the OH and $CH_2O$ laser pulses was approximately 400 ns, and was chosen to prevent any interference in the signal collection of OH and $CH_2O$ between the two cameras. Because the two PIV laser pulses straddled the two PLIF laser pulses, the PIV trigger signal was delayed such that it was one image behind the OH and $CH_2O$ cameras. Therefore the first PLIF images acquired in each run by the two PI-Max cameras were ignored, as was the last Mie scattering image acquired in each run by the PIV camera.

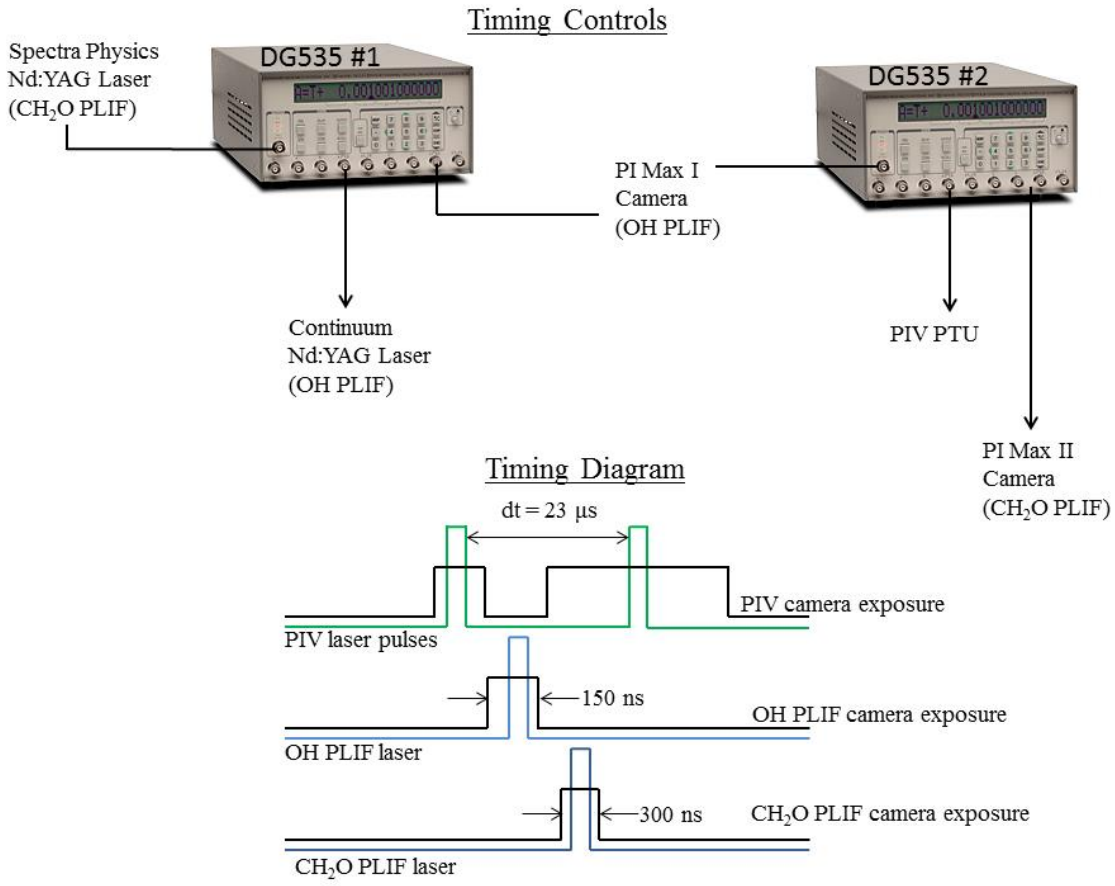


**Fig 2.9: Simultaneous $CH_2O$ PLIF, OH PLIF, and PIV timing controls and timing diagram.**

The laser beam paths for $CH_2O$ and OH PLIF were combined using a dichroic mirror as shown in Fig. 2.10a. The high pulse energy needed for $CH_2O$ fluorescence at 355 nm caused laser scatter within the test section that was potentially dangerous to the cameras. As a result, the beam widths for the $CH_2O$ and OH PLIF were kept less than 9 mm. At this width, the beams were able to pass through the jet exit without scattering off the test section floor. The beams were focused in the imaging plane using an f=500 mm converging lens. Approximate thicknesses for the 355-nm and 282.67-nm beam in the test section were 250 μm and 350 μm, respectively. Final pixel resolutions for $CH_2O$ and OH PLIF imaging were 76 x 76 x 250 μm and 26 x 26 x 350 μm, respectively. Since the PLIF beam widths were narrower than the jet exit, two different regions of interest (ROI) were required to image both the windward and leeward JICF flame behavior. Figure 2.10b shows the approximate laser sheet location for the windward and leeward ROI, overlaid on a chemiluminescence image. As shown, the beams had to be brought in at an angle to capture the entire flame behavior in the two ROI, while avoiding scatter.

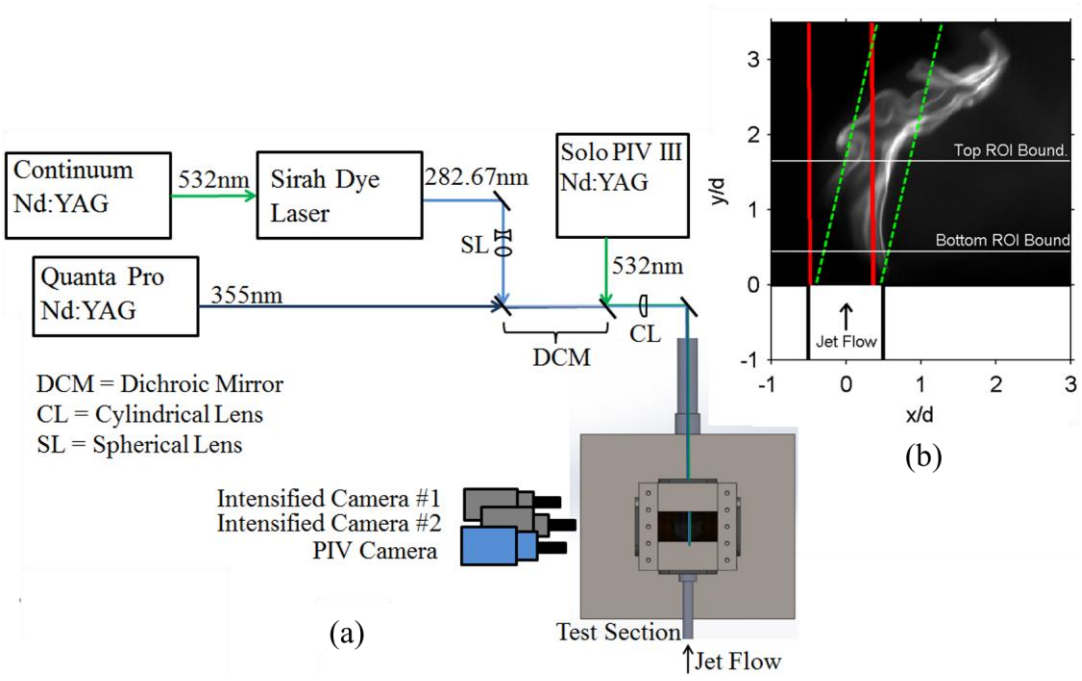


**Fig. 2.10: a.) Schematic of PLIF-PIV setup. The crossflow flow direction through the test section is pointed outward from the page. b.) Windward ROI laser sheet bounds (-) and leeward ROI laser sheet bounds (--) overlaid on chemiluminescence image of $J$ = 5.2 reacting JICF. Crossflow direction is from left to right.**

The PIV laser was combined with the two beams used for PLIF using a second dichroic mirror as shown in Fig. 2.10a. The beam was focused using the same f=500 mm converging lens as that used for the PLIF beams. All three laser sheets were aligned with one another along the jet centerline. The same target as that used for high speed PIV calibration was used for verifying alignment of the 355-nm, 282.67-nm and 532-nm laser sheets, the two PI Max cameras, and Flow Master PIV camera.

## 2.5 Image Analysis Techniques

### *2.5.1 High Speed Chemiluminescence*

Instantaneous flame boundaries were extracted from the chemiluminescence images for analysis of the flame stabilization behavior. Fig 2.11 shows an example of instantaneous high speed chemiluminescence images for a reacting JICF ($J$=5.2, $\phi_j$ = 1.2) with the flame edges marked by white

contours and the windward and leeward stabilization points marked by filled white circles. In the chemiluminescence images, the black regions, or very dark regions, indicated no flame, or very weak chemiluminescence, whereas the brighter white regions indicated strong chemiluminescence.

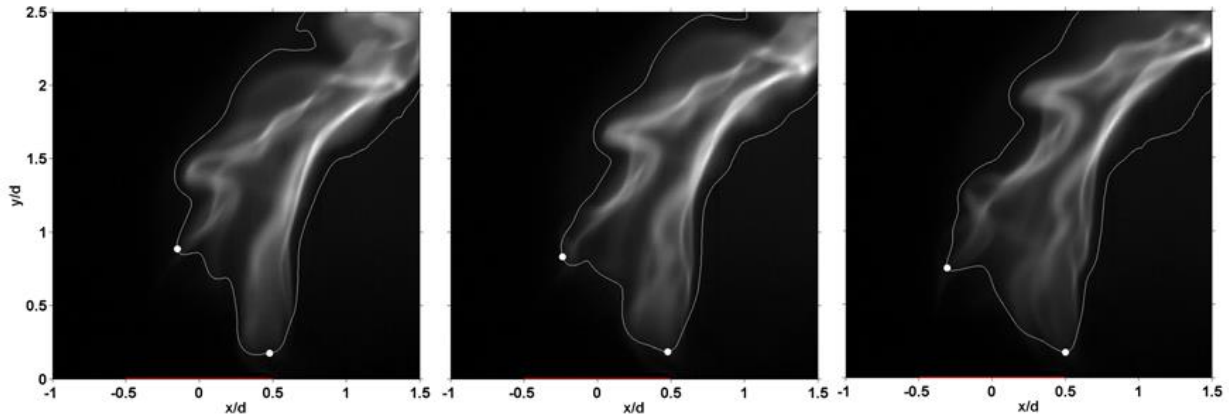


**Fig. 2.11: High speed chemiluminescence images of reacting JICF flame ($J$ = 5.2, $\phi_j$ = 1.2) with flame edge contours overlaid in white and windward and leeward flame stabilization points marked by white dots.**

The chemiluminescence images were first filtered with a Gaussian convolution filter to ensure that the flame contour was smooth. The Gaussian filter had a kernel size of 10x10 pixels (0.7x0.7 mm) and dimensionless standard deviation equal to 5. The flame boundary was then taken as the contour level at 10% of the maximum intensity in the instantaneous filtered image. The windward and leeward stabilization points were selected by locating the points on the contour closest to the windward and leeward jet edges, respectively. If the windward leading edge point was found to be located at the same axial location as the leeward leading edge, the image was flagged, and manually examined to determine if windward blowoff occurred. In the case of windward blowoff, no windward leading edge point was collected from the image. Spatial correlation of the chemiluminescence images was achieved by imaging a target plate (the same as described previously) with the high speed camera.

### *2.5.2 Dilatation from PIV*

The flame boundary was also identified using the two-dimensional dilatation field computed from PIV data. For premixed reacting flows, [54], [61], [62] have shown that there is generally good alignment between positive dilatation and heat release. For an ideal gas under constant-pressure conditions, the effect of heat release $q$ on dilatation $\nabla \cdot \vec{u}$ is shown by eq. (10a-c).

$$\nabla \cdot \vec{u} = -\frac{1}{\rho}\frac{D\rho}{Dt} \qquad (10a)$$

$$\nabla \cdot \vec{u} = \frac{1}{T}\frac{DT}{Dt} - \frac{1}{\overline{W}}\frac{D\overline{W}}{Dt} \qquad (10b)$$

$$\nabla \cdot \vec{u} = \frac{1}{T}\left[\frac{q}{\rho c_p} + \frac{\nabla \cdot (\lambda \nabla \mathrm{T})}{\rho c_p}\right] - \frac{1}{\overline{W}}\frac{D\overline{W}}{Dt} \qquad (10c)$$

The gas density is represented by $\rho$, gas heat capacity by $c_p$, mixture thermal conductivity by $\lambda$, and the mean mixture molecular weight by $\overline{W}$. The first term within the brackets on the right hand side of eq. (10c) is the contribution to dilatation from heat release; thus, heat release acts to increase dilatation. The second term in the brackets in eq. (10c) is the contribution to dilatation as a result of thermal diffusion governed by Fourier's Law. Najm et al. [54] have shown that for a premixed flame undergoing low to moderate strain, the contribution from thermal diffusion term is minimal. In the same study, the last term in eq. (10c), $\frac{1}{\overline{W}}\frac{D\overline{W}}{Dt}$, was also found to be negligible. From reacting PIV measurements, the two-dimensional $\nabla \cdot \vec{u}$ was computed through eq. (9a), using the local velocity field and neglecting the $\partial w/\partial z$, as it was not resolved by the planar PIV measurement. Analysis of the dilatation, presented later in this thesis, will include examination of effects from $\partial w/\partial z$.

In each instantaneous dilatation field, the contour(s) at 10% of the maximum (positive) dilatation were located. The longest contour in the flow field at the threshold value was taken as the flame boundary. In Fig. 2.12, the 10% of maximum dilatation contour from reacting JICF ($J$=8.7, $\phi_j$ = 1.2)

PIV measurements is marked by the solid black line. The windward stabilization point was found in each instantaneous PIV image by finding the point on the contour closest to the jet exit. No leeward flame stabilization point was identified since high (positive) dilatation was also present in non-reacting JICF at the same location; therefore the contour always suggested a fully attached leeward flame. In addition to the contribution from heat release, nonzero dilatation can also be a result of fluid motion into and out of the two-dimensional plane. Crossflow fluid exits the jet centerline plane ahead of the windward jet exit, as the jet acts as an obstruction to the crossflow, which results in negative two-dimensional dilatation. In the jet wake the flow re-enters the centerline plane as it wraps around the back of the jet, generating positive two-dimensional dilatation near the leeward jet exit. As expected, in the non-reacting flow no strong positive dilatation was found at the windward edge; thus, the high positive dilatation in reacting PIV measurements along the windward edge was attributed to the presence of heat release.

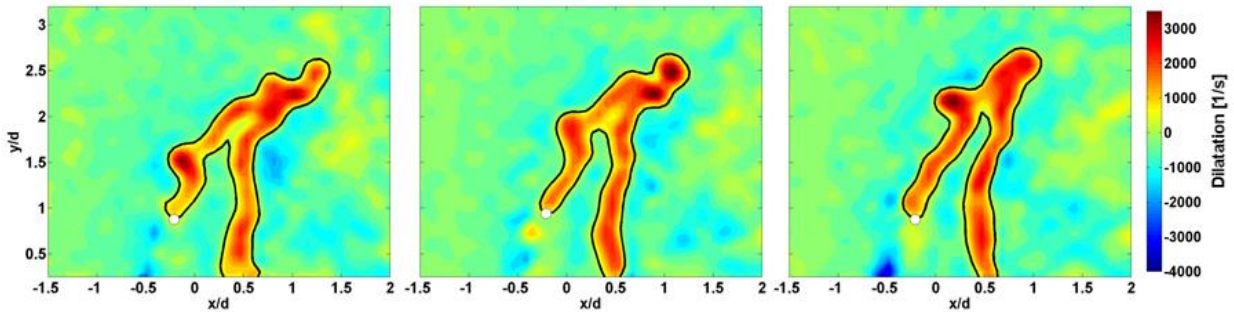


**Fig. 2.12: Dilatation computed from high speed PIV measurements of reacting JICF ($J$ = 8.7, $\phi_j$ = 1.2) with flame edge contours overlaid in black and windward flame stabilization point marked by white dot.**

### *2.5.3 PLIF Image Processing*

The goal of simultaneous $CH_2O$ PLIF and OH PLIF measurements was to visualize heat release in the reacting JICF flowfield through pixel-by-pixel multiplication of the PLIF images. For alignment

of the $CH_2O$ PLIF, OH PLIF, and PIV images, a target was placed in the imaging plane (same as previously mentioned) and images of the target were acquired by all three cameras. LaVision DaVis 7.2 software was used to perform the calibration for the cameras based on the target images and specific reference points. After calibration, OH image data was interpolated onto a grid matching equivalent resolution to that of the $CH_2O$ grid (lesser resolution). In Fig. 2.13, the various stages of image processing are shown. First, each grid-corrected/background subtracted PLIF image was filtered using a non-linear anisotropic diffusion filter [63], Fig. 2.13(b). A threshold equivalent to 10% of the maximum pixel intensity in the filtered image was used to remove low-level noise. Following the removal of this noise, a locally adaptive thresholding technique was applied to the image. The local threshold values were computed by determining the mean pixel intensity in a specified square window of pixels (75 x 75 for $CH_2O$ and 150 x 150 for OH), and then subtracting a constant value from the mean (-0.08 for $CH_2O$ and -0.025 for OH). This adaptive threshold was used to determine the regions corresponding to fluorescence signal in the filtered image such that the remaining images were binarized where 0 represented background and 1 represented LIF signal. The binarized $CH_2O$ and OH PLIF images were then multiplied by the non-linear filtered images, Fig. 2.13(c). Finally the OH and $CH_2O$ images were overlaid to determine the region of spatial overlap, as shown in Fig. 2.13(d). This approach identifies regions of heat release only. To quantify heat release magnitude the $CH_2O$ and OH images shown in Fig. 2.13(c) were multiplied pixel-by pixel.

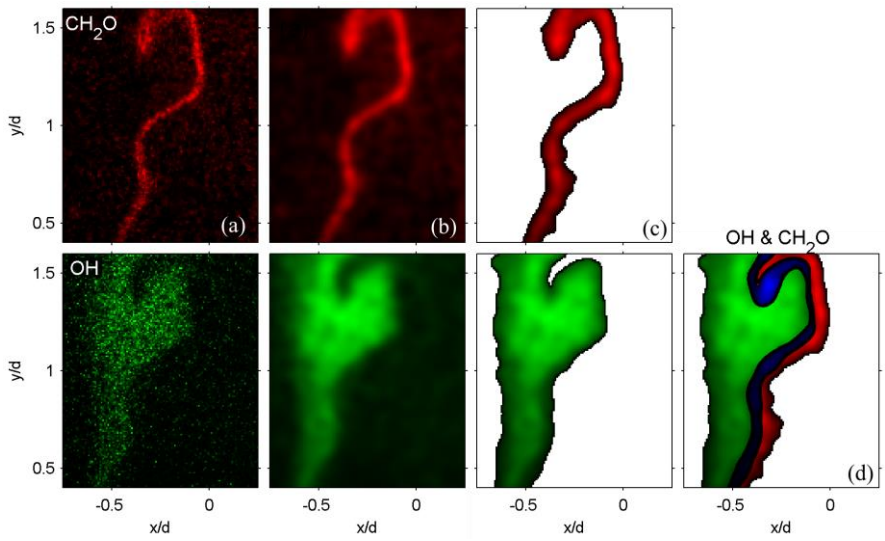


**Fig. 2.13: Example of PLIF image processing routine: (a) original image, (b) non-linear filtered image, (c) product of binarized and filtered images, and (d) OH & $CH_2O$ overlap with heat release contour shown in blue.**

For aerodynamic flame strain eq. (6) and curvature calculations, the inner heat release contour (closer to reactants) was used, similar to the approach taken by Kariuki et al. [64]. Because the heat release was defined by the spatial overlap of OH and $CH_2O$, the inner heat release contour aligns with the maximum gradient of OH nearest the reactants. The maximum OH gradient is often used for flame edge marking and was the technique adopted in [19], [20]; however, in those studies local extinction could not be accounted for as no $CH_2O$ measurements were taken. The use of simultaneous OH and $CH_2O$ improves flame edge identification, as the flame edge is conditioned upon there being spatial overlap between OH and $CH_2O$ and not just OH.

Once the flame edge was extracted from the PLIF measurements, the (*x*, *y*) flame edge coordinates were parameterized by a flame path-length parameter *S* such that *x(S)* and *y(S)*, as done in [19-20]. For each point along the flame edge, *n* neighboring points were fit by a 3rd order polynomial to smooth the flame edge and determine the local parametric functions for *x(S)* and *y(S)*. The largest value *n* was chosen at each point such that the length of the flame segment was just less than $5\delta_T^0$. The 3rd

order polynomials were differentiated and used to calculate the flame surface normal vector as well as the curvature. The normal was calculated such that a positive normal pointed towards the reactants. The curvature, *C*, was computed using,

$$C = \frac{\dot{x}\ddot{y} - \dot{y}\ddot{x}}{(\dot{x}^2 + \dot{y}^2)^{3/2}} \qquad (11)$$

where $\dot{x}$ and $\dot{y}$ are the first derivatives of the parametric functions such that $\dot{x} = \frac{dx}{dS}$; $\ddot{x}$ and $\ddot{y}$ are the second derivatives of the parametric functions.

Positive curvature represented a flame front that was convex to the reactants while negative curvature represented a flame front that was concave to the reactants. The curvature resolution was approximately 2.9 mm$^{-1}$ based on the thickness of the OH laser sheet. The aerodynamic flame strain $\kappa_a$ was computed using,

$$\begin{aligned} \kappa_a &= \left(\delta_{ij} - n_i n_j\right) S_{ij} \\ &= (1 - n_x^2) S_{xx} + \left(1 - n_y^2\right) S_{yy} \\ &\quad - 2 * n_x n_y S_{xy} \end{aligned} \qquad (12)$$

Flame edge points spaced less than 0.27 mm (PIV resolution) apart were removed to ensure that the flame edge resolution matched the PIV resolution. At each remaining flame edge point, the flow field statistics were integrated along the flame edge normal, in the direction going across the heat release contour. The integrated flow field statistics along these directions were used to determine $\omega_z$, $S_{ij}$, and $\nabla \cdot \vec{u}$ along the flame edge.

# CHAPTER THREE

# 3. Characterization of Flame Stabilization and Flow Field: $\phi_j$ = 1.2 JICF

**Introduction**

In this chapter results are presented for characterization of flame stabilization and flow field behavior for a $\phi_j$ = 1.2 JICF. The results shown are those obtained from high speed chemiluminescence imaging at 12 kHz and high speed PIV measurements. For this first study jet equivalence ratio was held constant while *J* was varied from 5 to 23. Availability of the high speed PIV system was limited, so the number of cases to be examined had to be reduced. Thus, it was decided to first examine the behavior of the non-reacting jet in vitiated crossflow and the $\phi_j$ = 1.2 reacting jet in crossflow. This rich equivalence ratio condition was chosen, over the lean and stoichiometric conditions, because of the dynamic flame behavior that was observed in preliminary JICF experimental tests. This dynamic behavior will be discussed in greater detail in the following sections; for clarity here, the $\phi_j$ = 1.2 was the condition at which flame behaviors ranging from full flame attachment at the jet exit to complete windward flame blowoff were observed. The lean flame never exhibited full flame attachment and so experiments with the $\phi_j$ = 1.2 JICF made for a better study of the various JICF flame stabilization behaviors.

## 3.1 Time-Averaged Observations

### *3.1.1 Flame Behavior*

The time-averaged flame behavior was analyzed first, using the results from high speed chemiluminescence imaging. The average flame location was determined by taking the average of the 0.5 seconds of data acquired at each run condition. Figure 3.1 shows the average flame location for the

$\phi_j$ =1.2 JICF for $5 < J < 23$. The flame remained nearly attached on the leeward side and lifted on the windward side of the jet. The windward liftoff height increased with increasing *J*, while the leeward liftoff height was nearly unaffected by *J*. Very weak signal (<10% max intensity) was present upstream of the windward liftoff height for $J$=5.2, extending all the way to the jet exit. This was the result of intermittent windward flame attachment that was observed. The location of the 90% maximum heat release contour suggested that the most intense burning occurred above the leeward jet exit. The location of this intensely burning region shifted further away from the jet exit with increasing *J*. The contours in each average image are spaced further apart from one another with increasing *J*, suggesting that the flame surface area increased with increasing *J*. For $J > 8.7$ the JICF flame length increased such that the flame impinged into the wall opposite the jet exit. The contours along the windward jet edge also straightened with increasing *J*, as the increase in jet momentum reduced the amount of jet bending.

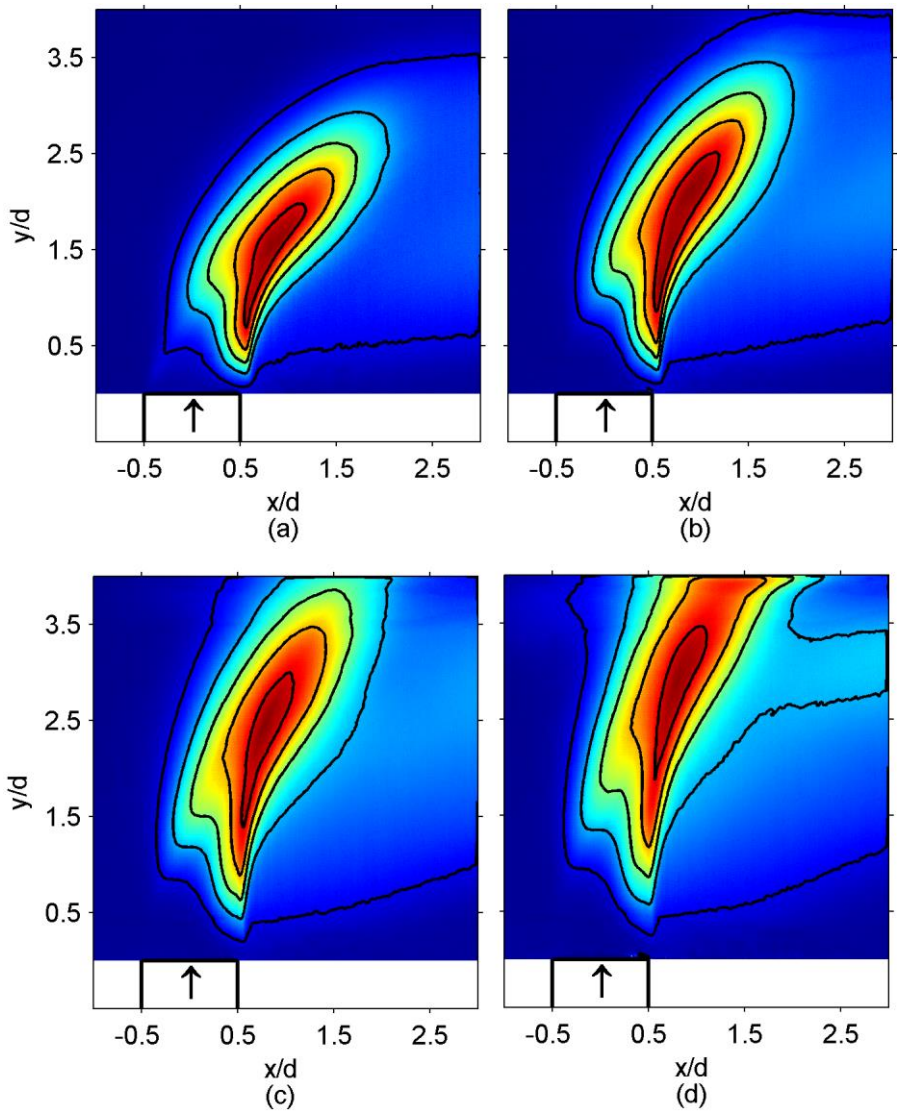


**Fig. 3.1: Average chemiluminescence image for $\phi_j$ =1.2 JICF for (a) $J$ = 5.2, (b) $J$ = 8.7, (c) $J$ = 15.7, and (d) $J$ = 22.7. Black contour lines represent 10, 30, 50, 70, 90% maximum intensity.**

### *3.1.2 JICF Flow Field*

Average flowfield calculations for the non-reacting and $\phi_j$=1.2 JICF are presented in this section, based on the high speed PIV measurements. Figure 3.2 displays the average $V_{mag}/V_j$ contours, where $V_{mag} = \sqrt{V_x^2 + V_y^2}$. In Fig. 3.2 streamlines (shown in white) are overlaid on the velocity field, with the jet center streamline shown in black. For both non-reacting and reacting JICF, the jet

penetration increased with increasing *J*, as shown by the jet centerline trajectory. For the non-reacting JICF, the effective jet width decreased along the jet trajectory as evidenced by converging windward and leeward streamlines. As the amount of crossflow fluid entrainment increases along the jet trajectory, the jet structure breaks down. This behavior is seen most clearly at $J = 5.2$, where the jet structure is visible in the jet nearfield, however further downstream is nearly no longer visible. For $J > 5.2$ the jet structure remains mostly intact along its trajectory until it impinged into the opposing wall.

In the case of the $\phi_j$=1.2 JICF, the jet structure never disappeared along the jet trajectory for all *J* conditions. As previously mentioned, the breakup of the jet structure is due mostly in part to the entrainment of crossflow. Several studies of both jet in co-flow and JICF have found that co-flow/crossflow entrainment rates decrease when heat release is present [48], [65], [66]. In these studies, the shear layer of the reacting jet also appeared more laminar than the shear layer of the non-reacting jet, due to a decrease in local Reynolds number. The reduction in crossflow entrainment reduces the jet decay and allows the reacting jet to maintain its structure longer compared to a non-reacting jet at equivalent *J*.

The change in jet structure between the non-reacting and $\phi_j$ =1.2 JICF was shown to have an effect on the flow behavior upstream of the jet. For the non-reacting flowfield images presented in Fig. 3.2 a clear stagnation region is seen upstream of the windward jet nearfield. The stagnation region forms as a result of the jet column acting as an obstruction to the crossflow; increasing *J* strengthened the effective obstruction and led to a larger stagnation region. As shown in Fig. 3.2, the presence of heat release further increased the size of the stagnation region. The reduction in crossflow entrainment under reacting conditions forces more crossflow to flow around the jet, generating a larger stagnation region along the windward boundary.

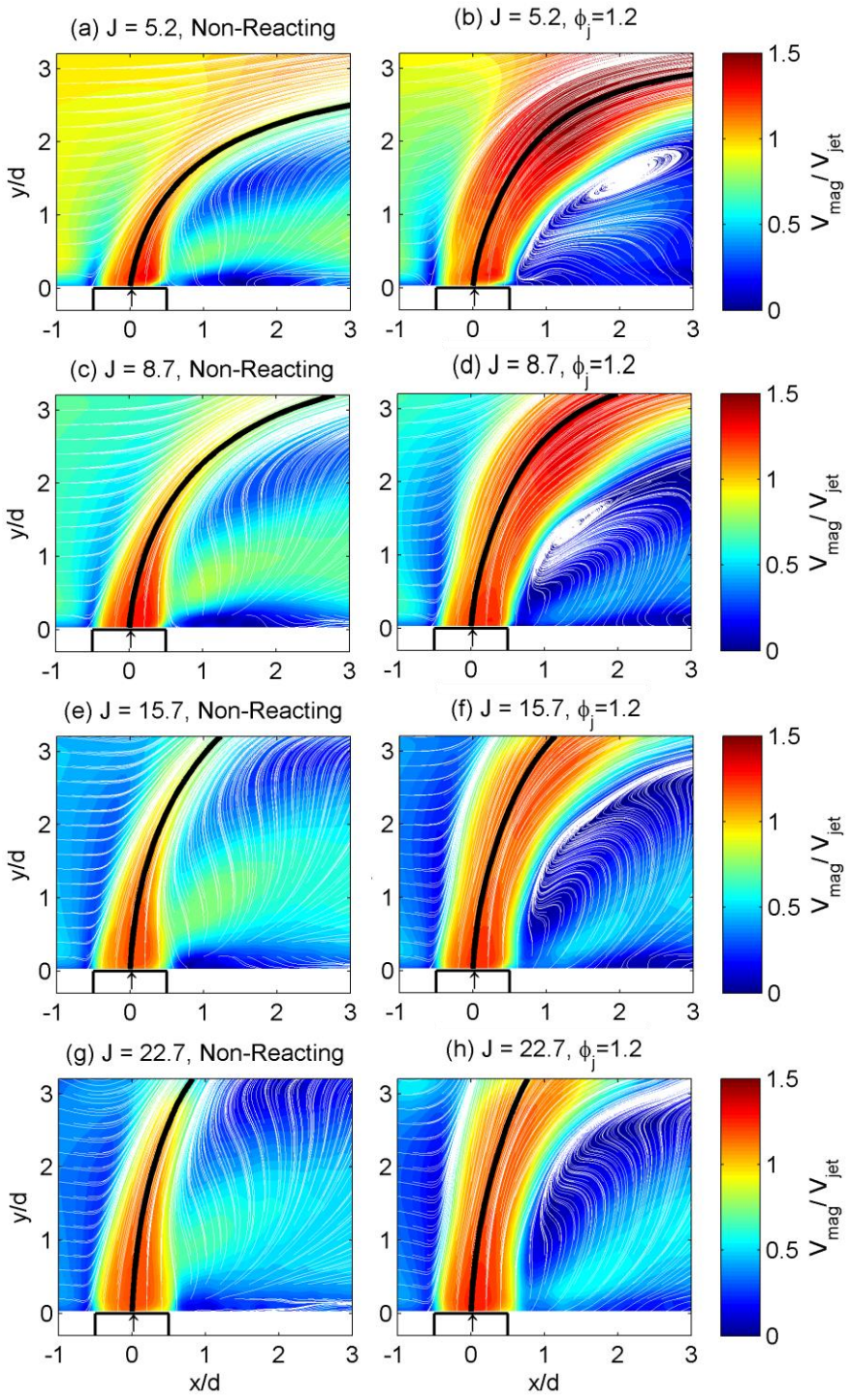


**Fig. 3.2: Average $V_{mag}/V$ for non-reacting and reacting $\phi_j = 1.2$ JICF with streamlines overlaid in white and jet center streamline overlaid in black.**

The wake behavior, shown in Fig. 3.2, differed between the non-reacting and reacting JICF. In the non-reacting JICF average flow field, the wake behavior was characterized by mostly upright streamlines. These results are in good agreement with those presented in [52], [67]. In the case of the reacting JICF the wake streamlines behaved differently for varying *J*. For the $J = 5.2$ reacting JICF, there is a recirculation region that forms along the leeward jet boundary, centered at approximately $x/d=2$ and $y/d=1.5$. Similar recirculation behavior was observed by Schmitt et al. [52]. The recirculation region slowly disappears as the *J* is increased and vanishes completely when $J > 8.7$. For $J = 22.7$ differences between the non-reacting and reacting wake behavior become more subtle. Coincidentally, at this *J* value, the windward and leeward flame liftoff heights were highest. This suggests that upstream of the lifted flame the reacting JICF system behaves similarly to a non-reacting JICF. Similar observations were made by Hasselbrink and Mungal [48].

The apparent differences in wake behavior between the non-reacting and reacting JICF can be attributed to the differences in the behavior of the upright wake vortices under the two different flow conditions. For non-reacting JICF the upright wake vortices are the primary mixing mechanism responsible for entrainment of crossflow fluid in the jet wake near-field. As shown by Fric and Roshko [6], the upright wake vortices result from the entrainment of crossflow boundary layer fluid by the jet. For a non-reacting JICF the strong adverse pressure gradient caused by the jet column forces the crossflow boundary layer to separate from the bottom wall near the sides of the jet. The vortex elements that separate from the wall get entrained by the jet, creating tornado-like vortices that stretch from the crossflow boundary layer to the jet column. When time-averaged behavior is examined, the influence of the wake vortices is seen by upright streamlines as shown in Fig 3.2.

In-depth investigation into the reacting JICF wake has not been conducted thus far, and so a possible explanation of the behavior is presented here. From the streamlines displayed in Fig. 3.2, it is

apparent that the presence of the upright vortices may be diminished or even non-existent for the reacting JICF. As depicted by the average chemiluminescence images in Fig. 3.1, the jet wake is comprised mostly of low-level signal (<10% maximum heat release), which is most likely luminosity from combustion products. Along the windward jet trajectory the crossflow stagnates strongly against the jet, which minimizes the ability of the reacting jet to expand upstream, as evidenced by the tightly spaced contours. Along the leeward jet trajectory the contours are spread much farther apart, indicating that there is much less resistance against jet expansion in the jet wake. This also suggests that crossflow entrainment is significantly reduced in the reacting jet wake. The combustion products in the wake cause an increase in the jet wake pressure, relative to that of a non-reacting JICF, which then prevents entrainment of crossflow fluid. As a result, the reacting JICF appears to behave more like a solid cylinder than a non-reacting jet, with strong recirculation in the wake. Because the maximum heat release region is closest to the jet exit for $J$ = 5.2, the wake behavior is most significantly altered at this condition. For increasing $J$, the maximum heat release regions moves away from the jet exit, and therefore so does the high pressure region downstream of the jet. At these high $J$, the jet wake resembles behavior similar to both non-reacting and reacting JICF.

Comparisons between the average vorticity in the non-reacting and reacting flow fields were made and the results are shown in Fig. 3.3. Overlaid on the vorticity in Fig. 3.3 are the windward, centerline, and leeward streamlines, which provide a sense for the boundaries of the bulk jet flow. The high vorticity along regions along the windward and leeward streamlines represent the windward and leeward shear layers, respectively. Under reacting conditions, the length of the shear layers increased relative to the length of the non-reacting shear layer. Comparison between Figs. 3.2 and 3.3 shows that the windward shear layer corresponds well with the location of the stagnation region ahead of the jet. Along the stagnation region, $\frac{\partial u}{\partial y}$ ~0, and as a result, vorticity is highest here. The reacting leeward shear

layer stretches further, and is wider than, the non-reacting shear layer, which is in agreement with the observations of Lyra et al. [68]. As described earlier, the wake structure of the reacting JICF was noticeably different than the wake structure of the non-reacting JICF, which in turn affected the leeward shear layer behavior. Lower flow velocity in the reacting jet wake resulted in higher shear between the jet and wake, which attributed to the higher vorticity along the reacting leeward jet shear layer.

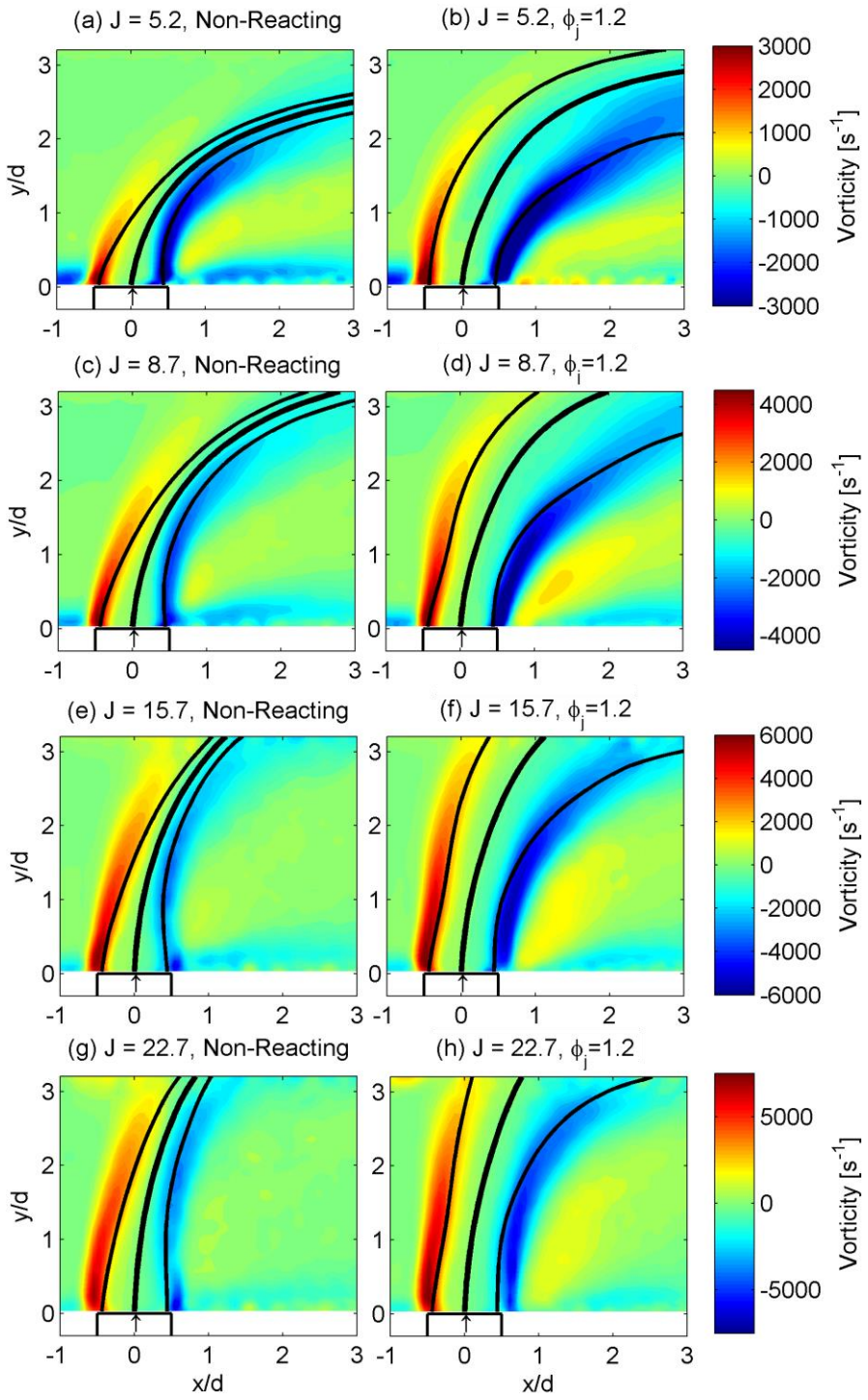


**Fig. 3.3: Average vorticity for non-reacting and reacting $\phi_j$ = 1.2 JICF with windward, jet center, and leeward streamlines overlaid in black.**

### *3.1.3 JICF Trajectory & Scaling*

One of the most desired traits of the JICF configuration is the rapid and thorough mixing that takes place between jet and crossflow. For applications related to gas turbine combustors, quick mixing is essential for creating temperature uniformity, reducing $NO_x$ production, and minimizing combustor size. Several studies have shown jet penetration is one of the key metrics that determines the JICF mixing efficiency [34], [37]. Historically, the jet penetration has been determined by measuring the trajectory of velocity, temperature, or other scalars. From these measurements jet trajectory correlations have been developed. For non-reacting JICF the correlations generally take the form of eq. (1)-(2); however, reacting JICF correlations have yet to be developed. In this section, an experimental reacting jet trajectory correlation is presented, computed using the high speed PIV measurements of the $\phi_j$ =1.2 JICF. In addition to the reacting jet correlation, a correlation was developed for the non-reacting JICF. The classical non-reacting jet trajectories, eq. (1)-(2), have shown strong agreement for unconfined JICF, but the accuracy of these correlations for predicting highly confined JICF penetration behavior, as that studied here, has yet to be determined. The lateral confinement of the JICF for the experiments presented in this section was $H/d$=4; traditional experimental JICF confinement can vary from $H/d$=50 to completely unconfined JICF.

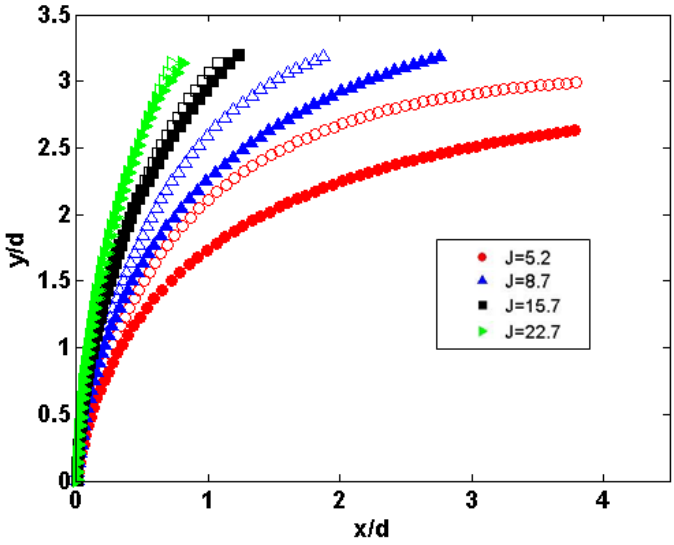


**Fig. 3.4: Non-reacting (closed symbols) and reacting (open symbols) JICF trajectories.**

The streamline with origin at the jet center was used to define the jet centerline and jet trajectory. The average jet trajectories for JICF at various $J$ under non-reacting and reacting conditions are shown in Fig. 3.4. For the $J$ range tested, the reacting jets penetrated further into the crossflow than the non-reacting jets. This result is consistent with that seen by Hasselbrink and Mungal [48]. As $J$ increased, the difference in penetration depth between non-reacting and reacting jets was minimized, and at $J$ = 22.7, the reacting jet trajectory was only slightly more penetrating than the non-reacting jet. The increased penetration for the reacting JICF is a result of the slower jet velocity decay and jet expansion. Evolution of jet centerline velocity extracted from the local velocities along the center streamline for non-reacting and reacting JICF is shown in Fig. 3.5a. For each $J$, the reacting jet centerline velocity increases above the non-reacting jet velocity beyond a certain value of $y/d$. This location $(y/d)_{RZ}$, corresponds to the point at which the jet centerline crosses the reaction zone. For increasing $J$, $(y/d)_{RZ}$ moved farther away from the jet exit.

For the non-reacting jet the dilatation along the jet centerline was negative, indicating that the crossflow was, in effect, compressing the jet. At $J$ = 22.7 the sharp decrease toward even further negative dilatation was a result of the jet column approaching the opposing wall. On the other hand, for $J$ = 5.2 the dilatation at the end of the jet trajectory was near-zero, as the jet has almost entirely mixed away with the crossflow. For the reacting JICF the centerline dilatation behavior changes, due to the heat release from combustion. Starting from the jet exit ($y/d$ = 0) there is a sharp decline in dilatation, which continues until the minimum dilatation is reached at approximately $500s^{-1}$. The $y/d$ location at which the minimum is located varied only slightly with $J$ value, occurring near $y/d$ = 0.5. A gradual increase in dilatation follows as the jet reactants begin preheating upstream of $(y/d)_{RZ}$. At $(y/d)_{RZ}$ the dilatation becomes positive, and hence the jet velocity increased. The increased continued until a maximum was reached. The location of maximum dilatation shifted farther from the jet exit as $J$ value increased and the gradual decrease in dilatation after the maximum was a result of crossflow entrainment by the jet.

The most significant increase in velocity at $(y/d)_{RZ}$ occurred when $J$ = 5.2; and as $J$ increased the apparent increase in velocity reduced. For $J$ > 8.7 no velocity increase across the flame edge was observed; however, the decay rate of the reacting jet centerline velocity slowed significantly relative to the non-reacting jet. The effects of confinement are most likely the cause of the smaller velocity increase across the flame edge for $J > 8.7$. As $(y/d)_{ZR}$ approaches the wall, confinement of the jet prevents the flame from expanding, as was the case for the flames when the $J$ < 15.7. The effect of the centerline velocity on jet penetration is clearly seen by these results. For $J$ = 5.2, the heat release has the strongest effect on jet velocity, and thus reacting jet penetration. On the other hand, the effect of heat release on centerline velocity is weakest for $J$ = 22.7, and consequently the jet penetration only slightly increased.

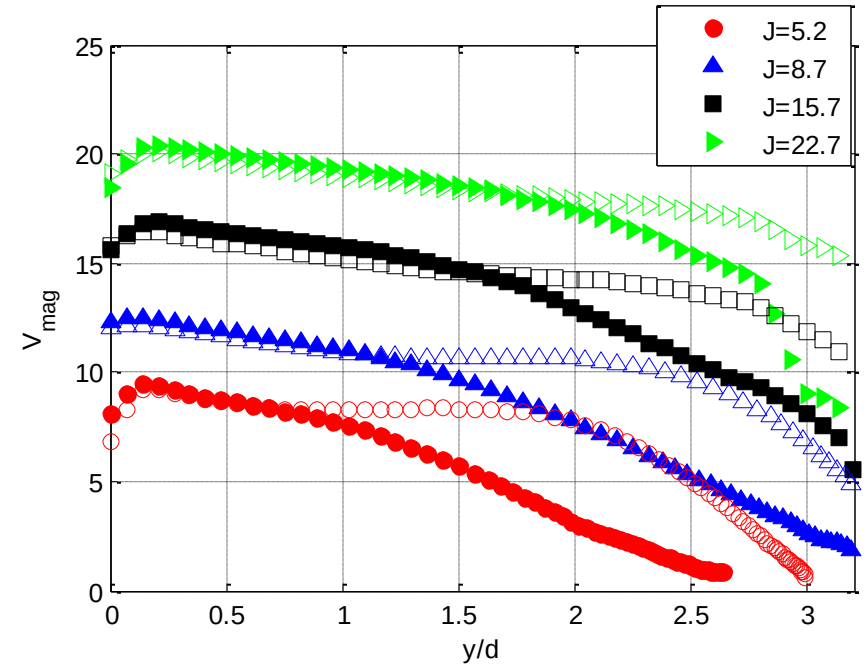


(a)

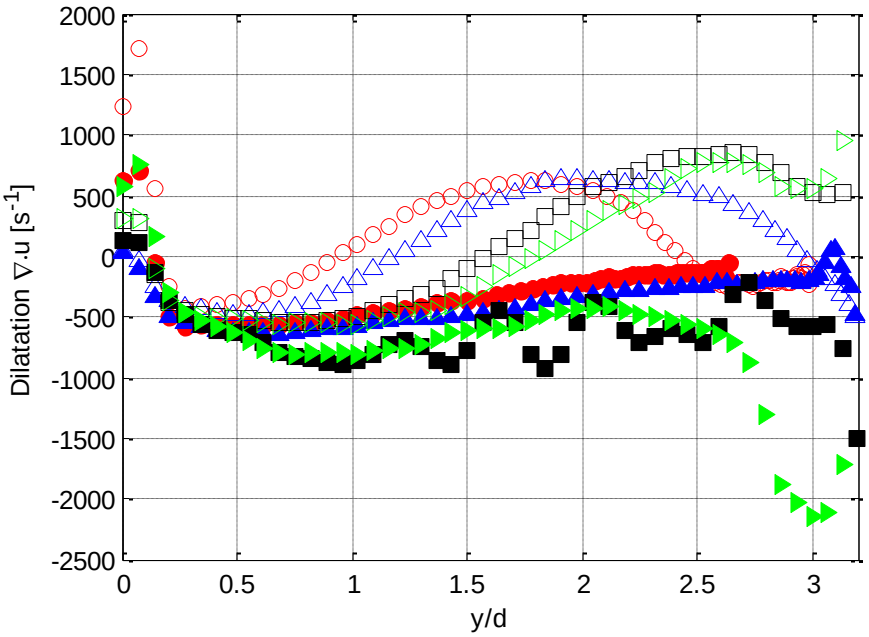


(b)

**Fig. 3.5: Non-reacting (closed symbols) and reacting (open symbols) JICF centerline (a) velocity and (b) dilatation along the *y/d* axis.**

Velocity decay of the non-reacting and reacting jets from Fig. 3.5(a) are normalized by the exit velocity in Fig. 3.6(a)-(b) and compared to a typical centerline velocity decay rate of $s^{-1}$ for a free

turbulent jet, where $s$ is the length parameter integrated along the jet trajectories taken from Fig. 9. For non-reacting JICF the $s^{-1}$ free jet scaling matched the JICF behavior in the region of $1 < s/d < 3$. For reacting JICF, the free jet scaling occurred over a smaller range, $1 < s/d < 2$. Upstream of the jet-like region, the velocity decay is slow indicating potential core flow behavior. Downstream of the region where jet-like behavior is observed, Han and Mungal [47] proposed a JICF wake like scaling of $s^{-3}$. The experimental centerline velocity decay of the JICF at $J < 15.7$ exhibited this same $s^{-3}$ scaling downstream of the jet like region; however, for $J = 15.7$ and $J = 22.7$, the effect of confinement caused jet interaction with the opposite wall prior to observing a wake like behavior. For the reacting jet at $J$=5.2, shown in Fig 3.6b, an increase in the centerline velocity occurs before the jet transitions into the jet like region, a result of the heat release.

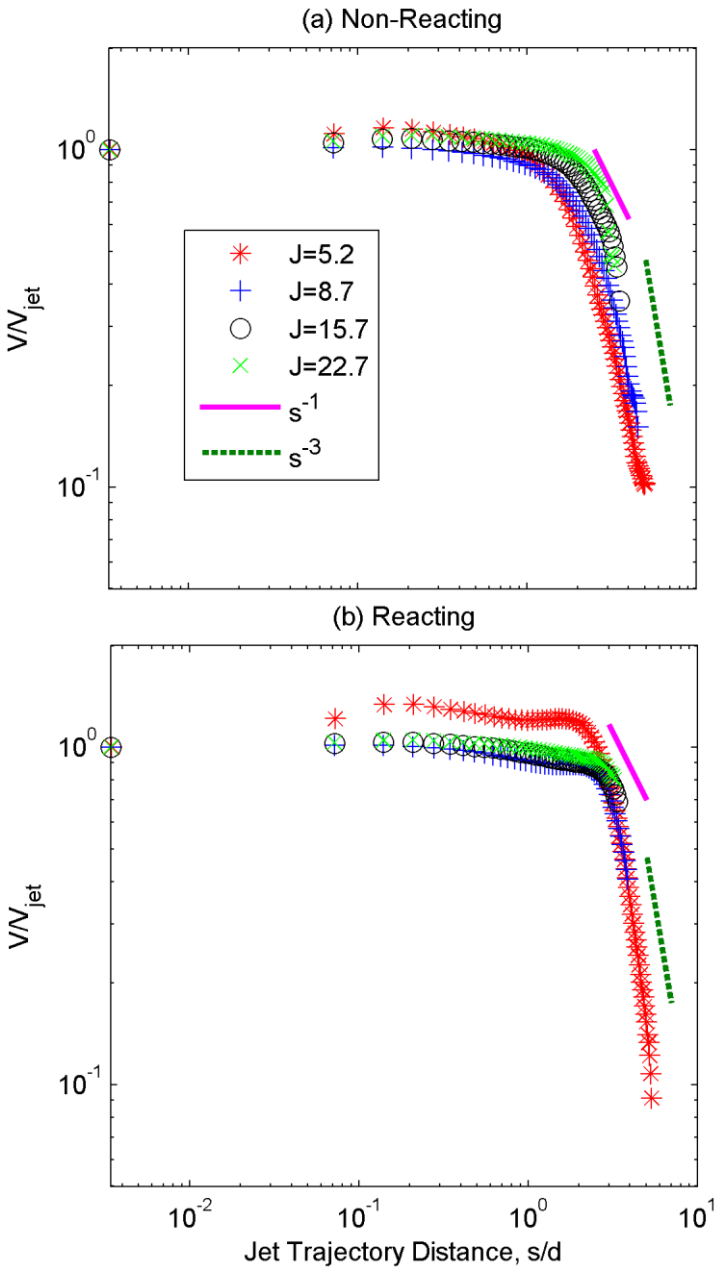


**Fig. 3.6: Velocity decay along jet centerline relative to free jet behavior for (a) non-reacting and (b) $\phi_j$ = 1.2 JICF.**

Several correlations of jet trajectory, as defined by eqs. (13)-(14), were tested to develop best fits to the data from Fig. 3.4. It was found that the trajectory data did not collapse well using the more classic $\sqrt{J}d$ scaling; additional dependence on $J$ was required. The data were found to collapse best when

using $X = xJ^C/d$ and $Y = y/\sqrt{J}d$ scaling. This scaling is consistent with that found by Kamotani and Greber [11] as shown in eq. (3). An iterative process was used in Matlab to minimize the variance between the data and the correlation to determine the constant C that collapsed the data best. Once the constant C was determined, which defines the trajectory dependence on *J*, a power fit defined by eq. (14) was matched to the data. Iteration was used to find the A and B constants for determining the line of best fit. The values of best fit were A=1.69, B=0.74, C=-0.015, E=1.2 for non-reacting jets and A=1.93, B=0.77, C=-0.205, E=0.9 for reacting jets.

Generally, power fits have been found to accurately describe JICF trajectory; however, the power fit correlation, eq. (13), was unable to accurately capture the experimental JICF trajectory, as shown in Fig. 3.7. In the jet near field, eq. (13) under-predicted the jet penetration, and in the jet far field over-predicted the jet penetration. The trajectory defined by eq. (13) does not account for the effect of the opposing wall on the jet trajectory, as power law fits were developed for mostly unconfined configurations or configurations with large *H/d* (where *y* approaches infinity as *x* approaches infinity). In developing a new correlation, confinement effects on the JICF were considered by using an asymptotic correlation given by eq. (14). As shown in Fig. 3.7, the new correlation eq. (14) captures the JICF trajectory accurately.

$$Y = AX^B \tag{13}$$

$$Y = A\left(\frac{X^B}{X^B + E}\right) \tag{14}$$

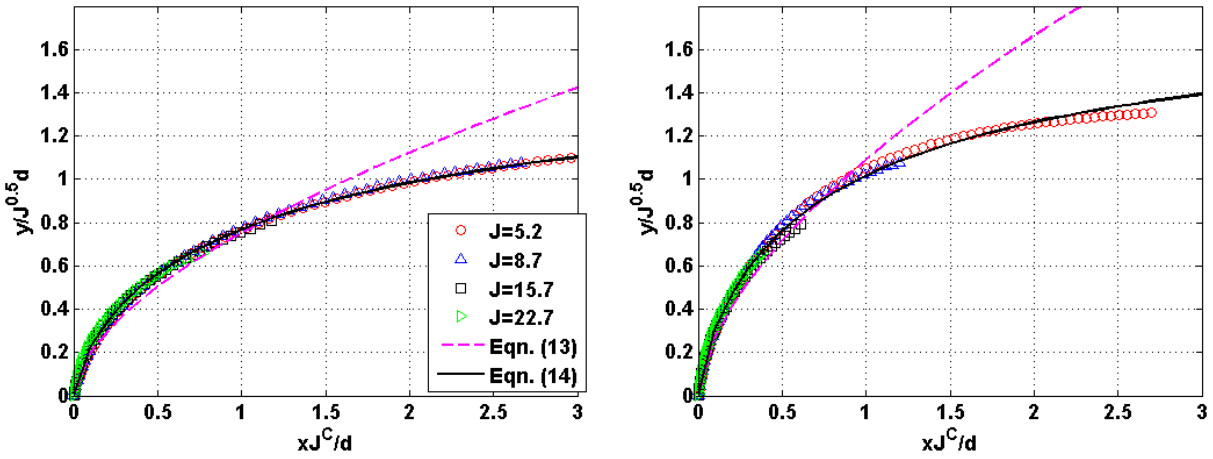


**Fig. 3.7: Lines of best fit for (a) non-reacting and (b) $\phi_j$ = 1.2 JICF trajectory.**

In Fig. 3.8, the asymptotic trajectories for reacting and non-reacting jets utilizing eq. (2-3) are compared with the correlations for non-reacting JICF found by Pratte and Baines [9], Kamotani and Greber [11], and Smith and Mungal [69]. In each of these prior experiments, *H/d* ratios far exceed *H/d*=4. Pratte and Baines [9] and Smith and Mungal [69] used the trajectory correlation defined by eq. (2) and Kamotani and Greber [11] used eq. (3). The correlation used by Kamotani and Greber [11] matched the experimental data the closest, however still over-predicted the non-reacting jet trajectory. Differences in jet trajectory correlations highlight the need for more rigorous trajectory definitions. As shown, confinement effects significantly impact the JICF trajectory; however few correlations take the *H/d* ratio into account. Additionally, separate correlations must be developed for reacting JICF which may take into account additional parameters such as flame stabilization location and total heat release.

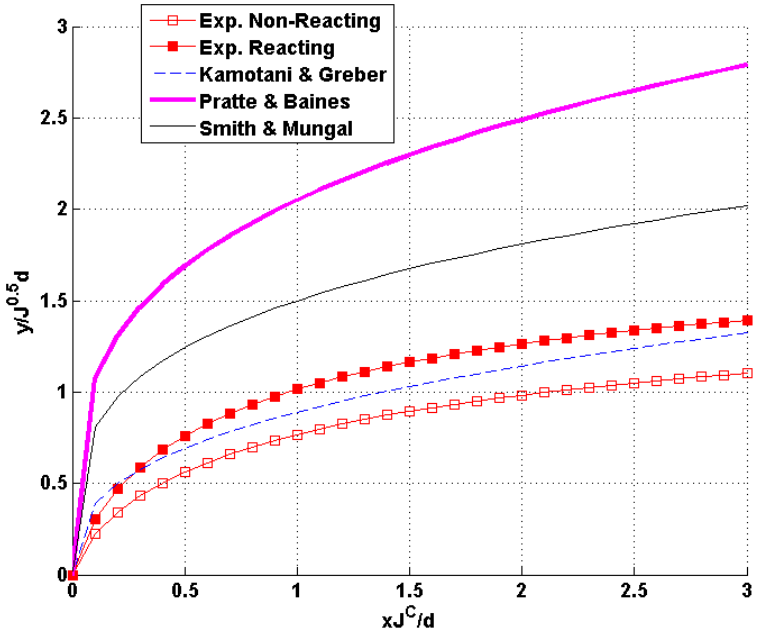


**Fig. 3.8: Comparison of experimental trajectory correlations with correlations found in literature.**

## 3.2 Instantaneous Flame and Flow field Behavior

### *3.2.1 Flame Behavior – High Speed Chemiluminescence Imaging*

Analysis of the instantaneous $\phi_j$ =1.2 JICF flame behavior was first conducted using high speed chemiluminescence imaging. The windward flame stabilization was characterized by three different behaviors: a fully attached flame, an unsteady lifted flame, and intermittent blowoff. Examples of these observed flame behaviors are shown in Fig. 3.9. Full flame attachment at the jet exit was observed most frequently for $J$ = 5.2; for $J$ > 5.2, the windward liftoff was the most frequently observed flame behavior and full flame attachment was never observed. The leeward flame base was located slightly lifted above the jet exit for all $J$ and was characterized by more consistent behavior, relative to the windward flame. Similar windward and leeward flame behaviors were also observed by Steinberg et al. [46].

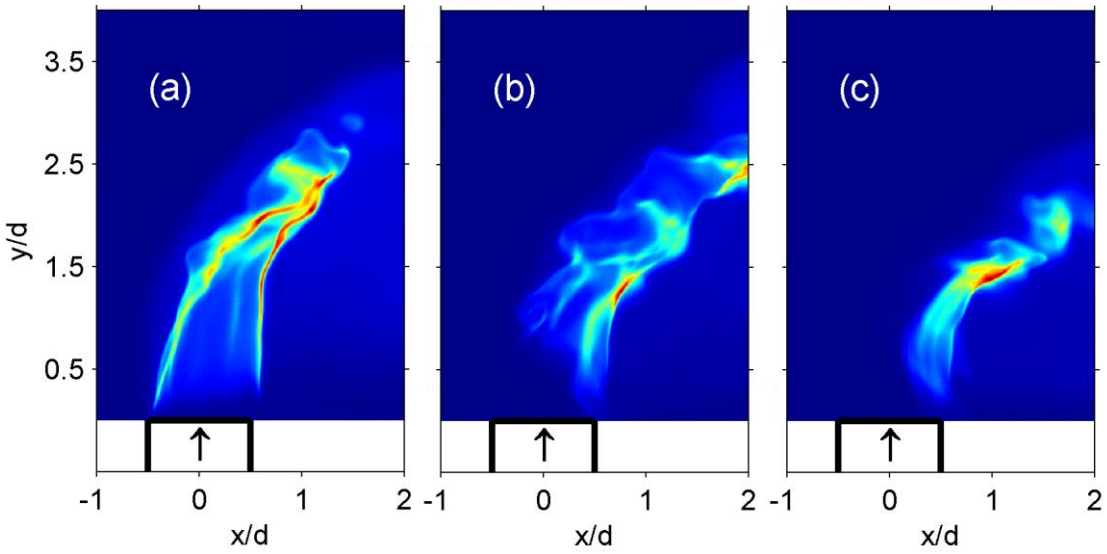


**Fig. 3.9: $J$ = 5.2 $\phi_j$ = 1.2 JICF high speed chemiluminescence frames showing observed instantaneous flame behaviors: (a) attached flame (b) lifted flame, and (c) windward blowoff.**

The time resolved imaging allowed for visualization of auto-ignition behavior in the reacting JICF flow field. The sequence of high speed chemiluminescence frames presented in Fig. 3.10 is an example of visual observation of auto-ignition. The sequence begins (Fig. 3.10(a)) where the windward flame base is lifted approximately 1.75*d* above the jet exit. The beginning of observable auto-ignition event begins in Fig 3.1(b)-(c) with very faint chemiluminescence signal appearing near the jet exit, isolated from the lifted flame base. In frames (d)-(h) the development of the auto-ignition kernel is characterized by stronger chemiluminescence intensity, increasing size, and convection towards the lifted flame front. The end of the auto-ignition sequence (i) occurs when the kernel merges with the lifted JICF flame. As *J* was decreased the frequency of observable ignition kernels decreased, due in part to the decreasing flame liftoff. This does not necessarily suggest that auto-ignition did not occur for lower *J*, only that clear visualization of auto-ignition kernels did not happen. The longer liftoff associated with high *J* allowed for larger growth of the ignition kernels prior to merging with the lifted flame front. More vigorous mixing between the jet mixture and hot cross flow also increased the possibility of auto-ignition in the lifted windward flame regions at high *J*.

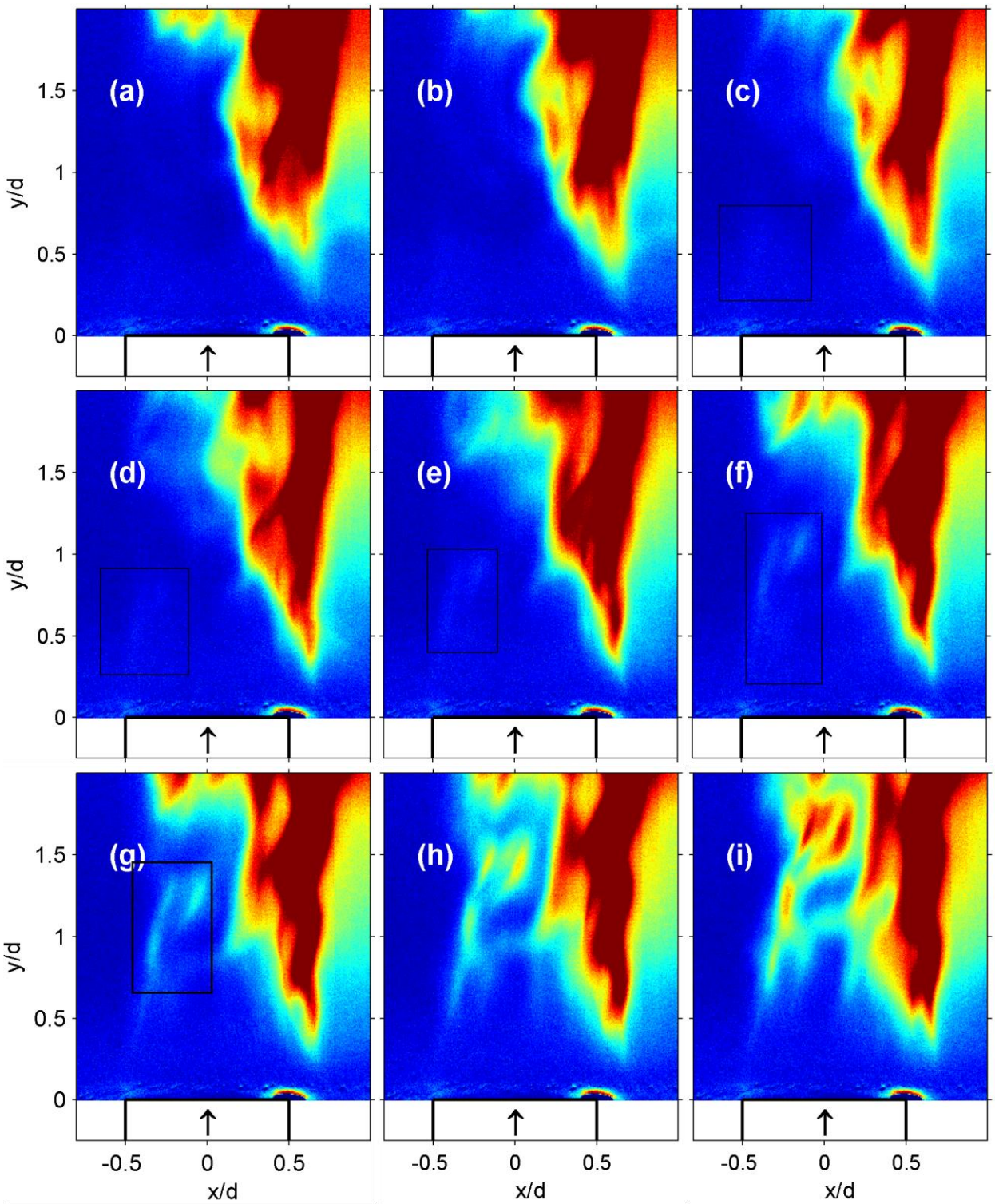


**Fig 3.10: Auto-ignition behavior shown by high speed chemiluminescence images of $J$ = 22.7 $\phi_j$ = 1.2 JICF. Total elapsed time over 9 frames shown is approximately 1 ms.**

The average windward and leeward flame liftoff heights for the $\phi_j$ =1.2 JICF are shown in Fig 3.11(a). The instantaneous windward and leeward flame stabilization points were computed using the method described in *Section 2.5.1*, and the average of all the instantaneous points was determined. Overlaid onto the average flame location in Fig. 3.11(a) are *x/d* and *y/d* error bars representing one standard deviation. The trends show that the windward flame liftoff height increased with increasing *J*. Additionally, the average windward flame stabilization location moved toward the windward jet exit *x/d* = 0.5 with increasing *J*; which is a direct result of the change in jet penetration. As *J* increased, the windward error bars in both *x/d* and *y/d* shortened, indicating the flame position was more consistent. At higher *J*, the ability of the crossflow to influence jet behavior was weakened, so the increased windward flame unsteadiness at low *J* value was most likely a result of jet fluctuations caused by the interaction with the crossflow. The leeward flame stabilized much closer to the jet exit and the stabilization position was much more consistent than the windward flame location. Along the leeward flame edge the influence of the crossflow is weaker and recirculation of hot combustion products allows for more consistent flame anchoring.

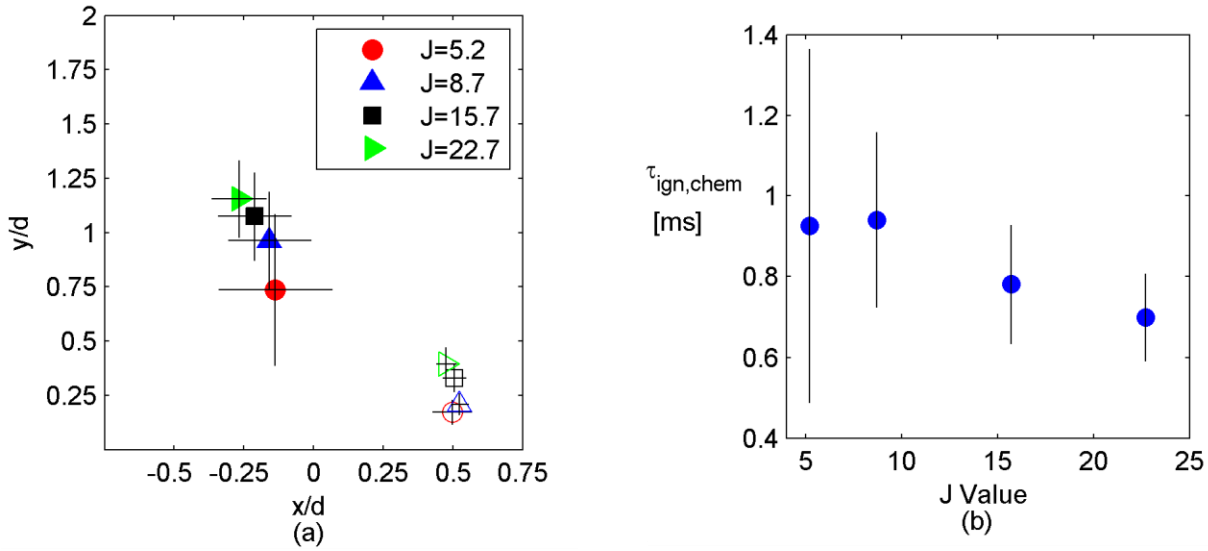


**Fig. 3.11: $\phi_j$ = 1.2 JICF (a) average windward (closed symbols) and leeward (open symbols) flame liftoff heights and (b) average ignition time based on windward flame liftoff height.**

In Fig. 3.11(b) an ignition timescale $\tau_{ign,chem} = \frac{y_{Lifted,w}}{V_{jet}}$ as a function of *J* is shown, where $y_{Lifted,w}$ is the average windward liftoff height. This analysis is similar to that conducted by Sullivan et al. [45]. For the non-premixed JICF in [45], the ignition timescale for the varying jet mixtures was first determined numerically using plug flow reactor simulations. The experimental timescales, computed as$\tau_{ign,chem}$, agreed well with numerically calculated values, such that the experimental ignition delay time was independent of *J*. This suggested that the dominant stabilization mechanism for the non-premixed flame in vitiated crossflow was auto-ignition. The results shown in Fig. 3.11(b) suggest that the average ignition time was not consistent for the varying *J*, and for *J* = 22.7 the average ignition time was nearly 25% faster than for *J* =5 .2 and *J* = 8.7. At *J* = 5.2 ignition times variations were largest, based upon the size of the standard error bars. The results suggest one of two possibilities: (1) auto-ignition was not the dominant flame stabilization mechanism or (2) $\tau_{ign,chem}$ is not the proper way to characterize JICF auto-ignition. Further analysis presented later in this chapter will address both of these questions.

Non-reacting PIV measurements were used to study the flow field characteristics at the average flame stabilization locations obtained from chemiluminescence imaging. PIV data were taken from regions of interest centered at the average flame stabilization locations shown in Fig. 3.11(a). The width of the region of interest was selected as ± one standard deviation of the average flame stabilization location at each corresponding *J* value. For each instantaneous PIV image, the vector field statistics within the region of interest were averaged.

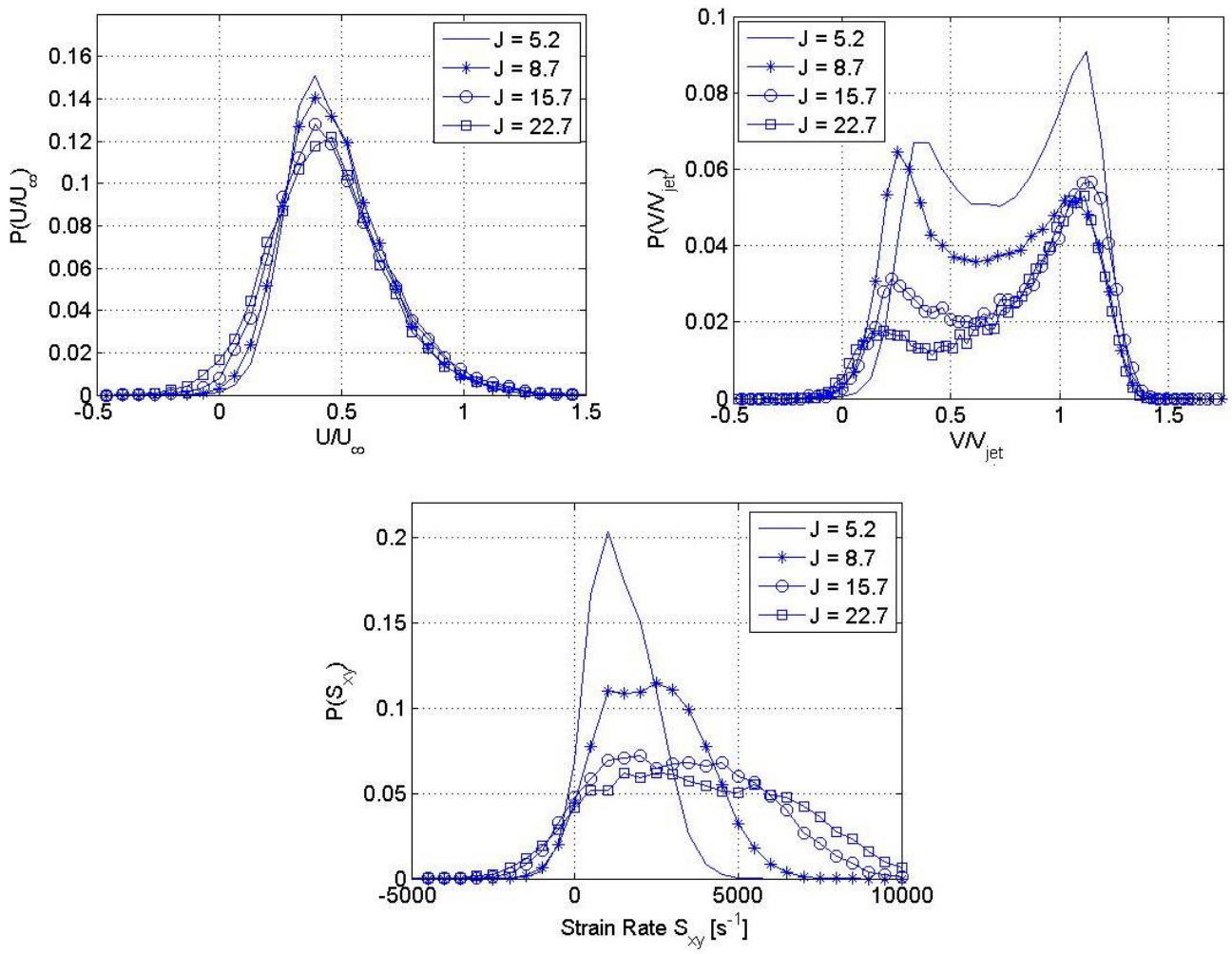


**Fig. 3.12: $\phi_j$ = 1.2 JICF probability distributions for $U/U_\infty$, $V/V_{jet}$, and $S_{xy}$ taken from non-reacting PIV measurements at average windward flame stabilization points shown in Fig. 3.11(a).**

Figure 3.12 shows the probability distributions (pdfs) that were computed for *u*- and *v*-velocity components and strain rate $S_{xy}$ at the average windward flame edge location. For each *J* the $V/V_{jet}$ pdf is characterized by two peaks, near 0 and 1. This suggests that the flame stabilization occurred along the shear layer, with highest probably of stabilization on the inner edge closest to the bulk jet flow. This is further evidenced by the probability distributions of strain-rate $S_{xy}$. As *J* increased the maximum strain rate along the shear layer increased, and thus, the pdf of strain rate broadened with increasing *J*. For

varying $J$, the pdfs of $U/U_\infty$ closely align, with a single peak near 0.4. This suggests that flame stabilization occurs in a region where $u$-velocity is consistent for all cases.

Figure 3.13 shows the probability distributions that were computed for $u$- and $v$-velocity components and strain rate at the average leeward flame edge location. Unlike the pdfs computed for the windward stabilization points, the $V/V_{jet}$ were characterized by a single peak. The leeward stabilization location varied only slightly with $J$; therefore, the location of the peak probability in $V/V_{jet}$ moved to the right as the $J$ increased. The $U/U_\infty$ pdfs were also characterized by a single peak and collapsed nicely for the varying $J$ values. With the highest probability at approximately $U/U_\infty$=-0.1 it is likely that the flame stabilized in a recirculating flow region in the jet wake. In Fig. 3.14 clear flow recirculation is observed in the jet wake especially in the vicinity of the flame base. Flow recirculation is particularly important for flame anchoring [10], [19], [46], [70], especially when the recirculating mixture contains hot combustion products.

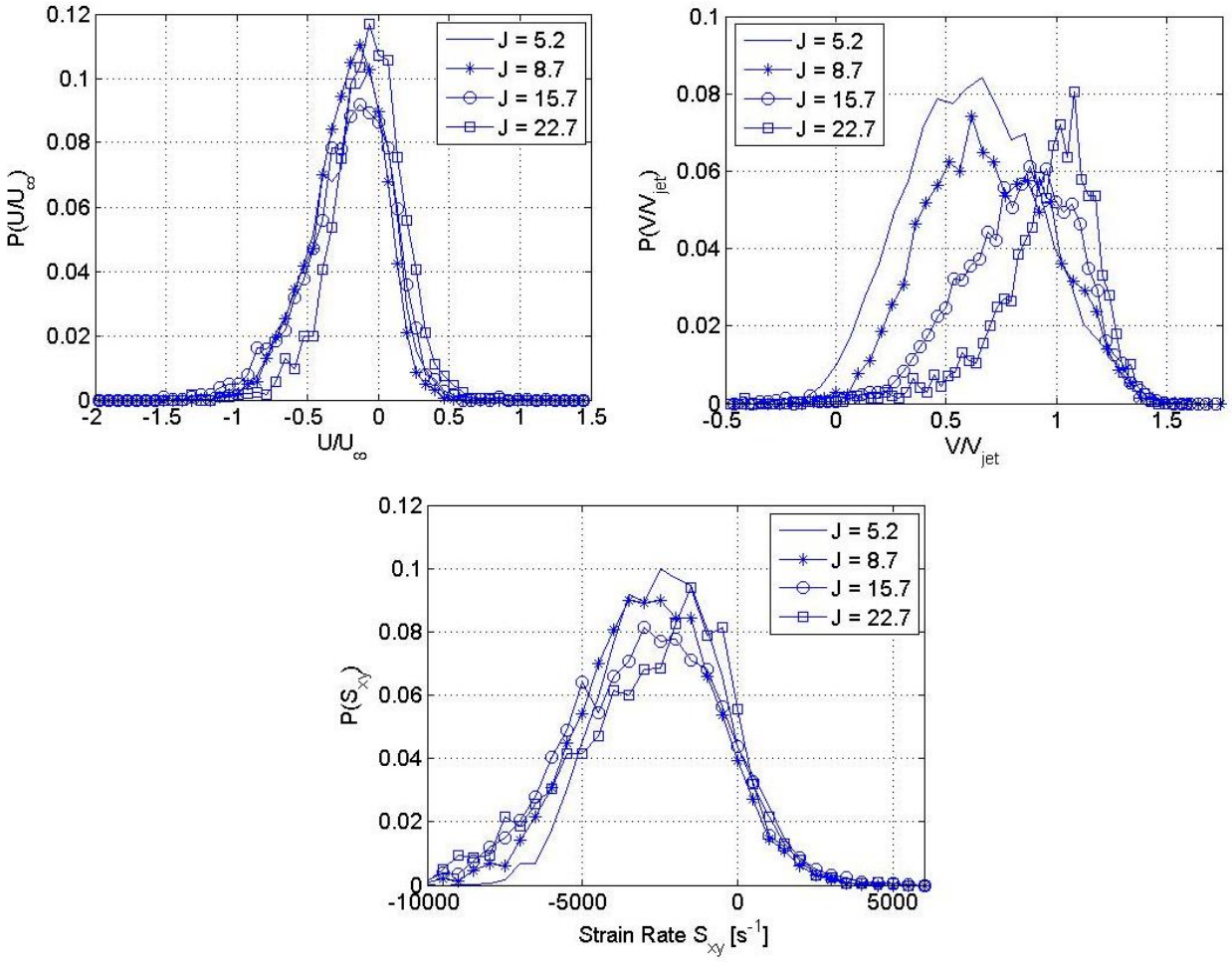


**Fig. 3.13: $\phi_j$ = 1.2 JICF probability distributions for $U/U_\infty$, $V/V_{jet}$, and $S_{xy}$ taken from non-reacting PIV measurements at average leeward flame stabilization points shown in Fig. 3.11(a).**

Steinberg et al. [46] likened the JICF leeward flame stabilization behavior to the commonly studied opposed-flow configuration, where strain rate is a commonly used parameter as a measure of residence time [15]. The probability distributions of strain-rate $S_{xy}$ shown in Fig. 3.13 aligned well for the varying *J* conditions. Opposed flow flame stabilization is highly dependent on equivalence ratio [71] and given that the jet equivalence ratio was held constant, it appropriately follows that the $\phi_j$ =1.2 JICF leeward flame is situated in a region where strain-rates were independent of *J*. For higher *J*, flame liftoff increases slightly as strain-rates near the jet exit are exceedingly high to support flame stabilization.

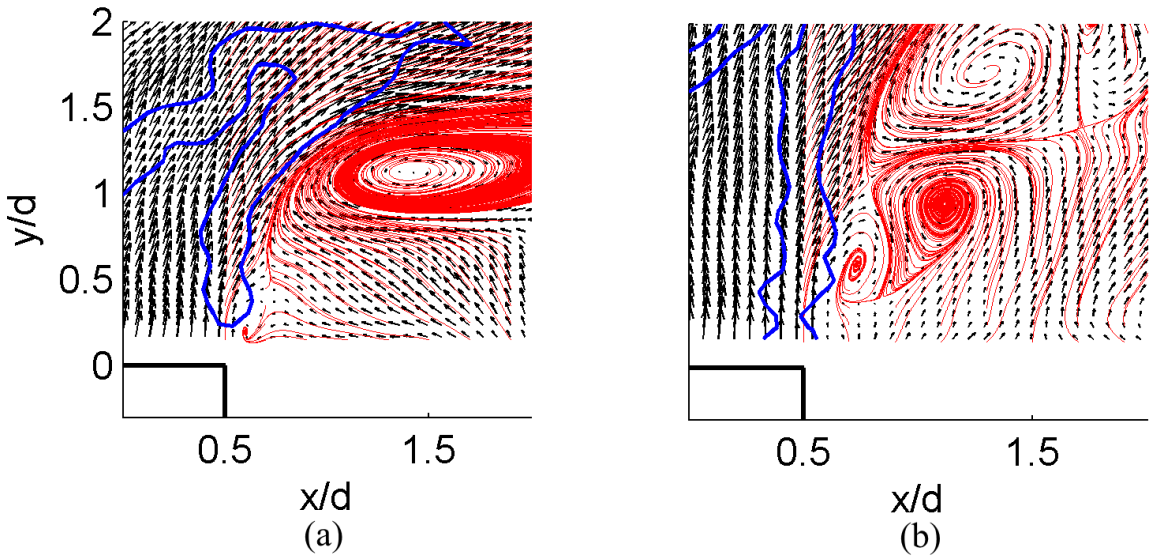


**Fig. 3.14: Instantaneous examples of recirculating flow behavior near leeward flame stabilization location for a) $J$ = 5.2 and b) $J$ = 15.7. The blue contour represents the 10% maximum dilatation isocontour and red lines represent jet wake streamlines in each instantaneous image.**

### *3.2.2 Flame Behavior – High Speed PIV*

The three instantaneous windward flame behaviors seen in the chemiluminescence images, and shown in Fig. 3.9, were also observed using the dilatation field, calculated from the high speed PIV measurements. The lifted, attached, and windward blowoff flame behaviors seen via dilatation are shown in Fig. 3.15(a)-(c). The flame region is marked by positive dilatation, with the 10% maximum dilatation contour at approximately $\nabla \cdot \vec{u}$ =250 $s^{-1}$ in each of the images. The background dilatation remains near $\nabla \cdot \vec{u} = 0$ $s^{-1}$. Along the windward and leeward shear layers, localized regions of negative dilatation existed. Negative 2-D dilatation can be an indication of (1) out-of-plane motion and/or (2) increasing density rate of change. In the windward jet nearfield, out-of-plane motion is significant, as the crossflow fluid is forced to flow around the jet column. Increasing density would result from high temperature combustion products mixing with crossflow or jet reactants, with the former most likely the case along the jet shear layer.

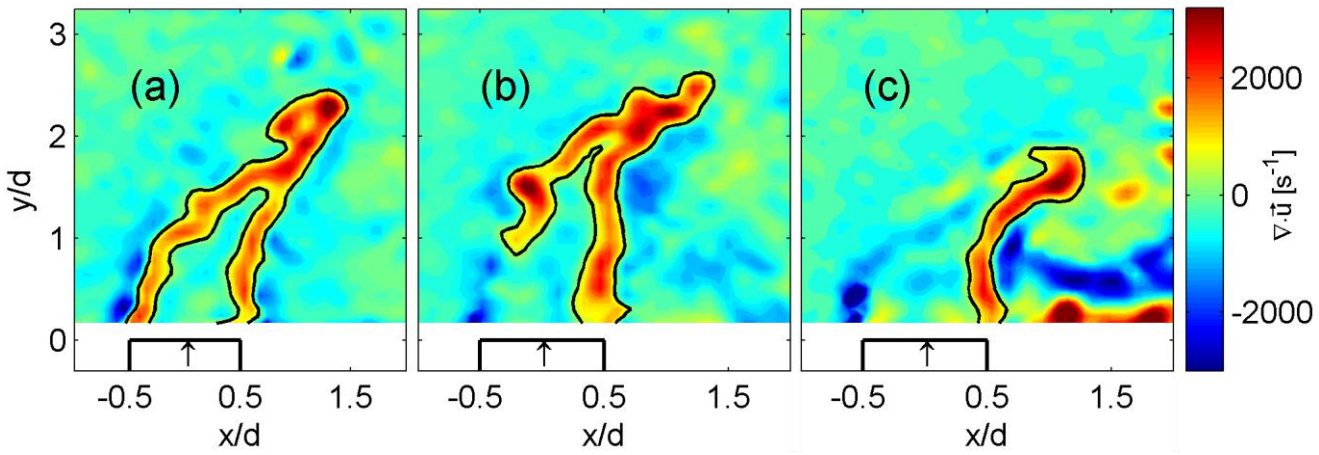


**Fig. 3.15: (a) $J$ = 5.2 and (b)-(c) $J$ = 8.7 $\phi_j$ = 1.2 JICF dilatation field showing observed instantaneous flame behaviors: (a) attached flame, (b) lifted flame, and (c) windward blowoff.**

A comparison between the average windward flame stabilization points determined using dilatation versus chemiluminescence imaging is show in Fig. 3.16(a). The average windward stabilization points identified using dilatation were consistently positioned closer to the jet exit than then those identified by chemiluminescence. For $J$ = 5.2, the discrepancy was most significant. In general, the flame stabilization trends were similar using the two different methods. The differences between them can most likely be attributed to the thresholding techniques utilized. The contour level in the chemiluminescence image is the 10% of the maximum path integrated signal contour, as a result of the line-of-sight imaging. On the other hand, the contour level chosen from the dilatation fields is the 10% of the maximum signal in the PIV plane. As a result, the flame boundary threshold in the chemiluminescence images may be slightly higher than that for the dilatation field, which would lead to more lifted stabilization point estimates.

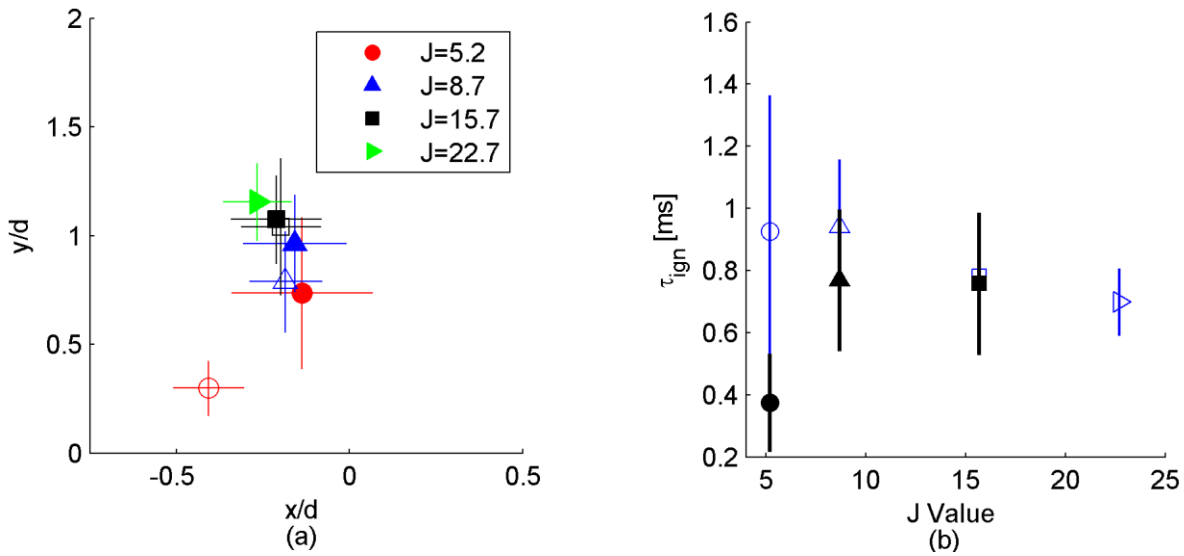


**Fig. 3.16: (a) Average windward flame stabilization points computed through chemiluminescence (open symbols) and average windward flame stabilization points computed using dilatation (closed symbols). (b) Average ignition time based on windward flame liftoff height.**

Ignition timescales were computed based on the flame stabilization locations determined using dilatation ($\tau_{ign,dil}$) and are compared with $\tau_{ign,chem}$ in Fig. 3.16(b). As expected, based on the stabilization locations in Fig. 3.16(a), the ignition timescales differ between the two methods. More importantly, the $\tau_{ign,dil}$ do not collapse for the varying *J* values, which agrees with the result for $\tau_{ign,chem}$. Again, this suggests that further analysis is required in order to determine the dominant flame stabilization mechanism.

Flame marking via dilatation allowed for comparison between the instantaneous flame and flow field behavior. Flow field information was extracted from a 2 x 2 mm region just upstream of the instantaneous windward flame stabilization location. The pdfs for velocity and strain rate $S_{xy}$, shown in Fig. 3.17 changed significantly when flow field statistics were conditioned on the instantaneous leading flame edge location, compared to results shown in Fig. 3.12. At $J$ = 5.2, two peaks were observed in the *v*-velocity pdf, indicating that there were times when the flame would sit on either edge of the shear layer. For $J$ > 5.2, the $V/V_{jet}$ pdf was characterized by a single peak, at $V/V_{jet}$ = 1. Unlike the $U/U_{\infty}$ pdfs

shown in Fig. 3.12, the $U/U_\infty$ pdfs shown in Fig. 3.17 didn't align well for the varying $J$. For $J$ = 5.2, the peak in the probability distribution of $U/U_\infty$ was near zero, and for increasing $J$ the peak shifted to higher $U/U_\infty$. As seen from the average velocity fields shown in Fig. 3.2, there is a small stagnation region just upstream of the windward jet exit. The strong peak near $U/U_\infty$ = 0 and the double peak $V/V_{jet}$ distribution confirms the experimental observations; the $J$=5.2 exhibited both attached and lifted flame behavior. The peak in $V/V_{jet}$ near 0.5 and $U/U_\infty$ =0 corresponds to flame attachment, where the flame anchors near the stagnation region; while the peak in $V/V_{jet}$ near 1 corresponds to lifted flame behavior, where the flame anchors along the inner edge of the shear layer.

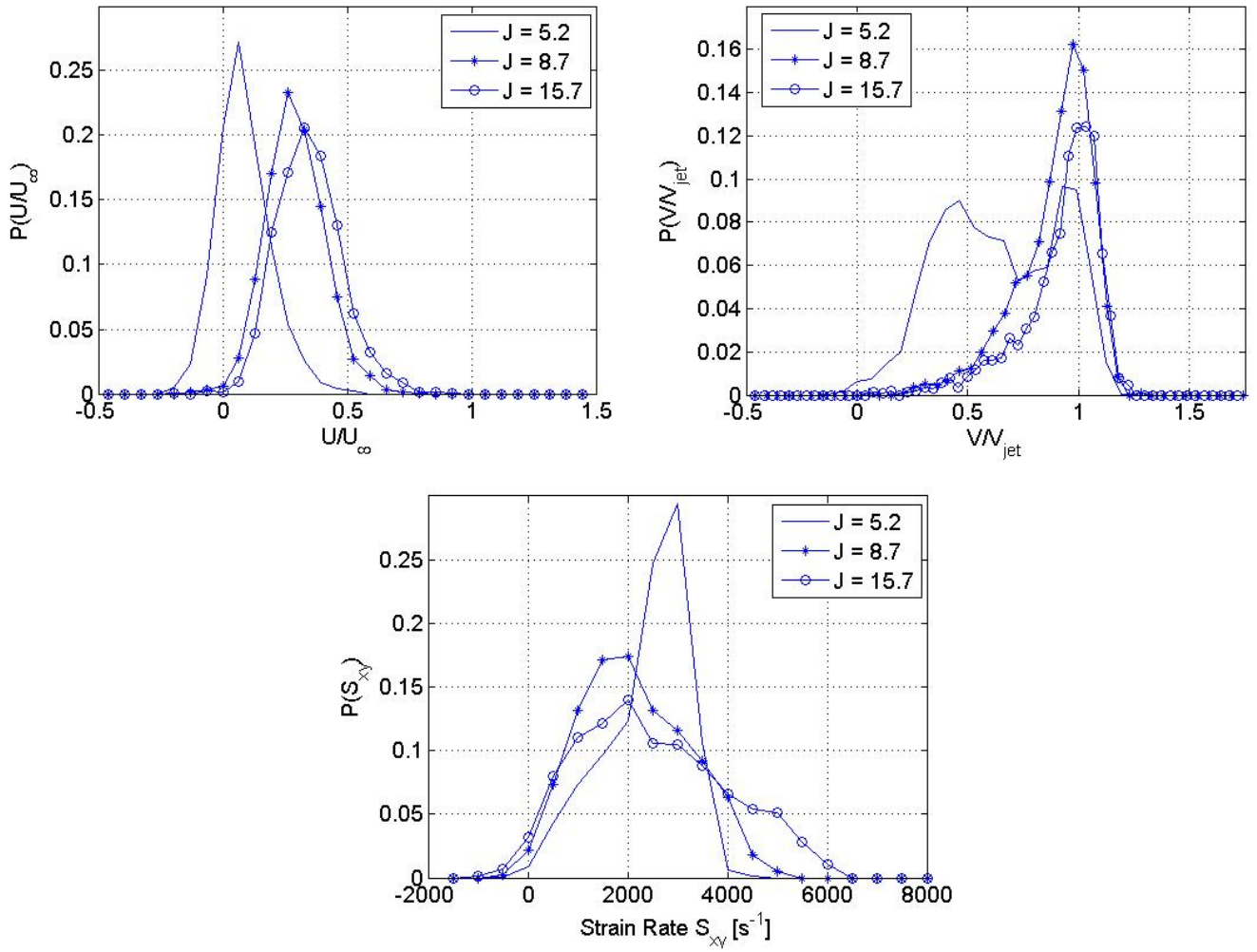


**Fig. 3.17: $\phi_j$ = 1.2 JICF probability distributions for $U/U_\infty$, $V/V_{jet}$, and $S_{xy}$ taken from reacting PIV measurements at instantaneous windward flame stabilization points.**

The distribution of strain rate at the instantaneous flame base shown in Fig. 3.17 was significantly narrower than that observed when using the average flame stabilization location in Fig. 3.12. The location of the peak probability in the strain rate pdfs in Fig. 3.17 shifted to lower values compared to the peak location in Fig. 3.12, and the distribution of strain-rate were more aligned for the varying *J* conditions. In Fig. 3.12, the strain rate distributions broadened significantly with increasing *J*; however, when the flow field statistics were conditioned on instantaneous flame location, Fig. 3.17, strain rates remained almost entirely below 6000 $s^{-1}$. The strain rate distributions based on the average

flame location, shown in Fig. 3.12, exceeded 6000 $s^{-1}$ for $J > 5.2$. The narrow strain-rate distribution, and shift to lower strain rates suggests that the flame stabilization behavior was correlated with strain rate.

Figure 3.19 details the various regions that make up the JICF flame. The first region of interest is region (i), where jet reactants and crossflow fluid mix upstream of the lifted flame front. Just beyond (i) is the windward flame stabilization point (ii), which sits on the inner edge of the shear layer, as denoted by the high strain rate. The flame surface downstream of the stabilization locations are indicated by (iii). This region of the flame surface (iii) sits well inside of the shear layer, evidenced by the increased distance from the high strain region. Downstream of (iii) is the post flame region, where mixing between the combustion products and crossflow occurs. The proximity of the windward flame stabilization point (i) to the shear layer suggests that jet-crossflow mixing may be a controlling parameter for flame stabilization. On the other hand, jet-crossflow mixing may have a significantly less effect on the flame surface (iii) that sits farther from the shear layer.

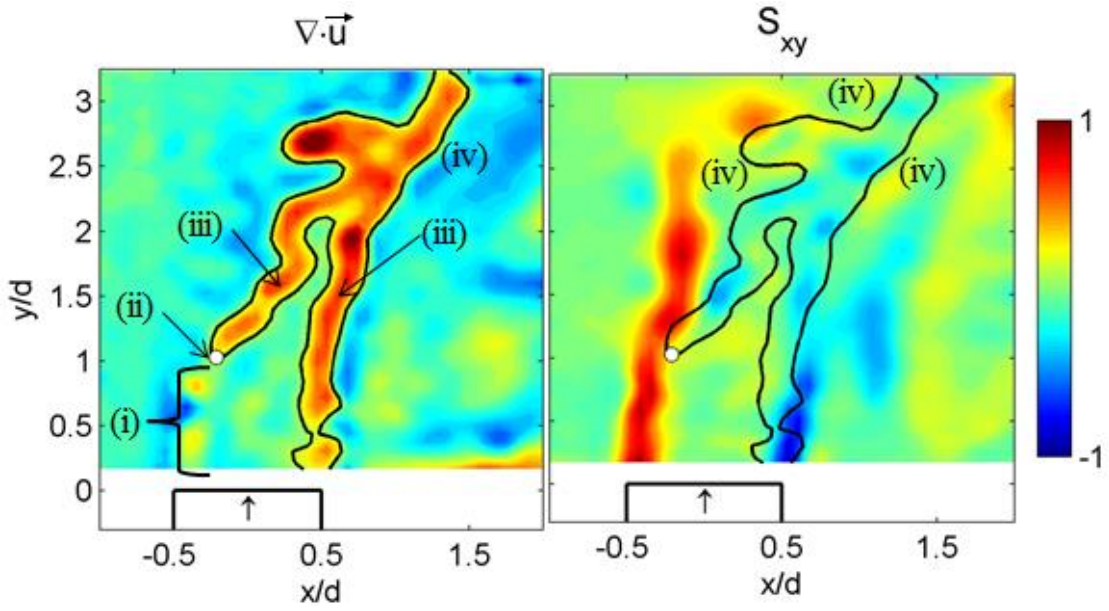


**Fig 3.18: Normalized instantaneous dilatation and strain-rate for $J$ = 8.7, $\phi_j$ = 1.2 JICF showing (i) jet reactant and crossflow mixing region, (ii) windward flame stabilization location, (iii) inner flame surface, and (iv) post-flame region. Dilatation normalization value was 3000 $s^{-1}$.**

Additional examples of the instantaneous flame and flowfield behavior are shown in Fig. 3.19, where the windward flame is lifted, with the liftoff height increasing with $J$. In each case, both the lifted windward flame and attached leeward flame appear to anchor along the inner edge of the shear layer. Flame surfaces away from the anchoring locations appear to sit inside the bulk jet flow. Flame anchoring near the shear layer suggests that jet and cross-flow mixing may impact flame stabilization behavior. For the inner flame surface, region (iii) in Fig. 3.18, jet and crossflow mixing may not be as critical and thus, the resulting flame stabilization mechanism would then most likely be premixed flame propagation. In this region, dynamic balance is achieved between the jet bulk velocity and the propagating flame front. Flame behavior in this region could be compared with the Bunsen flame tip behavior, which is described in detail in [15], [72].

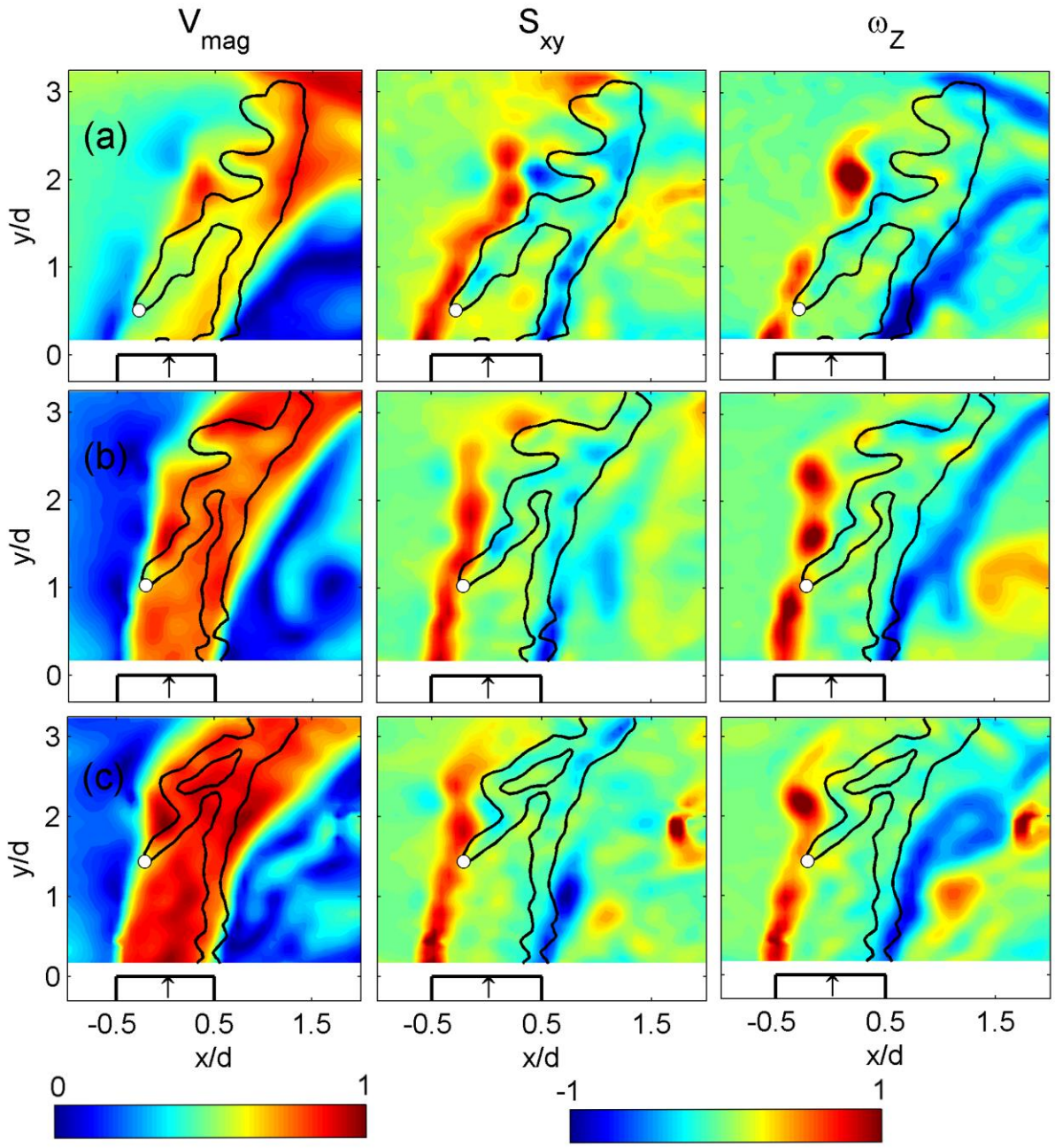


**Fig. 3.19: Instantaneous 10% maximum dilatation contour (black) and windward flame stabilization location (white) overlaid on $\phi_j$ = 1.2 JICF velocity magnitude, strain-rate, and vorticity fields for (a) $J$ = 5.2, (b) $J$ = 8.7, and (c) $J$ = 22.7. The normalization values for $V_{mag}$, $S_{xy}$, and $\omega_z$ were 15 m/s, 2200 $s^{-1}$, and 4500 $s^{-1}$, respectively.**

For analysis of the windward flame stabilization behavior, an experimental flame base propagation speed was determined based on the definition used by Upatnieks et al [73] as,

$$S_b = V_{flow} - V_{flame} \qquad (15)$$

While the previous work applied this to lifted non-premixed flames, the same approach of extracting an effective flame propagation speed from the current measurements can be used to assess if premixed flame propagation contributes to flame stabilization. The value for $V_{flow}$ was taken as the average *v*-velocity in the 2 x 2 mm region upstream of the instantaneous flame base and $V_{flame}$ was found by differentiating the instantaneous flame base location relative to time such that $V_{flame} = dy_{flame}/dt$. Central differencing was used to compute $dy_{flame}/dt$ where *dt* was 0.3 ms which is the reciprocal of the PIV acquisition rate of 3500 Hz. The flame speed pdfs in Fig. 3.20 follow no consistent trend for the *J* values shown, which suggest that flame propagation may not be the mechanism for the lifted flame stabilization. For *J*=5.2 the pdf is very narrow with a peak around 3 m/s and for *J* = 8.7 the profile broadened with a peak around 8 m/s. For *J*=15.7, no clear peak is observed and the profile is very broad extending to flame speeds above 20 m/s.

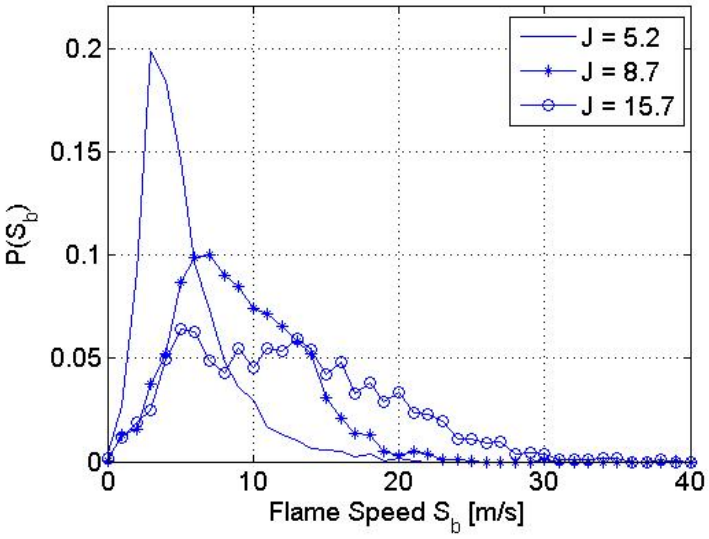


**Fig. 3.20: Experimental probability distribution of effective flame speed computed at instantaneous windward flame base locations in reacting dilatation field.**

Upatnieks et al [73] reported flame propagation speeds ranging from $0.7S_L^0$ to $1.1S_L^0$ at their lifted flame base, which would place the JICF flame propagation speed in the approximate range of $0.35 < S_b < 0.55$ m/s. Experimental flame propagation speeds far exceeded laminar flame speeds, which can be attributed to a number of factors. In the work of Upatnieks et al [73] no high temperature coflow was present as is in the JICF studied here. Mixing with high temperature crossflow can significantly increase the flame propagation speed beyond the laminar flame speed. No measurements were performed in the experiment to quantify the temperature of the mixture upstream of the flame base, thus no experimental temperature-flame speed relationship could be determined. Flame wrinkling and stretching due to turbulence can also increase the flame propagation speed beyond the laminar burning velocity [74]. More complete estimation for expected JICF flame propagation speed would require temperature and composition measurements ahead of the flame base, along with characterization of strain rates and turbulence intensities taken from PIV. Uncertainties in the experimental calculation of $S_b$ may also arise from differentiation of the flame base location. Nevertheless, the large variation in the pdfs of Fig. 3.20 with $J$, suggest that the effective flame speed is inconsistent with premixed flame propagation.

Experimental effective ignition delay times were also computed at the instantaneous windward flame stabilization location. Streamlines were traced backwards starting from the stabilization location to the jet exit. The ignition time was computed by dividing the length of the streamline by the average velocity along the streamline. Occasionally streamlines were traced back to locations other than the jet exit; in these instances the image was not used for ignition time calculations. For $J$ = 8.7 and $J$ = 15.7, 400 images were discarded, thus streamline information was kept from 1600 of the 2000 images. For $J$ = 5.2 only 10 of the 2000 images were discarded. Additionally, the instances when the flame fully attached were not used to compute ignition delay times. The pdfs of ignition delay time, Fig. 3.21, show

very similar distributions for all three momentum flux ratios. The pdf peak for $J > 5.2$ occurred at 0.15 ms while the pdf peak for $J = 5.2$ is located at 0.09 ms.

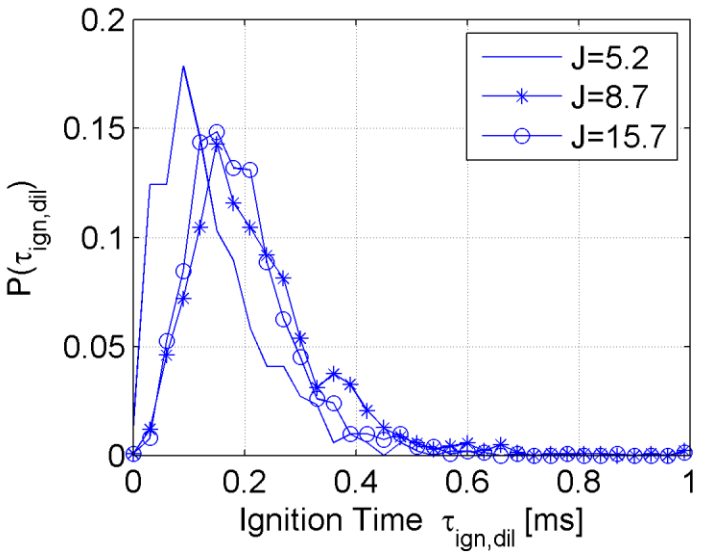


**Fig. 3.21: Ignition delay time probability distribution computed at instantaneous windward flame base locations in reacting dilatation field.**

In the JICF flowfield, mixing along the jet shear layer leads to heat transfer from the high temperature vitiated crossflow to the fresh reactants; if the mixing residence time is sufficiently long, auto-ignition can occur as observed in the high speed chemiluminescence images. Based on the ignition delay time pdfs shown in Fig. 3.21 auto-ignition is most likely the dominant mechanism for flame stabilization for $J > 8.7$. For $J = 5.2$ the ignition delay time with highest probability was 40% faster than for $J > 5.2$. Flame propagation allows the flame to stabilize close to the jet exit, such that there is insufficient time for auto-ignition to occur. In this case, the experimentally calculated ignition delay time would significantly decrease (causing the pdf to shift to the left). Auto-ignition may still in occur in the instances where the flame is lifted far from the jet exit, as probability of experimental ignition delay time at 0.15ms was still high.

The strain rate pdfs shown in Fig. 3.17 suggested that the flame stabilization behavior was coupled with strain rate. Scalar dissipation rate is generally used for studying auto-ignition behavior; Mastorakos [19] has shown that strain rate is a relatively good indicator of scalar dissipation. High scalar dissipation and high strain rate can inhibit auto-ignition because mixing occurs too fast and mixture residence times are too short. Too low scalar dissipation, and strain rate, can delay auto-ignition due to lack of mixing between high temperature fluid and reactants. From Fig. 3.17, for $J > 5.2$ the strain rate with highest probability was approximately $2000s^{-1}$, and for $J = 5.2$ it was $3000s^{-1}$. Probability of near-zero strain rates and strain rates exceeding $6000s^{-1}$ was low, as strain rates of those magnitudes indicate insufficient and too rapid of mixing, respectively.

### 3.3 Summary & Conclusions

In this chapter the time-average and instantaneous flame was examined for a $\phi_j = 1.2$ JICF at varying $J$ value conditions. Diagnostic techniques included high speed chemiluminescence imaging and high speed 3.5 kHz PIV. From these measurements the following conclusions regarding the flame stabilization were made:

- Two distinct flame branches existed: a leeward flame branch and a leeward flame branch.
- The leeward flame branch stabilized near the jet exit and was characterized by consistent behavior.
- The windward flame branch exhibited highly unsteady behavior which included: full flame attachment, unsteady lifted flame behavior, and windward blowoff.
- Flow recirculation of crossflow fluid and jet combustion products in the jet supported leeward flame stabilization.
- For $J$~5 flame stabilization was the result of both flame propagation and auto-ignition; for $J > 5$ auto-ignition was the dominant flame stabilization mechanism.

- Strain-rate correlated well with flame behavior; low strain rates delay auto-ignition, high strain rates exceeding ~6000$s^{-1}$ inhibit auto-ignition.

Additionally, characterization of both the non-reacting and reacting JICF flow fields was conducted in this chapter and the major findings are listed below.

- For non-reacting JICF, the velocity decay along the jet centerline was steady, and scaled well with free jet centerline velocity decay.
- For reacting JICF, there was a distinct location along the jet centerline at which high dilatation generated by heat release led to an increase in jet centerline velocity; as a result reacting jets penetrated further into the crossflow than non-reacting jets.
- Confinement effected jet penetration; as *J* increased, and jet penetration increased, differences between non-reacting and reacting jets were minimized.
- A new asymptotic correlation was developed to describe the trajectory behavior of both the non-reacting and reacting JICF.
- The wake structure of the reacting JICF changed relative to the non-reacting JICF wake; heat release present in the jet wake prohibited the formation of the upright wake vortices, and led to stronger flow recirculation.

# CHAPTER FOUR

# 4. Flame Stabilization for Lean-Rich JICF Conditions

### Introduction

In this section, the effect of $\phi_j$ on flame stabilization is examined in detail. In Chapter 3 it was shown that both auto-ignition and flame propagation assist in the stabilization of the $\phi$ = 1.2 JICF flame. Changing jet equivalence ratio affects the reactivity of the jet mixture, such that flame propagation and auto-ignition characteristics are changed. Flame visualizations from high chemiluminescence imaging and simultaneous $CH_2O$, OH PLIF, and PIV are presented for combustion analysis of the varying $\phi_j$ jets. Since the evolution of an ignition kernel, from initial formation up to the point in which it merges with the main flame structure, occurs over a very short duration of time, high speed chemiluminescence imaging was instrumental for observing such behavior. Similarly, high speed chemiluminescence assisted in imaging the time resolved motion associated with flame propagation. More detailed analysis on the JICF flame structure is presented subsequently using the simultaneous two-dimensional OH, $CH_2O$ PLIF and PIV measurements. The focus of the PLIF-PIV data analysis was to determine how the flame interacts with the highly complex JICF flowfield. Although it does not provide time sequence information, the coupled flame and flow field data provide further insights into the JICF flame anchoring not obtainable from high speed chemiluminescence imaging alone.

### 4.1 Chemiluminescence Imaging

The chemiluminescence images for the different $\phi_j$ conditions were conducted at 8.4 kHz, as described in Section 2.4.1. Previous studies [45], [46], [68] have reported that the JICF flame stabilization behavior along the windward and leeward jet boundary can be noticeably different. This

was also observed for the $\phi_j = 1.2$ condition presented in Chapter 3. The $\phi_j = 1.2$ windward flame stabilization was characterized by three distinct behaviors: (1) windward flame attachment, (2) unsteady lifted flame behavior, and (3) windward flame blowoff. On the other hand, leeward flame stabilization was characterized by more consistent behavior, in agreement with [45], [46]. In this section visualization of the JICF lean, stoichiometric, and rich flame chemiluminescence is presented.

From the high speed PIV measurements it was determined that windward flame stabilization for $J > 5.2$, $\phi_j = 1.2$ was controlled by auto-ignition. For $J = 5.2$, $\phi_j = 1.2$ flame edge propagation was found to also assist in the windward flame stabilization. For higher $J$ values, increased windward flame liftoff provided for more mixing between jet and crossflow ahead of the flame front. The mixing, and subsequent heat transfer from hot crossflow to jet reactants, led to auto-ignition upstream of the lifted flame edge. Figure 4.1 presents an example of windward auto-ignition following windward flame blowoff for $J = 8.7$, $\phi_j = 0.8$. Ignition kernel formation is shown in two different instances during the 2.5 ms time sequence. In the first instance, development of the ignition kernel begins in frame (c), as evidenced by the faint chemiluminescence signal centered in the circular outlined region. As the ignition kernel grows larger, and becomes more luminous, it also convects towards the downstream flame that is anchored by the leeward flame branch. When the kernel merges with the downstream flame structure in frames (g)-(h), the windward flame branch is established. While connected downstream with the leeward flame branch, the flame luminosity of the windward flame branch continues to increase. Formation of a second ignition kernel is seen in Fig. 4.1 frame (h), upstream of the newly established windward flame branch. Once again, the kernel grows in size, and becomes more luminous, as it convects away from the jet exit. The ignition kernel connects with the windward flame branch in frames (m)-(o), by means of a thin flame segment that extends outward from the windward flame branch.

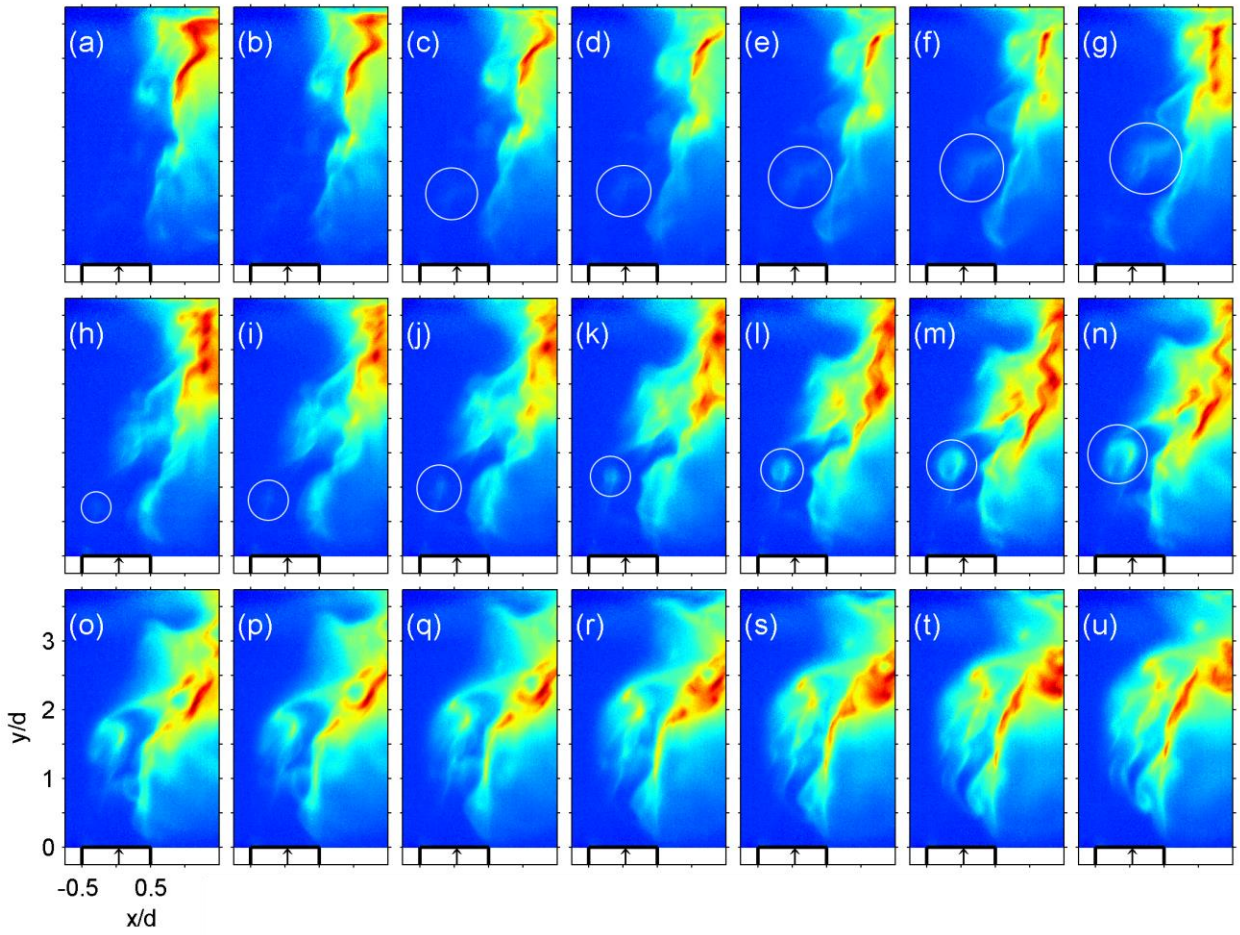


**Fig. 4.1: Sequence showing the recovery of windward flame stabilization following blowoff via ignition kernel formation for $J$ = 8.7, $\phi_j$ = 0.8. Chemiluminescence images have been normalized by max intensity and recreated in false color where red represents highest flame luminosity.**

The structure of the ignition kernels shown in frames (c)-(g) and (h)-(n) were noticeably different. The second ignition kernel observed in frames (h)-(n), appeared as a coherent structure with strong chemiluminescence, while the first ignition kernel, frames (c)-(g), was characterized by more distributed and relatively weaker chemiluminescence. The coherent ignition kernel highly resembles the structures visualized in the non-reacting JICF shear layer in [6]. The increasing size of the ignition kernel corresponds well with the growth of the jet shear layer vortices as they convect downstream. Increased mixing time between jet and crossflow in the vortex core would provide suitable conditions

for auto-ignition. Further analysis will be presented on flame-vortex interaction in later sections of this paper. The more distributed ignition kernel, frames (c)-(g) is most likely the result of ignition of a segment of the jet and crossflow mixing layer, as opposed to a distinct vortex structure.

The line-of-sight chemiluminescence images allow for increased visualization of three-dimensional effects, which occasionally showed interaction between the leeward and windward flame branches. Figure 4.2 presents a sequence of chemiluminescence image frames where the windward flame branch was reestablished after blowoff, assisted by propagation of the leeward flame. In Fig. 4.2 (a) there is no apparent windward flame branch, but a predominant flame segment along the leeward jet edge. Beginning in frame (b) a small flame segment, originating from the leeward flame branch, begins to propagate upstream, toward the windward jet edge. The propagation of the flame in this direction indicates burning around the edge of the circular jet. In frames (b)-(g) the propagating flame front moves almost all the way around the jet to the windward boundary. Assisted by the leeward flame it leads to windward flame stabilization in frame (h), after which the strength of the windward flame branch increases significantly and two distinct branches are observed (n). Similar leeward-windward flame interaction is seen in Fig. 4.1(r)-(u). Consideration for out-of-plane flame behavior will become increasingly important for interpretation of the 2-D PLIF-PIV results presented later in this chapter.

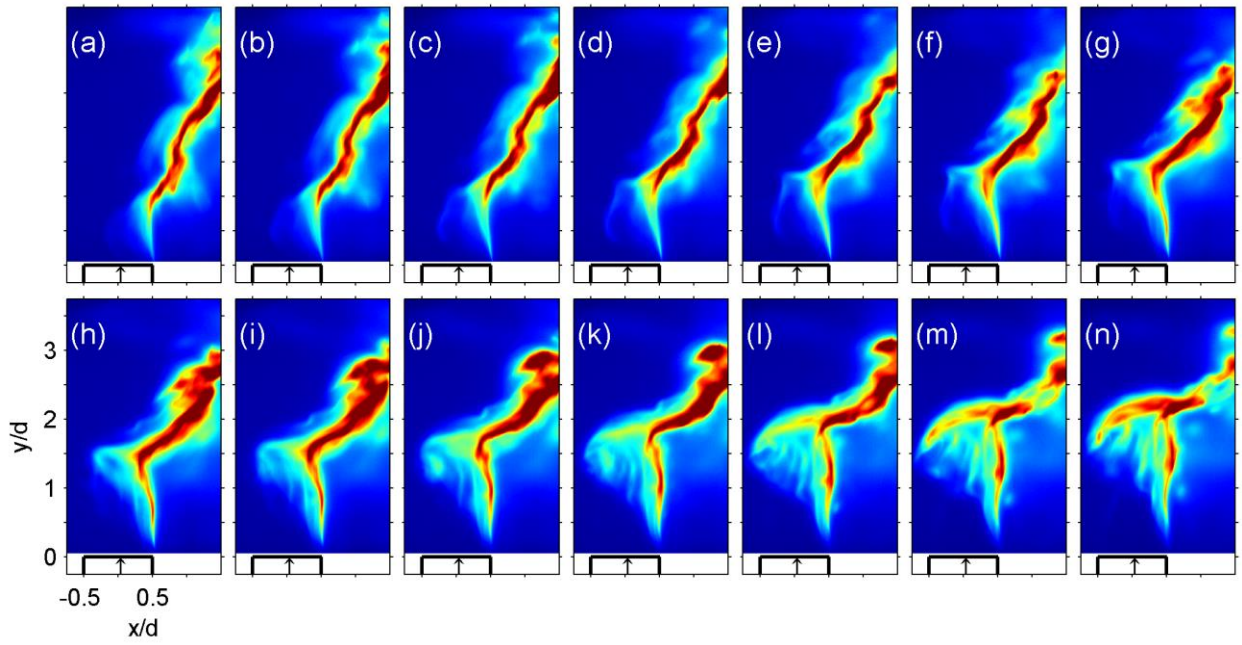


**Fig. 4.2: Sequence showing the recovery of windward flame stabilization following blowoff via leeward flame propagation for a $J$ = 8.7, $\phi_j$ = 1.2 JICF.**

Reestablishment of the windward flame following blowoff was seen to occur as a result of ignition kernel formation and ignition assisted by the leeward flame edge. Stabilization of the windward flame branch was maintained, until the next blowoff event, as a result of ignition kernel formation (Fig. 4.1) and windward flame propagation. An example of windward flame propagation is shown in Fig. 4.3. In the seven frames shown in Fig. 4.3 the windward flame moves steadily toward the jet exit from an initial location of $y/d$~1 to $y/d$~0.5. Windward flame stabilization via flame propagation becomes possible when the propagation speed of the leading windward flame edge achieves dynamic balance with the local flow velocity. In Fig. 4.3, the flame propagation speed exceeded the local flow velocity upstream of the flame, such that the flame was able to propagate towards the jet exit. The absence of ignition kernels ahead of the lifted flame front further confirms that premixed flame propagation was responsible for the stabilization of windward flame front in this instance. Flame stabilization via flame propagation is also the primary factor that leads to windward flame blowoff. Increases in local velocity

upstream of the flame edge, as a result of jet velocity fluctuations, disrupt the balance between the flame propagation speed and flow speed causing the leading flame edge to move further downstream (blowoff).

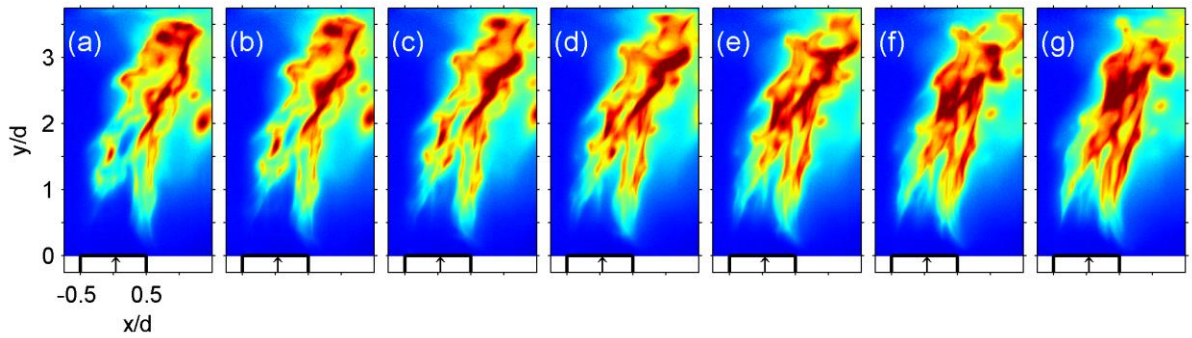


**Fig. 4.3: Sequence showing windward flame propagation for a $J$ = 8.7, $\phi_j$ = 1.0 JICF.**

The time resolved chemiluminescence data was most useful for visualizing the dynamic behavior of the JICF flame including: blowoff, ignition kernel formation, and flame propagation. The focus of the next sections, where the PLIF-PIV results are presented, will be to understand the influences of varying $J$ and $\phi_j$ on flame stabilization. Thus far it is understood that windward flame stabilization favors velocity conditions that allow for flame propagation or mixing conditions resulting in continuous ignition kernel formation. In the experiment $J$ was varied by changing jet velocity and therefore it influences both the propagation and ignition behavior of the jet. Increasing $J$ results in higher velocities in the jet nearfield, which is less favorable for upstream flame propagation, but faster mixing between jet and crossflow, which is more favorable for auto-ignition conditions due to faster mixing with the hot crossflow. Similarly changing $\phi_j$ will influence both the propagation and ignition characteristics of the jet mixture.

### 4.2 OH and $CH_2O$ PLIF

An example of the typical JICF flame structure observed through $CH_2O$ and OH PLIF imaging is shown in Fig. 4.4. The windward and leeward PLIF images were not taken simultaneously and thus the two images represent different instances in time. The post-processed PLIF images show that flame structure consists of three distinct regions: a preheat zone ($CH_2O$ only), a reaction zone ($CH_2O$ and OH overlap), and a post-flame zone (OH only). The preheat zone resides closest to the premixed reactants, while the post-flame region resides closest to the crossflow stream. There was no measurable level of OH in the crossflow and as such the OH images show the regions of combusting jet mixture and its products region. The thin region of overlap of OH and $CH_2O$, as determined by the pixel-by-pixel product of the two PLIF signals, determined the location of the heat release zone. The focus of this section is for characterization of the different PLIF behaviors observed for the JICF flame; observations on flame and flow field interaction will be the focus of the next section.

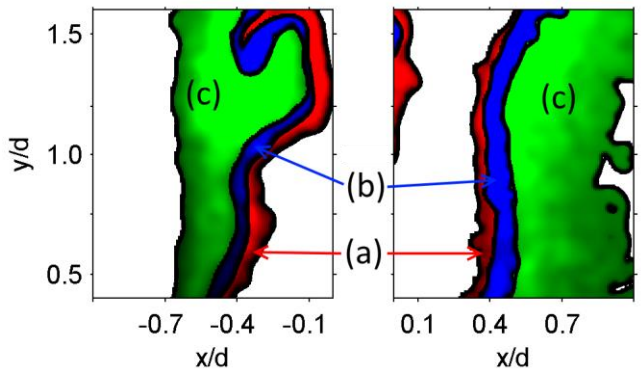


**Fig. 4.4: Example of JICF flame structure observed through OH and $CH_2O$ PLIF imaging for both the windward (right) and leeward (left) ROI. $CH_2O$ is presented in red, OH in green, and OH*$CH_2O$ in blue. Labeled regions correspond to (a) preheat zone, (b) heat release zone, and (c) post-flame zone.**

### *4.2.1 Windward Flame Behavior*

Figure 4.5 shows instantaneous examples of the three most common windward flame behaviors that were observed independent of $J$ and $\phi_j$. The first example shown in Fig. 4.5(a), shows both $CH_2O$, OH, and heat release contours that stretch across the entire *y/d* range in the images. This behavior will be referred to as an attached flame. The second behavior observed is shown in Fig. 4.5(b), and is referred to as a lifted flame, where the $CH_2O$, OH, and subsequent heat release contours are lifted above the jet exit. In Fig. 4.5(c) the third flame shows lifted OH and heat release contours, however there is an extended region of $CH_2O$ upstream of the heat release region. For the example shown in Fig. 4.5(c), the $CH_2O$ formation upstream of the lifted OH/heat release zone extends significantly farther upstream from the heat release zone than for the lifted flame condition shown in Fig. 4.5(b). For this reason, flames exhibiting this behavior will be referred to simply as flames with extended $CH_2O$ formation.

Flames with extended $CH_2O$ formation are a new observation for the premixed JICF configuration; however, similar observations have been made in different experiments where auto-ignition is prevalent [22], [30]. Gordon et al. [22] observed regions of "$CH_2O$ only" upstream of a lifted flame base in a lifted jet in vitiated coflow configuration. Premixing between the central fuel jet and high temperature vitiated coflow upstream of the stabilized flame lead to the formation of the "$CH_2O$ only" regions. The absence of OH in these regions indicated pre-ignition behavior [21], without full thermal runaway. The authors in [22] did also observe auto-ignition kernel formation, which was characterized by isolated regions of overlapping $CH_2O$ and OH ahead of the stabilized flame front. The $CH_2O$ signal in the windward part of JICF was rarely observed as an isolated pocket upstream of the flame; instead, the $CH_2O$ signal most often remained continuous, either attached or lifted.

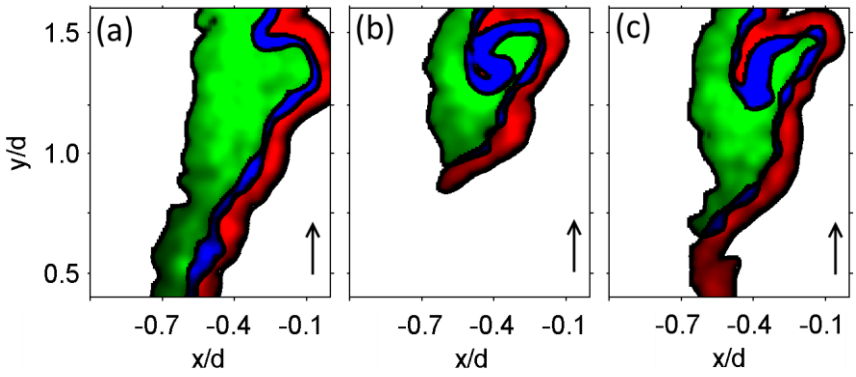


**Fig. 4.5: Examples of instantaneous JICF windward OH PLIF-$CH_2O$ PLIF behavior: (a) attached flame, (b) lifted flame, and (c) extended $CH_2O$ formation. $CH_2O$ is presented in red, OH in green, and OH*$CH_2O$ in blue.**

In the high speed chemiluminescence sequence shown in Fig. 4.1 isolated ignition kernel formation upstream of the windward flame edge was observed. Initially, formation of these kernels was thought to be the result of crossflow entrainment by the jet shear layer vortices. Heat transfer from the hot crossflow to jet reactants, along with long residence times in the vortices would provide for auto-ignition. In the PLIF images, isolated ignition kernels were rarely observed; instead, thickened flame structures, as shown in Fig. 4.6, appeared where $CH_2O$ contours aligned with a vortex structure. The boxed-in regions shown in Fig. 4.6 correspond to the locations where there was localized thickening of the heat release region, seen via PLIF imaging. Unlike the kernels observed with high-speed chemiluminescence imaging, the thickened structures shown in Fig. 4.6 were not isolated in the flow field, as thin flame branches extended from the kernel. The windward PLIF region was chosen based on the high-speed chemiluminescence data and the average location of the windward flame base; thus, it was intended to image the ignition kernels. However, because of the observation of these thin flame branches via PLIF and not high speed chemiluminescence further investigation of this behavior was required.

Additional analysis of the chemiluminescence ignition showed occasional occurrence of thin flame branches connecting to localized thickened flame regions, three different examples are shown in Figure 4.7. In sequence (a), a lifted windward flame is observed at $t_1$. At $t_2$ very weak chemiluminescence can be seen ahead of the lifted flame front and as time progress from $t_2$ to $t_4$, the intensity of chemiluminescence ahead of the lifted flame increases. The interesting feature about the ignition in sequence (a), is that the ignition structure appears connected to the lifted flame front, and resembles a thin flame branch more so than an ignition kernel. By $t_5$ the leading edge of the ignition structure beings to distort as it wraps around a vortex element, similar to the behavior observed in the PLIF images. In sequences (b) and (c), distinct ignition kernel formation is seen upstream of the lifted windward flame branch; however, the progression of the ignition suggests the existence of flame branches connecting the ignition kernel and lifted flame front. In Fig. 4.1, the isolated kernels moved away from the jet until they eventually merged with the lifted leeward stabilized flame branch. In sequences (b) and (c) in Fig. 4.7, there appears to be a thin faint region that connects the bright kernel and stabilized flame branch. Im et al [26] observed similar continuous ignition structures in a turbulent mixing layer, in cases where turbulence was weaker. Increasing the turbulence in the mixing layer led to break up of the continuous ignition layer and the formation of distinct ignition kernels.

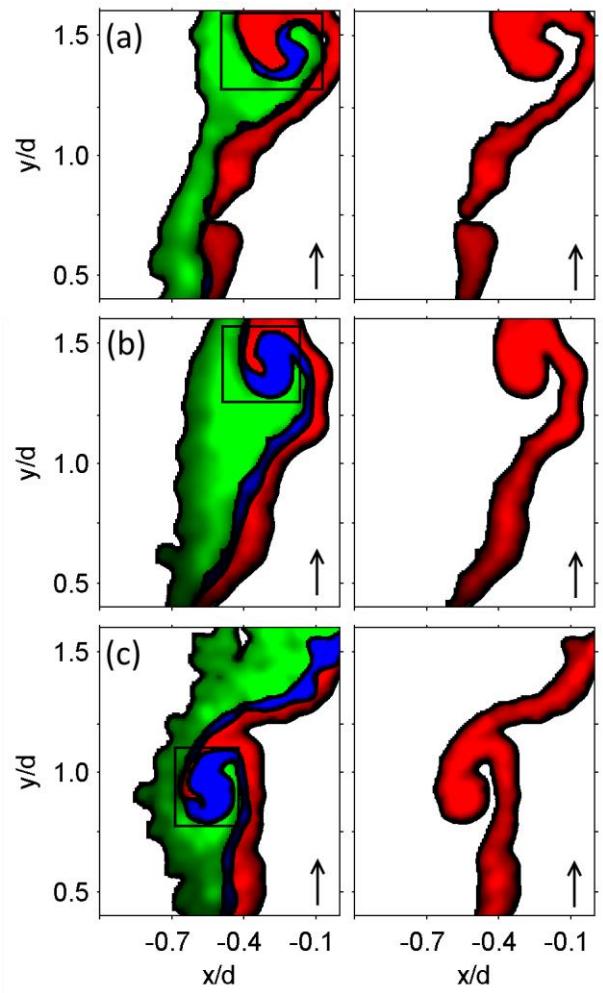


**Fig. 4.6: Examples of $J$ = 8.7 instantaneous windward JICF ignition kernel formation seen via OH PLIF-$CH_2O$ PLIF. Figures on left: $CH_2O$ (red), OH (green), and OH*$CH_2O$ (blue). Figures on right: $CH_2O$. The corresponding $\phi_j$ for (a)-(c) were 0.8, 1.2, and 1.0, respectively.**

Consideration of the flame observations from both chemiluminescence and PLIF data has led to a new conclusion regarding the localized ignition kernels. The thin flame branches ignite along the jet and crossflow mixing layer where heat transfer from crossflow to jet is highest. This behavior is evidenced by occasional buildup of $CH_2O$ ahead of the lifted flame edge. Because these thin flame branches ignite along the mixing layer, flame interaction with the windward shear layer vortices is common. The flame vortex interactions can result in two different behaviors: thickening of the heat

release zone and buildup of $CH_2O$ radical pools. Thickening of the heat release zone can occur as a result of flame folding /merging caused by the strong vortex motion. Buildup of $CH_2O$ in the vortex elements can be the result of more focused heat transfer from the folded flame to the reactants in the vortex core [64], or preheating of jet reactants caused by mixing with crossflow fluid. The jet shear layers are the primary mechanism responsible for crossflow entrainment in the jet nearfield and the long mixing residence times in the vortex cores could to the preheating of jet reactants and formation of $CH_2O$. Differences between the isolated ignition structures observed in Fig. 4.1 and the flame branch segments observed in Fig. 4.6 will be addressed in *Section 4.3.1*. It will be shown that flame stabilization along the mixing layer leads to increased strain along the flame surface, most significantly along the thin flame branches. Additionally, flame stabilization closer to the crossflow suggests ignition of mixtures containing both jet reactants and crossflow fluid. Both increased strain and reactant dilution can affect the strength of the chemiluminescence signal, such that more localized kernels appear in the chemiluminescence imaging.

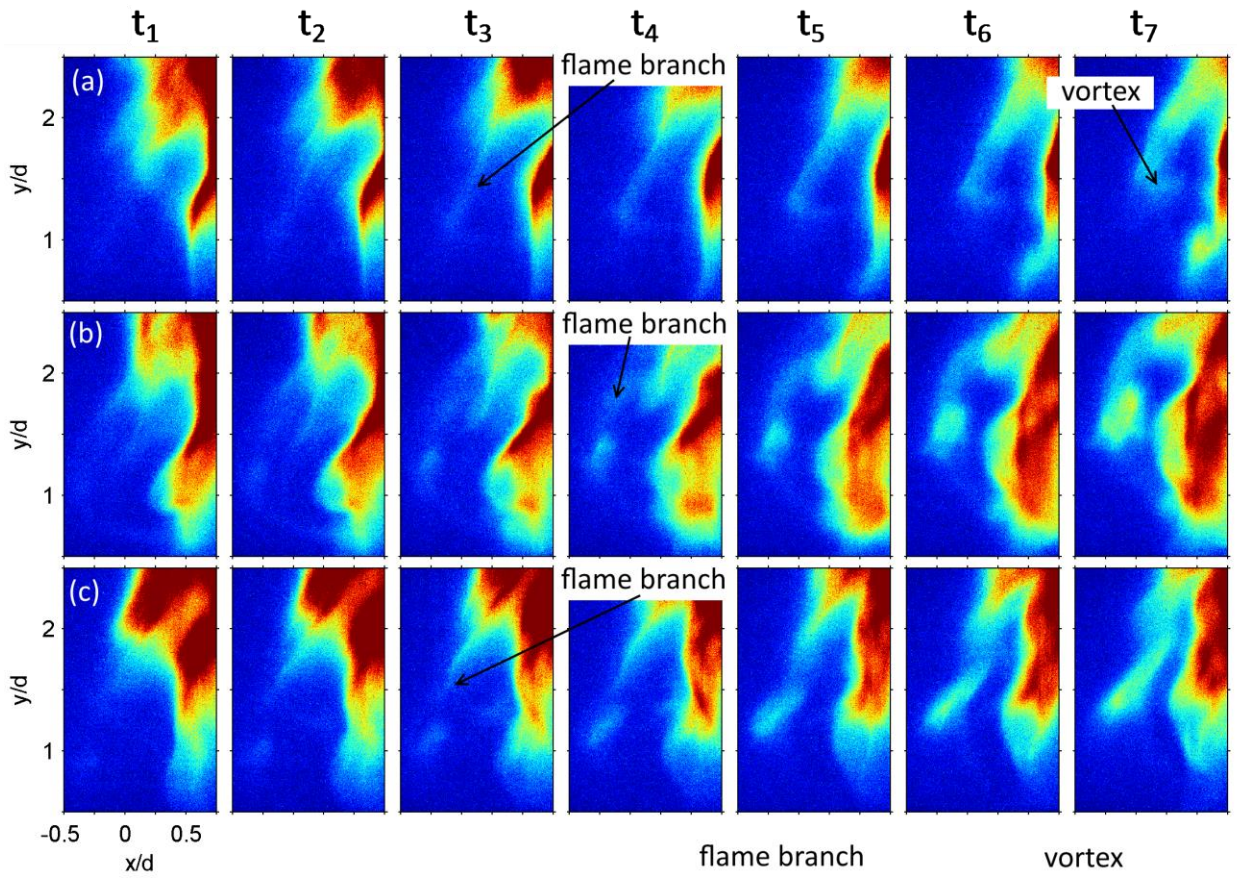


**Fig. 4.7: Examples of $J$ = 8.7, $\phi_j$ = 0.8 instantaneous windward JICF ignition formation seen via high speed chemiluminescence imaging. Time between frames is 0.12 ms.**

### *4.2.2 Leeward Flame Behavior*

The JICF flame structure in the leeward region of interest was more consistent than the windward flame behavior. The leeward flame PLIF image shown in Fig. 4.4 is representative of the typical behavior observed, again, independent of $J$ and $\phi_j$. In the leeward region, the flame remained attached and no large vortical structures were observed along the leeward flame branch. No localized thickening of the preheat and/or heat release zones was observed, which is agreement with the lack of ignition kernels seen in the leeward jet region from the high-speed chemiluminescence data.

## 4.3 Simultaneous OH, $CH_2O$ PLIF and PIV

The high speed chemiluminescence imaging allowed for visualization of the time resolved features of the JICF flame. From these measurements it was concluded that stabilization of the highly unsteady windward flame occurred as a result of ignition kernel formation and flame propagation. Formation of the windward flame ignition kernels was dependent on the buildup of $CH_2O$ radicals along the jet shear layer, as seen from the $CH_2O$ and OH PLIF results presented in Section 4.2. In this section results are presented from simultaneous $CH_2O$, OH PLIF, and PIV measurements. Though not time resolved, the simultaneous PLIF-PIV measurements provided detailed information on the flame-flowfield interaction, with particular focus on understanding the JICF flame stabilization. Key results presented in this section include flame-vortex interactions, flame-shear layer behavior, and flame stretch analyses. The effect of $J$ and $\phi_j$ on flame behavior is also examined in this section.

### *4.3.1 Flame-Vortex Interactions*

The flame-vortex interactions were most prevalent in the windward side where the JICF shear layer vortices are most prominent. The effect of the vortices on flame structure varied. In some instances, the heat release zone resided on a vortex. This behavior led to thickening of the reaction zone as a result of flame folding and possible merging between ignition structures and thin flame branches. The flame-vortex interactions for the instantaneous flame examples shown in Fig. 4.6 are depicted in Fig. 4.8 by combining the heat release information with the vorticity field. In the images shown, the thickening of the flame surface is clearly seen where a vortex structure is in close proximity to the flame. The flame was also observed to wrap around the outer boundary of a vortex element and thus, only thickening of the preheat zone was observed. An example of this behavior is shown in Fig. 4.8(d). Two vortices are apparent in this instantaneous image, both of which reside on the outer edge of the preheat zone closest to the reactants. A thickened region of $CH_2O$ upstream of the lifted heat release

zone is present in the vicinity of the first vortex structure ($y/d$~0.5). No flame is present near this vortex, suggesting a region of mixing between hot crossflow and reactants in the vicinity of this. The flame surface near the second vortex ($y/d$~1) is clearly distorted as a result of its presence. The preheat zone near this flame surface is thickened, but no thickening of the flame surface is observed. Without time resolved imaging it is not possible to determine if this behavior is simply an early stage of flame-vortex interaction, before flame thickening occurs, or if it is an example of an entirely different flame-vortex interaction, where only the preheat zone is affected.

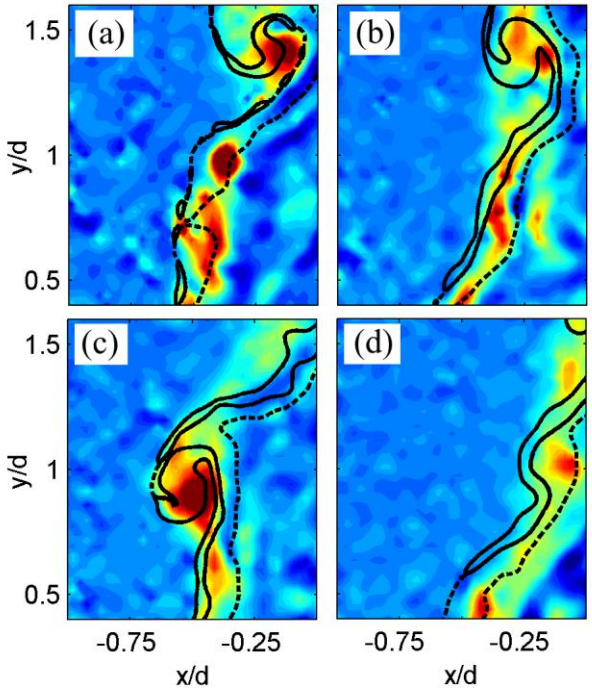


**Fig. 4.8: Instantaneous heat release (solid lines) and preheat zone (dashed lines) overlaid onto $\omega_z$ field. Minimum (blue) and maximum (red) $\omega_z$ in the images shown are -3000 and 12000 $s^{-1}$, respectively. The three cases (a), (b), and (c) correspond to the same cases shown in Fig. 4.6. Case (d) shows vortex-preheat zone interact for a $J$ = 8.7, $\phi_j$ = 1.2.**

The effect of flame-vortex interactions on the flame strain, $\kappa_a$ is shown in Fig. 4.9. The two cases shown correspond to the boxed in flame-vortex interactions shown in Fig. 4.6 (a) and (b). The flame surfaces shown in Fig. 4.9 are divided into three regions: (i) leading flame branch, (ii) folded

flame surface, and (iii) trailing flame branch. Region (i) corresponds to the thin flame branch that extends from the vortex toward the jet exit and region (iii) corresponds to the thin flame branch that extends from the vortex away from the jet exit. The folded flame region (ii) corresponds to where thickening of the flame is significant. The plots of $\kappa_a$ along the flame surfaces confirm that along the thickened flame surface $\kappa_a$ is low and along the flame branches $\kappa_a$ is highest. In both cases (a) and (b), $\kappa_a$ exhibits two localized peaks, on either side of a region where $\kappa_a$ is less than half the peak magnitude. The two peaks correspond to the highly strained flame edges (i) and (iii) in the braids of the vortex and the thickened flame (ii) surface is the low strain region in the vortex core between the two peaks. Increased strain rate has been shown to significantly affect CH concentration, which is the primary species responsible for both OH* and CH* [75]. Thus, it is possible that more distinct ignition kernels were observed in the CH* chemiluminescence imaging (as seen in Fig. 4.1) because CH* chemiluminescence of the thin flame branches was very weak relative to those of the thickened flame regions.

Curvature plots are also shown in Fig. 4.9. In each case the thickened flame fronts exhibit both positive and negative curvature. The peak positive curvature is around approximately ~1mm$^{-1}$, and results from the flame surface being pulled inward by the vortex. A consequence of the flame surface being pulled in by the vortex is the formation of a cusp region with strong negative curvature, beyond the curvature resolution range. These curvature plots show that no single curvature convention (positive or negative) can be associated with the thickened flame segments. It has been shown here however, that flame-vortex interactions cannot be characterized simply by high $\kappa_a$ or high $C$ because there are significant variations in both $\kappa_a$ and $C$ along the flame surface. As previously mentioned, the formation of coherent vortex rollups occurs predominately along the JICF; and therefore, no isolated flame-vortex interactions were observed along the leeward flame branch.

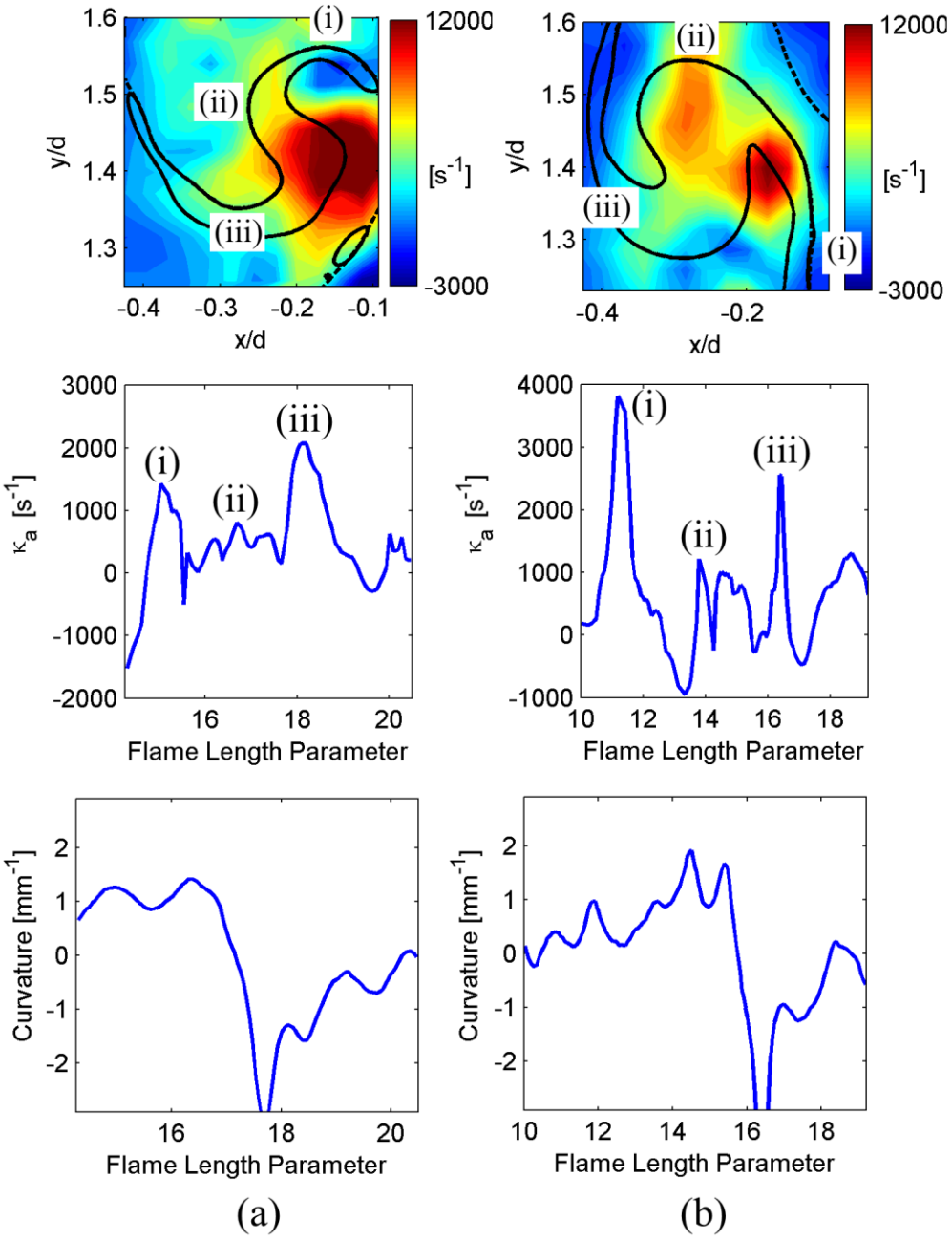


**Fig. 4.9: Flame strain $\kappa_a$ and Curvature *C* for two instantaneous flame-vortex interactions. The cases shown are (a) and (b) from Fig. 4.6 and 4.8.**

### *4.3.2 Visualization of Flame-Shear Layer Interaction*

The PLIF-PIV measurements showed a higher extent of flame-shear layer interaction than previously realized from the 2-D dilatation measurements computed from high speed PIV measurements. The PLIF-PIV results show that near the flame anchoring location, for both the windward and leeward flame branches, the flame is highly intertwined in the shear layer. It is in the shear layer where the vortex-flame interactions are observed and where the most significant amount of nearfield mixing between jet and crossflow occurs. In Fig. 4.10 instantaneous examples of flame-shear layer interactions are shown for both the leeward and windward flame branches. For visualization of the shear layer the z-component vorticity $\omega_z$ was used. In both the crossflow and jet, the vorticity is small as compared to the shear layer where vorticity is significantly higher and concentrated. The leeward flame branch consistently anchored in the shear layer for all $\phi_j$; however, at points along the flame farther from the flame base the flame moved away from the shear layer toward the bulk jet reactants as shown in Fig. 4.10.

Windward flame behavior appeared to be more significantly affected by $\phi_j$. For the lean jet mixture the windward flame branch was most frequently observed to remain situated on the shear layer. On the other hand, for the stoichiometric and rich jet mixtures the windward flame branch exhibited similar behavior to the leeward flame branch, in which the flame anchored in the shear layer but moved toward into the bulk jet flow with increasing distance from the flame base. Examples of the windward flame behavior are shown in Fig. 4.10(a) and for both jet equivalence ratio conditions the flames clearly anchor in the shear layer. For the windward flame specifically, the flame appeared to anchor in the shear layer closer to the crossflow. Auto-ignition calculations that simulate ignition between cold reactants and hot, vitiated crossflow have shown that auto-ignition favors highly diluted reactant mixtures where reactant concentration is low, but temperature is high [21], [35], [45]. Flame base

stabilization closer to the crossflow suggests auto-ignition behavior, as local mixtures in this region would be expected to contain higher concentration of crossflow and thus, shorter ignition delay times. Ignition of these highly diluted mixtures could also have an effect on the CH* production, as the concentration of reactant fuel is significantly decreased with increased dilution.

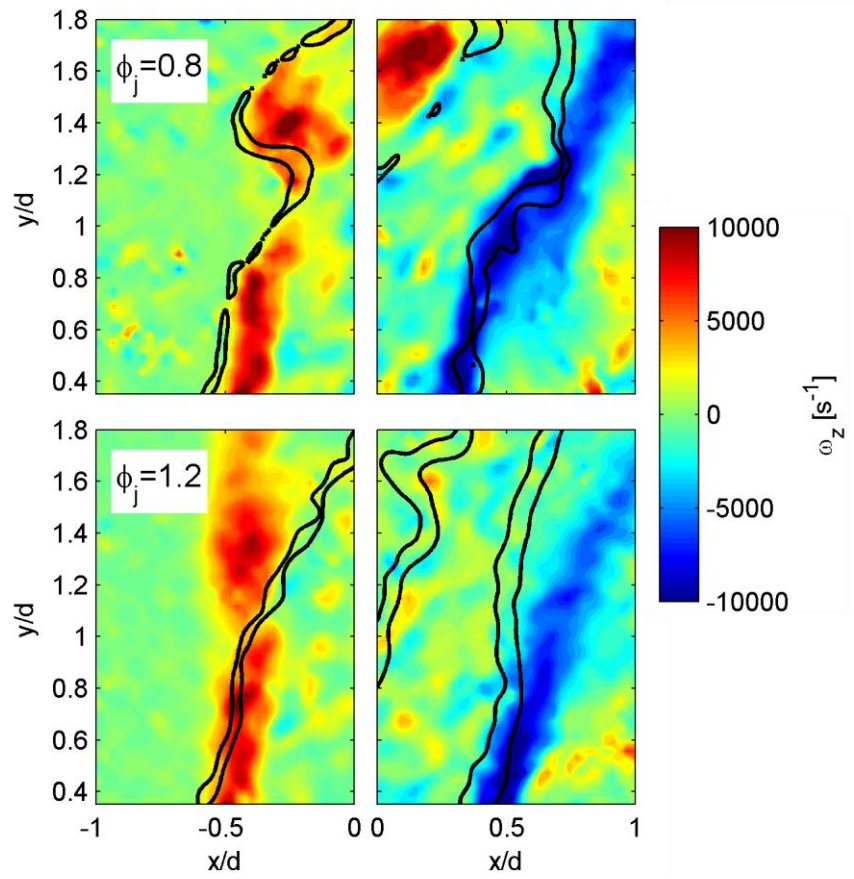


**Fig. 4.10: Instantaneous heat release contours overlaid onto $\omega_z$ for *J* = 8.7: windward region (left) and leeward region (right).**

As previously mentioned, the 2-D dilatation measurements presented did not show the same extent of flame-shear layer interaction as seen from the PLIF-PIV measurements. Figure 4.11 shows the same instantaneous heat release contours pictured in Fig. 4.10, but overlaid onto the 2-D dilatation field. In these images, agreement between heat release location ($CH_2O$, OH overlap) and 2-D dilatation varies.

The agreement between heat release location and 2-D dilatation is strongest when the flame resides away from the shear layer. On the other hand, when the flame is situated on the high vorticity shear layer the 2-D dilatation does not accurately reflect the heat release behavior. These results confirm the observations seen in previously for the $\phi_j$=1.2 JICF where the flame identified using 2-D dilatation was always seen to reside just outside of the shear layer.

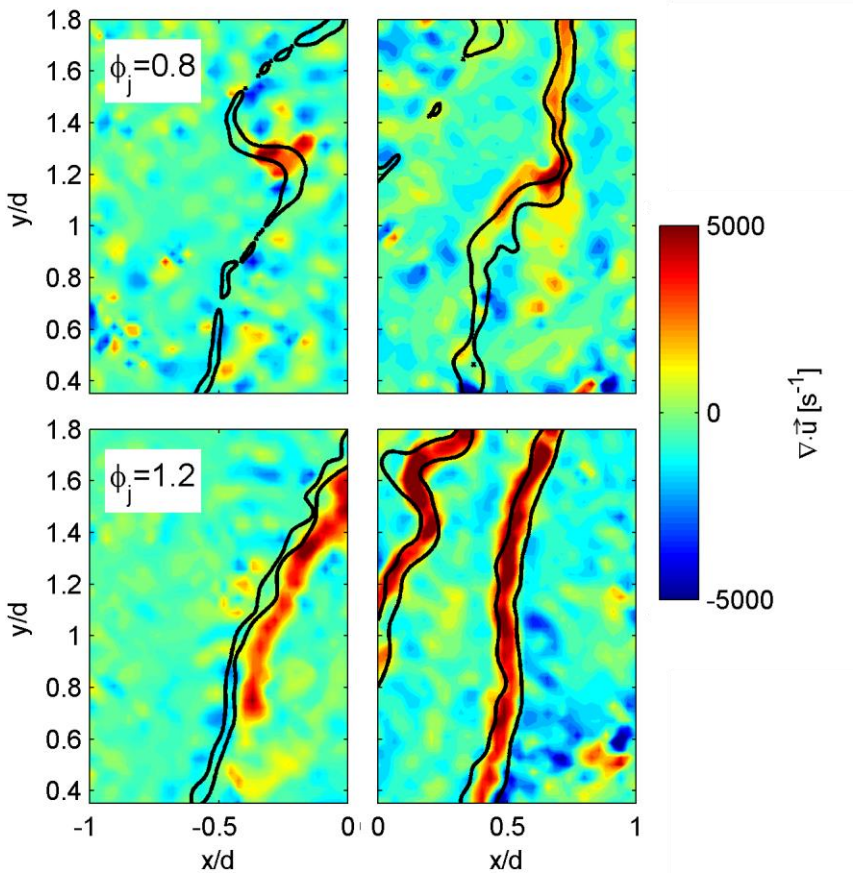


**Fig. 4.11: Instantaneous windward (left) and leeward (right) heat release contours overlaid onto 2-D dilatation field for *J* = 8.7 JICF: $\phi_j$ = 0.8 (left) and $\phi_j$ = 1.2 (right). Cases are the same as those shown in Fig. 4.10.**

It has been shown in previous studies [61], [62] that for premixed flames, dilatation is a reasonably good marker for heat release; and thus it requires further evaluation to determine the cause of disparity between the heat release and dilatation in the JICF configuration. One such factor is the likely

effects of out-of-plane motion. For the experimental PLIF-PIV results, only 2-D measurements were acquired, and consequently only 2-D dilatation was computed. The JICF flow field is highly complex, with a high degree of three dimensionality. For example, the jet shear layer rollups that form along the windward JICF shear layer are most noticeably along the jet centerline, however advection by the crossflow causes these vortex structures to wrap around the jet column. The stretching of the vortex filaments around the jet creates significant out-of-plane motion, where the reference plane is the jet centerline plane parallel with the crossflow flow direction. As a result, in a non-reacting JICF configuration, 2-D dilatation along the windward shear layer would be expected to be negative. In the case of reacting JICF when the windward flame stabilizes in shear layer, negative 2-D dilatation caused by the out-of-plane motion counteracts the positive dilatation caused by heat release. As the flame moves away from the shear layer and into the bulk jet flow the out-of-plane motion is minimal, and thus the 2-D dilatation accurately reflects the heat release behavior.

### *4.3.3 Statistical Analysis of Flame-Shear Layer Interactions*

In Fig. 4.12, plots of average $\omega_z$ and dilatation along the flame edge at different *y/d* positions are shown. The 2-D dilatation along the windward and leeward flame branches is noticeably different, with much higher dilatation along the leeward flame branch. These statistics are in agreement with the results shown in Fig. 4.11; that there was more consistent agreement between heat release and dilatation along the leeward flame branch. Along the leeward flame branch dilatation was always positive, and increased with increasing *y/d*. Increased leeward flame-shear layer interaction with increasing *J*, as evidenced by higher nearfield vorticity, resulted in lower dilatation. For the stoichiometric and rich flame conditions the average dilatation converged along *y/d*, which is in agreement with the laminar flame calculations shown in Table 2.3 (approximately 6% difference in maximum dilatation). The results shown in Fig. 4.12, confirm that for $\phi_j \geq 1$ the leeward flame completely uncoupled from the

shear layer, as dilatation became independent of *y/d* location. Similarly, from the laminar flame properties it is expected that the dilatation for the lean flame is less, as there is a reduction of approximately 44% in maximum dilatation relative to the laminar rich jet condition.

In the leeward region, the vorticity along the flame edge decreased consistently with increasing *y/d* location; vorticity trends along the windward flame edge were non-monotonic. Slight increases in vorticity were observed along the windward flame branch with increasing *y/d*, consistent with the observation that the flame traveled from the crossflow side to the jet side of the shear layer. Following an increase in vorticity, a peak was reached (center of the shear layer) after which vorticity decreased. For the rich flames, the flame crossed the shear layer earlier, as evidenced by the *y/d* location of the peak average vorticity and subsequent rapid decrease in vorticity. Increase in vorticity with *J* was also observed, as a result of stronger shear generated by the higher jet momentum. Average dilatation along the leeward flame branch was consistently higher than the dilatation along the windward flame edge. The windward dilatation in regions of highest flame-shear layer interactions was independent of $\phi_j$ suggesting that out-of-plane motion affects dilatation in the windward branch.

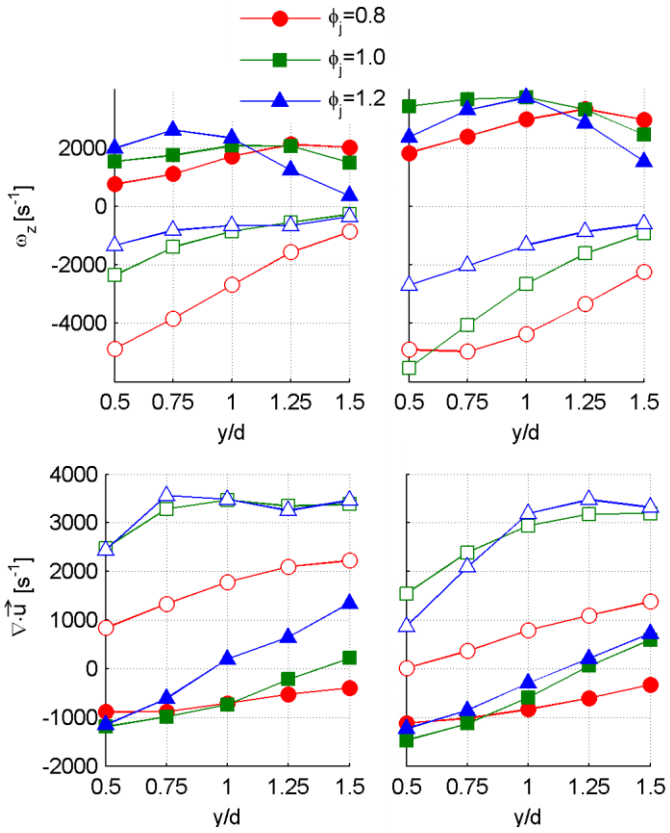


**Fig. 4.12: Average vorticity and dilatation for *J* = 5.2 (right) and *J* = 8.7 (left) JICF: windward region (closed symbols) and leeward region (open symbols).**

Emphasis has been placed on characterizing the flame-shear layer interaction for better understanding the flame stabilization behavior. For premixed bluff-body stabilized flames it has been shown that as equivalence ratio approaches the lean flame stability limit, the flame interacts significantly more with the shear layer [19], [20], [70]. A consequence of the increased flame-shear layer interaction is an increase in flame strain $\kappa_a$ along the flame edge, which can lead to local flame extinction events that ultimately cause flame blowoff. For the bluff-body flames, decreasing flame speed and heat release (with decreasing equivalence ratio) were considered to be the primary factors that leads to increased flame-shear layer interactions. The flame behavior in the JICF configuration can be thought of in a similar way to the bluff-body stabilized flame. The stoichiometric and rich JICF, which have highest laminar flame speed, produce the conditions in which the flame was observed to move farthest from the

shear layer in both the windward and leeward regions. The lean jet however, which has a lower laminar flame speed, was observed to remain much more coupled with the shear layer, most notably in the windward region.

Another notable observation about the flame-shear layer interaction in the premixed JICF configuration is how it compares to the behavior found in non-premixed JICF configurations. In the experiment presented by Lyra et al. [68], a jet containing 70% $H_2$/30% He by volume was injected into a 1200K fuel-lean vitiated crossflow and the flame behavior was analyzed using simultaneous PIV and OH PLIF imaging. For the $J$=9 non-premixed JICF system, the flame remained anchored uniformly around the jet exit. In the jet nearfield the windward and leeward flame branches stabilized along the outer edge of the shear layer (closer to the crossflow). In the jet far field, the flame moved farther from the shear layer, toward the crossflow, such that the flame remained outside of the characteristic jet shear layer rollup. For this non-premixed JICF configuration, jet and crossflow mixing is critical for flame stabilization and so it is possible that the flame remains outside the shear layer closer toward the oxidizer, where the fuel and oxidizer have mixed in stoichiometric proportions.

The premixed JICF flame is an interesting contrast to non-premixed flame results [68], as the premixed flame can traverse the shear layer into the bulk jet flow, most markedly for $\phi_j \geq 1$, such that flame stabilization appears independent of crossflow mixing. Because the premixed jet contains a flammable mixture, flame stabilization in the bulk jet flow (away from the shear layer) implies premixed flame propagation behavior. Thus, the JICF flame stabilization has been divided into two regimes, as pictured in Fig. 4.13: (1) flame-shear layer interaction and (2) flame stabilization in the bulk jet flow. For the windward flame, flame stabilization in the shear-layer suggests both auto-ignition and flame stabilization are likely contributing mechanisms. From the results presented in in Chapter 3 it was shown that in this regime auto-ignition is more dominant than flame propagation for higher $J$ values, but

at lower *J* auto-ignition and flame speed can both contribute to flame stabilization. The leeward flame also anchors in the shear layer; however the leeward flame behavior is more consistent. Flow recirculation of hot crossflow and combustion products in the jet wake has been suggested to be the primary factor in assisting leeward flame stabilization. For both the windward and leeward flame segments that stabilize away from the shear layer in the bulk jet flow, premixed flame propagation is likely the dominant flame stabilization mechanism. In the bulk jet flow, lack of jet-crossflow mixing implies that the reactants being consumed are purely from the premixed jet mixture and flame propagation is dominant.

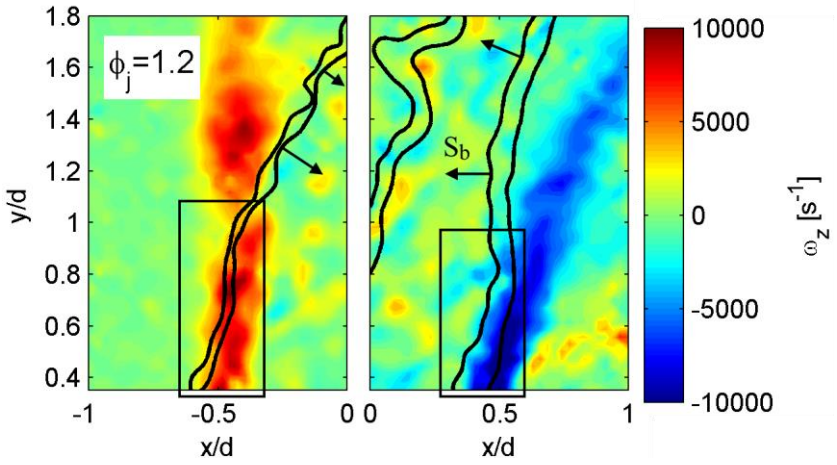


**Fig. 4.13: Instantaneous example different regimes of flame stabilization for the windward and leeward JICF flame. Boxed-in regions correspond to flame-shear layer interactions; arrows indicate premixed flame propagation behavior. Case shown is for the *J* = 8.7, $\phi_j$ = 1.2 JICF.**

### 4.4 Flame Stretch Analysis

In *Section 3.3* the importance of flame-shear layer interactions for flame anchoring was shown, as heat transfer from hot crossflow to jet reactants in the shear layer allowed for auto-ignition. In this section, results are presented from calculations of flame strain, $\kappa_a$ and flame curvature, *C*. The importance of these results is to determine the effect of shear-layer interactions on the flame stretch. In [19], [20], [70] it was shown that increased flame-shear layer interactions increased the probability of

higher flame stretch, which was thought to cause localized extinction along the flame edge. Though no localized extinction was observed for the JICF flame, analysis of flame stretch is important for determining how flame stretch behavior may change for even leaner $\phi_j$ or higher *J* values.

### *4.4.1 Flame Strain, $\kappa_a$*

Further characterization of the JICF flame has been conducted by examining the behavior of flame strain, $\kappa_a$ along the flame edge at varying *y/d* locations is shown in Fig. 4.14. In general, variation in $\kappa_a$ along the flame front was most significant along the windward flame edge. In this region, $\kappa_a$ increased with increasing *y/d* location. As shown, in the bottom panel of Fig. 4.14, the increase in $\kappa_a$ with increasing *y/d* location was the result of increasing dilatation ($S_{xx}$ and $S_{yy}$) and decreasing shear strain $E_{xy}$. It was shown that windward dilatation did not vary significantly with *J*, thus the increased $\kappa_a$ along the windward flame front at the higher *J* was the result of increased $S_{xy}$ with the higher jet momentum. The trend in $\kappa_a$ was similar for the $\phi_j$=0.8 and $\phi_j$=1.2 conditions, but higher $\kappa_a$ was observed for $\phi_j$=1.2. Higher variation in $\kappa_a$ along the stoichiometric windward flame edge was observed and is in agreement with the trends in $\omega_z$ and dilatation shown in Fig. 17. Effects from three-dimensional behavior on $\kappa_a$ are expected to be most significant for the windward region. This analysis is simplified assuming the flame surface z-normal component is small and negligible along the jet centerline; in which case, the missing component in the two-dimensional $\kappa_a$ calculations is $S_{zz}$. As previously described, along the windward jet boundary $S_{zz}$ is expected to be positive. Considerations of three-dimensional behavior would thus likely lead to increased $\kappa_a$.

The trends in average $\kappa_a$ were less consistent along the leeward flame branch for the varying *y/d* locations. Examination of the $\kappa_a$ components in Fig. 4.14 show that the increase in $S_{xx}$ (and thus positive $\kappa_a$) caused by dilatation is negated by strong contribution from $S_{xy}$ toward negative $\kappa_a$ values. As a result, $\kappa_a$ along the leeward flame was dominated by $S_{yy}$. Though dilatation led to increase in $S_{yy}$ with

increased with *y/d* (not shown) changes in the flame y-normal direction, as the jet penetration changed, led to non-monotonic behavior in $S_{yy}$ (and thus $\kappa_a$). In the windward region, both dilatation and $S_{xy}$ contribute toward positive $\kappa_a$; however, in the leeward region $S_{xy}$ contributes negatively to $\kappa_a$. This suggests that increased flame-shear layer interactions along the leeward flame branch would shift $\kappa_a$ toward zero or more negative values. The behavior is evidenced by comparing $\kappa_a$ in the leeward flame nearfield at the varying *J* conditions. The increased flame-shear layer interactions at higher *J* led to lower (or a shift toward zero) $\kappa_a$. There did not appear to be any significant variation in $\kappa_a$ between the lean and rich flames, however along the stoichiometric leeward flame branch $\kappa_a$ was consistently higher.

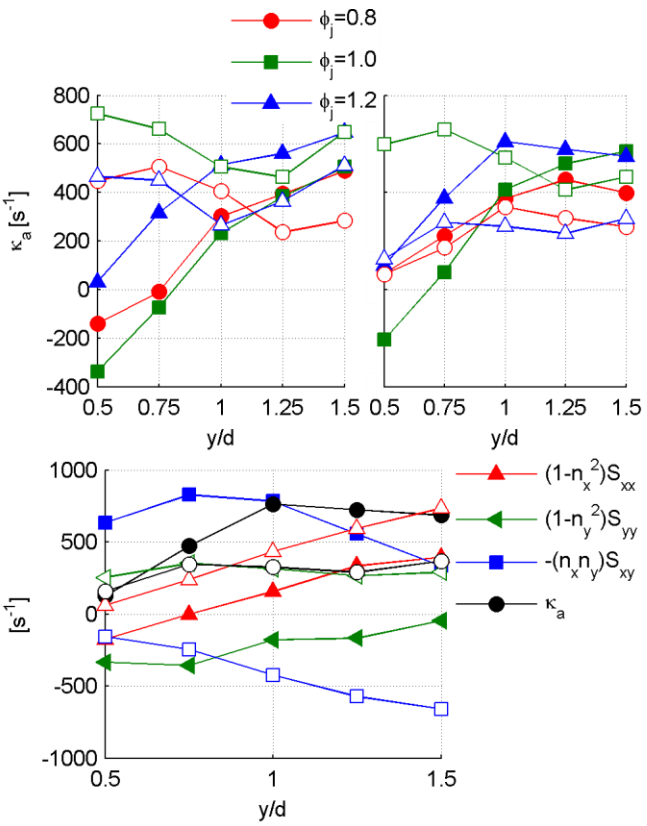


**Fig. 4.14: Top: Average $\kappa_a$ for *J* = 5.2 (left) and *J* = 8.7 (right) JICF: windward ROI (closed symbols) and leeward ROI (open symbols). Bottom: Example of contribution from $S_{xx}$, $S_{yy}$, $S_{xy}$ in calculation of $\kappa_a$ for *J* = 8.7, $\phi_j$ = 1.2.**

### *4.4.2 Flame Curvature, C*

Probability distributions of the flame curvature *C* for specified JICF conditions are presented in Fig. 4.15. The curvature distributions for the $\phi_j$=0.8 and $\phi_j$=1.2 windward flame are centered about zero, with similar distribution at the different *y/d* locations. The curvature distributions for the leeward flame show opposite different trend; the distribution of curvature narrows with increasing *y/d* location. For the windward flame where flame-vortex interactions are prevalent, positive and negative curvature effects were both observed (see Fig. 4.9). This confirms why the curvature probability distributions are centered about zero. The very slight broadening of the curvature distribution with increased *y/d* location (evidenced by the decrease in peak probability value) is most likely related to the growth in vortex structures along the jet trajectory. As the vortices convect away from the jet, they grow in size. As shown, larger vortices appeared to have a more significant effect on the flame thickening behavior. Thus, for the windward flame it is likely that the larger vortices at the higher *y/d* locations more significantly affect the flame curvature. The curvature distributions appeared independent of jet equivalence ratio. In the windward region, flame separation from the shear layer was much less frequent and thus the curvature probability distributions reflect this.

The opposite trend in curvature statistics with *y/d* for the leeward flame can be attributed to more pronounced separation between the flame and shear layer with increasing *y/d*, relative to the windward flame branch. Because no large scale rollups were observed in the leeward region, the primary source of leeward flame curvature is most likely small scale wrinkles that form when the flame resides in the shear layer. This is evidenced by broad curvature distributions at *y/d*=0.5, where flame shear layer interactions were most common. As the leeward flame *y/d* position increased, the curvature distributions began to narrow and converge onto one another with a stronger peak at zero curvature. For the rich jet conditions, for *y/d*>0.5, the curvature distributions were more aligned. This behavior is

consistent with the flame moving further from the shear layer, with this occurring fastest for the rich and stoichiometric jet cases. Though not shown here, the same trends were generally observed for the $J$=5.2 condition. The distribution of curvature at $y/d$=0.5 was slightly narrower, as less leeward flame-shear layer interactions occurred at this lower $J$ value. At $J$=5.2 the windward curvature distributions were also observed to show closer agreement for the varying $y/d$ locations, possibly due to weaker vortex formation along the shear layer.

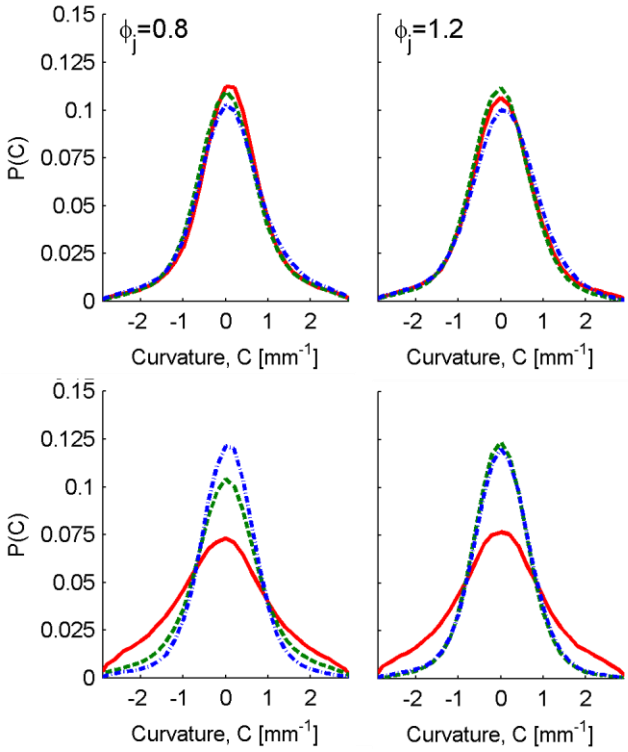


**Fig. 4.15: Probability distributions of *C* for JICF windward flame (top) and leeward flame (bottom) branches: *y/d* = 0.5 (red-), *y/d* = 1.0 (green--), *y/d* = 1.5 (blue-.-).**

### 4.5 Summary and Conclusions

Results are presented from high speed chemiluminescence imaging and simultaneous OH, $CH_2O$ PLIF and PIV of lean, stoichiometric, and rich premixed jets injected into hot, vitiated crossflow. From these measurements the following conclusions were determined:

- Unsteady windward flame stabilization was supported by flame propagation and ignition kernel formation ahead of the lifted flame front for all $\phi_j$.
- For all $\phi_j$ the leeward flame branch exhibited consistent behavior.
- Both the windward and leeward flame branches were observed to anchor in the jet shear layer.
- Instances of extended reactant preheating ahead of the windward flame were observed, which suggested auto-ignition behavior.
- Thickened preheat regions were also observed to coincide with the location of vortex rollup along the windward jet shear layer.
- Thickened heat release regions were also observed in the vicinity of vortex structures. Flame merging between thin flame branches and ignition structures, formed in the vortex core, as well as flame folding are thought to be the source for the thickened heat release regions.
- High strain along the thin flame branches extending from the thickened flame region was thought to affect CH* formation, thus giving the appearance of isolated ignition kernels in the high speed chemiluminescence images. Flame-vortex interactions were not observed along the leeward flame branch as they were along the windward branch.
- Dilatation measurements were shown to accurately follow the heat release behavior along the leeward and windward flame edges when the flame resided outside of the shear layer. As predicted by laminar flame simulations, dilatation was weakest for the lean flame and highest for the rich and stoichiometric flames.
- The lean flame was also characterized by the highest amount of flame-shear layer interactions, while the rich and stoichiometric flames were able to traverse the shear layer and move into the bulk jet flow.

- Stabilization of the premixed JICF flame was divided into two regimes: (1) flame-shear layer interaction and (2) flame stabilization in the bulk jet flow. Stabilization in the bulk jet flow suggested consumption of purely jet mixture and thus premixed flame propagation is the likely flame stabilization mechanism in these regions. In the instances where the flame stabilizes in the shear layer, auto-ignition and flame propagation are likely to contribute to the flame stabilization.
- Observation of windward flame anchoring closer to the crossflow confirms that auto-ignition was most likely the dominant mechanism in the flame-shear layer regime.
- Flame strain along the windward flame branch increased monotonically with flame *y/d* location; however proper characterization of flame strain using three-dimensional measurements may affect this behavior.
- Along the leeward flame no monotonic trends were observed for flame strain. Shear-strain caused a shift toward negative flame strain, while dilatation acted oppositely.
- Results from this study suggest that leaner jet conditions or increased *J* leads to increased flame-shear layer interactions and ultimately, increased flame strain.

# CHAPTER FIVE

# 5. Computational Analyses

### Introduction

In this Chapter, results from computational analyses are presented to determine the accuracy of 2-D dilatation as a marker of heat release and flame location. In *Section 2.5.2* relations were provided to show how both heat release and thermal diffusion effect dilatation in a reacting flow field. In Chapter 4, comparison of the computed 2-D dilatation from PIV, and heat release, determined from simultaneous PLIF imaging, showed that agreement between dilatation and heat release was dependent on the flame position in the flow field. In the instances that the flame stabilized in the shear layer, dilatation did not accurately mark the heat release/flame location; however, when the flame edge resided away from the shear layer, in the bulk jet flow, dilatation and heat release location showed good agreement. This bi-modal behavior motivated further investigation between heat release and dilatation. For the numerical analyses, three different CHEMKIN models were used: (1) 1-D premixed flame, (2) counterflow flame, and (3) plug flow reactor calculations. The 1-D premixed flame calculations were conducted to validate the dilatation equations shown in *Section 2.4.2*. The counterflow flame simulations served to determine the effect that strain rate has on dilatation and heat release. The plug flow reactor calculations were conducted for analysis of JICF auto-ignition behavior, which included investigation into how jet and crossflow mixing affect ignition delay time, heat release, and dilatation.

### 5.1 1-D Premixed Flame

The 1-D premixed flame simulations were conducted using the CHEMKIN-PRO Premix model. In Chapter 4, results from these simulations were presented for quantification of unstretched laminar

flame properties of the premixed jet mixture(s). In this section, the 1-D premixed flame calculations are used to validate eq. (10c) (*Section 2.4.2*), which shows dilatation to be a function of heat release, temperature, and mixture mean molecular weight. Output data from the 1-D simulations included all quantities required to solve eq. (10c) and was post-processed in MATLAB for the dilatation analysis. Because the grid on which the final solution was obtained was non-uniform, the finite difference approximation method described in [13] was used to calculate derivatives.

**Table 5.1: Laminar Flame Properties for premixed ethylene and air at T = 300 K (same table shown in *Section 2.3*).**

| Jet Equivalence Ratio $\phi_i$ | Adiabatic Flame Temperature [K] $T_{ad}$ | Laminar Flame Speed [cm-s$^{-1}$] $S_L^0$ | Laminar Flame Thickness [mm] $\delta_T^0$ | Maximum Heat Release [kJ-cm$^{-3}$-s$^{-1}$] $q_{max}$ | Maximum Dilatation [s$^{-1}$] $(\nabla \cdot \vec{u})_{max}$ |
|---|---|---|---|---|---|
| **0.8** | 2170.67 | 50.03 | 0.33 | 5.97 | 9939.42 |
| **1** | 2367.69 | 64.13 | 0.29 | 8.93 | 16405.41 |
| **1.2** | 2364.91 | 65.46 | 0.28 | 8.92 | 17441.35 |

The primary reason for using the 1-D premixed flame simulation to validate eq. (10c) was that all quantities were solely a function of axial distance *x* along the solution grid, and thus derivatives in any other direction were zero. Derivatives with respect to time were also zero, such that $\frac{DT}{Dt} = u\frac{dT}{dx}$ and $\frac{D\bar{W}}{Dt} = u\frac{d\bar{W}}{dx}$. The left hand side of eq. (10c), was calculated using 1-D velocity field data such that $\nabla \cdot \vec{u} = \frac{du}{dx}$. Temperature *T*, heat release *q*, and mixture mean molecular weight $\bar{W}$ data were provided in the CHEMKIN output file for calculation of the right hand side of eq. (10c). For extracting density $\rho$, specific heat at constant pressure $c_p$, and thermal conductivity $\lambda$, the Cantera toolbox for MATLAB was used. Configuration of the 1-D premixed simulation in CHEMKIN is straightforward, and consists only of three components: (1) inlet conditions, (2) premixed flame model, and (3) the output. The input

conditions are based on the experimental JICF jet mixtures: premixed ethylene-air with $\phi_j$ = 0.8, 1.0, and 1.2. The inlet temperature of the reactant mixture in the simulations was 300K.

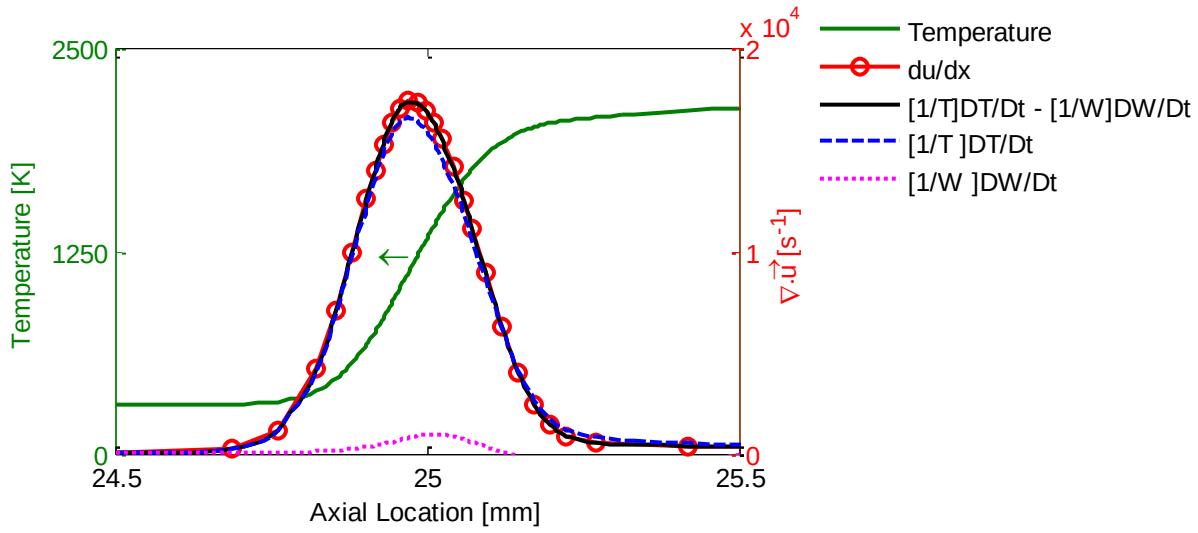


**Fig. 5.1: Comparison of dilatation calculations for $\phi_j$ = 1.2 1-D premixed flame.**

In Fig. 5.1 plots of temperature and dilatation are shown for the 1-D premixed flame; the rise in dilatation corresponds with the increase in temperature caused by the combustion reactions. The results confirm that the relation shown in equation (10b), namely, that the dilatation computed using the velocity field is equivalent to the dilatation computed using the constant-pressure ideal gas relation shown in the figure as solid black line. The results also are in agreement with Najm et al. [54], in that the contribution from $\frac{1}{\bar{W}}\frac{D\bar{W}}{Dt}$ is minimal compared to $\frac{1}{T}\frac{DT}{Dt}$.

A more detailed look into the contribution from thermal diffusion and heat-release on dilatation is presented in Fig. 5.2. The first major observation is that the peak in $\nabla \cdot \vec{u}$ does not align spatially with the location of peak heat release, $\frac{q}{T\rho c_p}$, but instead aligns with the location of the max temperature gradient. The rise of dilatation aligns with the rise in thermal diffusion, as a result of reactant preheating by the flame. As heat release begins to increase the thermal diffusion decreases, such that the

peak in $\nabla \cdot \vec{u}$ is reached before the peak heat release is reached. As expected, the maximum heat loss from the flame occurs at the same location as the maximum heat release, which causes the two terms to act against one another. Therefore, the peak (magnitude and location) of $\nabla \cdot \vec{u}$ falls between the peak for $\frac{q}{T\rho c_p}$ and $\frac{\nabla\cdot(\lambda\nabla T)}{T\rho c_p}$.

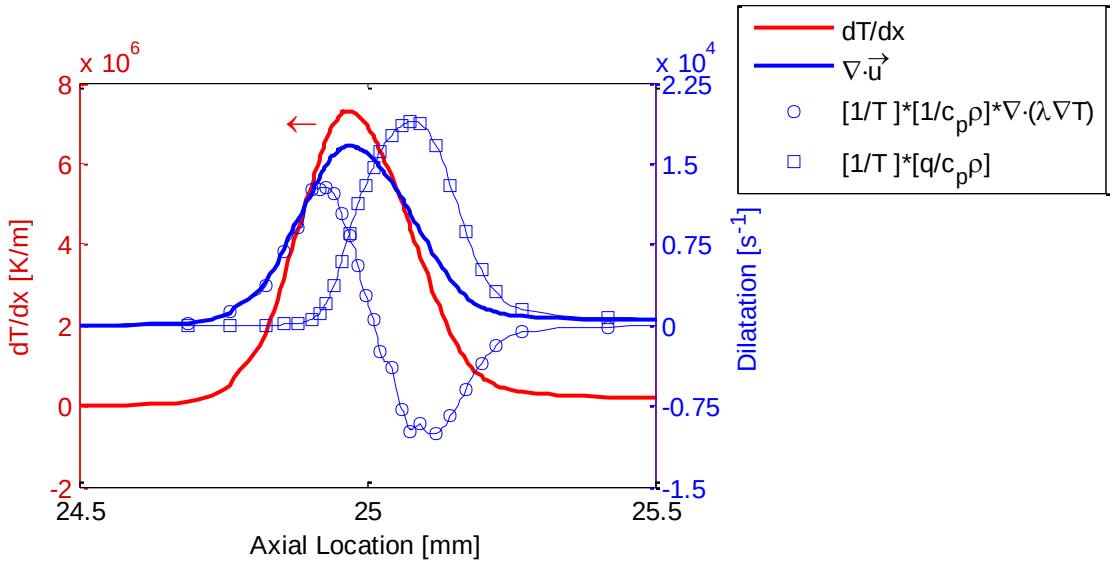


**Fig. 5.2: Profiles of temperature gradient (left y-axis) and dilatation (right y-axis) for the $\phi_j$ = 1.2 1-D premixed flame calculations.**

In order to accurately use dilatation as a marker of heat release, further analysis is still required. One way to do so is to examine peak dilatation versus peak heat release for the varying $\phi_j$ conditions. In Table 5.1 it is shown that the peak heat release for the lean jet is approximately 33% less than that of the rich jet, while dilatation is 43% less. The stoichiometric and rich jet conditions have nearly identical heat release; however, the peak dilatation for the stoichiometric jet is approximately 6% lower than for the rich jet. Looking at the data presented in Fig. 5.3, it is clear why there is discrepancy in dilatation between $\phi_j$ = 1.0 and $\phi_j$ = 1.2 even though the peak heat release is nearly identical. The contribution toward dilatation from the thermal diffusion term is stronger for the rich jet condition, and thus the peak

dilatation is higher. This is a direct result of a higher temperature gradient for the $\phi_j = 1.2$ condition. It follows appropriately then, that the decrease in peak dilatation for $\phi_j = 0.8$ is greater than the decrease in peak heat release, as both $T_{ad}$ (and max temperature gradient) and $q_{max}$ are lower at this lean jet condition.

The 1-D premixed flame calculations provided for validation of the dilatation equation presented in *Section 2.4.2* as well as reference values for the unstretched laminar premixed flames. In the next section, results from 1-D counterflow simulations are presented. In these simulations strain-rate variations are imposed on the premixed flame front, which provides for varying thermal diffusion and heat release effects. The effect of strain rate on heat release versus dilatation will be examined. In the final section of this chapter dilatation will be examined for jet reactant mixtures that have been highly diluted with crossflow mixture. This simulates mixture conditions similar to that which would be expected for JICF auto-ignition. Once again, these simulations will change the heat release and thermal diffusion effects from the flame. Determination of strain-rate and reactant dilution effects on dilatation will be useful for further understanding the behavior of dilatation in the JICF flow field.

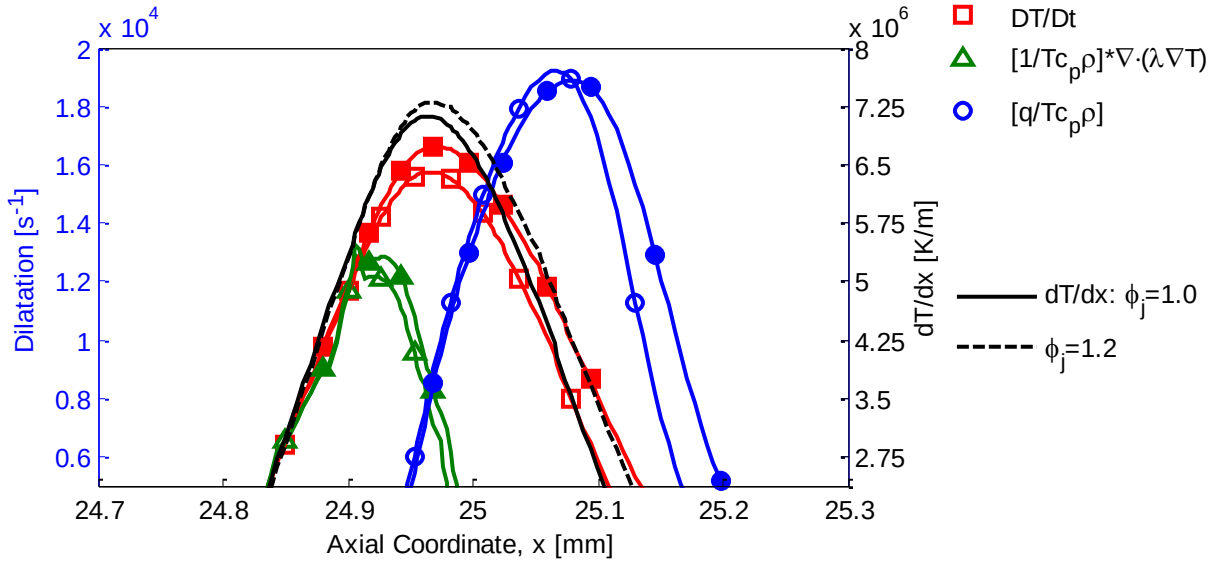


**Fig. 5.3: Dilatation (left y-axis) and temperature gradient (right y-axis) calculations from 1-D premixed flame simulations for $\phi_j = 1.0$ (open symbols, dT/dx: solid line) and $\phi_j = 1.2$ (closed symbols, dT/dx: dashed lines).**

### 5.2 Premixed Flame Counterflow Simulations

The counterflow configuration has been used extensively for both experimental and numerical combustion studies. In *Section 3.2.1* of this dissertation it was mentioned in reference to the flame stabilization behavior of the leeward flame branch. In this section, results from counterflow simulations will be presented primarily for analysis of dilatation behavior for strained premixed flames. In the JICF flowfield, high strain can be imposed on the flame when the flame interacts with the shear layer; and as such these simulations serve to understand how the heat release and dilatation are affected at these strained flow fields.

The simulations were conducted using the CHEMKIN OPPDIF software [76]. The configuration included two opposing nozzles, both containing premixed ethylene-air mixtures at the

varying $\phi_j$ conditions, as shown in Fig. 5.4. The symmetric premixed configuration was chosen to reduce effects from conductive heat loss downstream of the flame. This configuration is not representative of the premixed jet-in-crossflow flame configuration, instead it was chosen solely for the analysis of dilatation under strained flame conditions. The OPPDIF model simulates 1-D flame conditions, such that temperature, density, and axial velocity are functions of the axial direction only $\left(\frac{\partial T}{\partial y} = \frac{\partial \rho}{\partial y} = \frac{\partial u}{\partial y} = 0\right)$. The separation between the two nozzles was kept constant at 2 cm. Premixed ethylene-air was injected from both nozzles with identical velocities so that the stagnation plane was located at the center of the domain, 1 cm from each nozzle exit. The chosen nozzle separation distance was large enough to ensure that at low strain conditions there was no heat loss from the flame to the nozzles, but it was kept small enough to maintain efficient computing times.

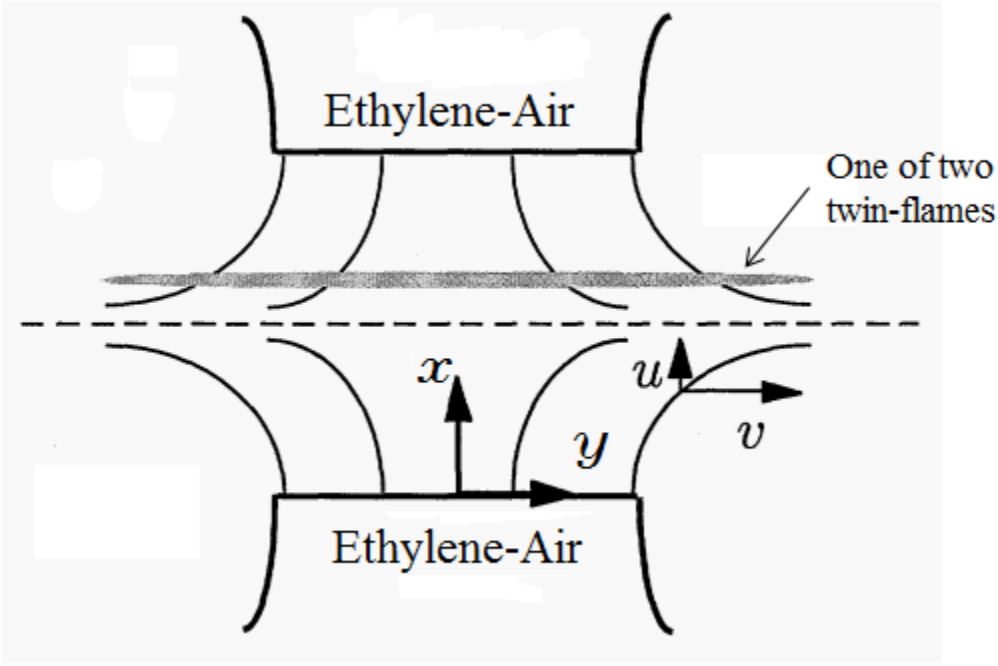


**Fig. 5.4: OPPDIF geometry configuration, adapted from [76].**

Different strain rate magnitudes were imposed on the premixed flame front by increasing the nozzle exit velocity. The strain rate definition used for the dilatation analysis was the maximum

absolute axial velocity gradient upstream of the flame edge, referred to as $\kappa_x$. The axial velocity gradient was determined through central differencing approximation using the output velocity data from CHEMKIN. An example of the calculation for $\kappa_x$ is shown in Fig. 5.5. To study the effect of $\kappa_x$ on flame behavior, $\kappa_x$ was increased (by increasing nozzle velocity) until no solution could be obtained. The maximum strain rate that solutions were obtained was dictated by the mixture equivalence ratio. For the $\phi_j$ = 0.8, 1.0, and 1.2 conditions the maximum $\kappa_x$, denoted $\kappa_{ext}$ were 1826 $s^{-1}$, 4630 $s^{-1}$, and 4881 $s^{-1}$, respectively. Beyond these strain rates flame extinction occurred and no solution can be obtained.

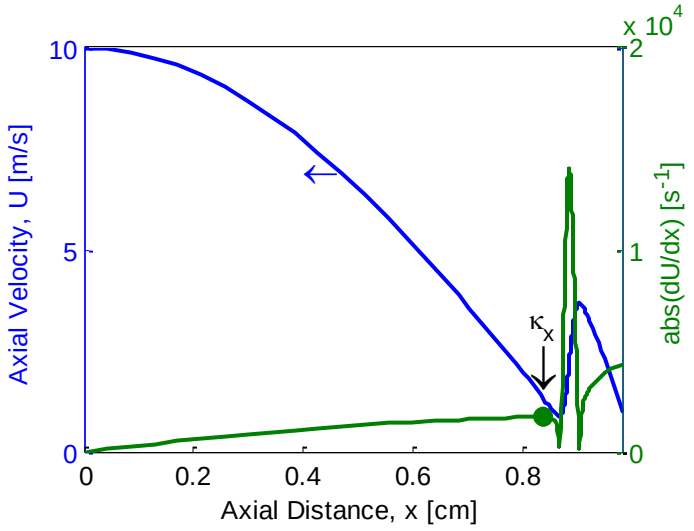


**Fig 5.5: Axial-velocity profile (left y-axis) and absolute axial velocity gradient profile (right y-axis) for $\phi_j$ = 1.2 and $\kappa_x$ = 1725 $s^{-1}$. Stagnation plane is located at *x* = 1.0 cm.**

For the extinction of a counterflow flame both flame speed and Lewis number, *Le*, effects must be considered. The flame speed controls where the premixed flame is situated in the flowfield. Higher strain, generated by increased nozzle exit velocity, forces the flame to stabilize closer to the shear layer where the flame propagation speed achieves dynamic balance with the flow velocity. As the flame moves toward the stagnation zone, *Le* becomes important. In Law [15], it is stated that for *Le* > 1, where *Le* = $\alpha/D$, flame extinction results due to increased heat loss as the flame moves toward the stagnation

zone. The flame temperature eventually decreases to the point at which chemical reaction can no longer be sustained. For $Le \leq 1$ flame extinction results from insufficient residence time for reaction as the flame position becomes restrained to the stagnation plane. For the counterflow premixed ethylene-air mixture with $\phi_j$ varying from 0.8 to 1.2, *Le* was computed. The mixture thermal diffusivity $\alpha$ and species mass diffusivity *D* were computed at 300 K. The species mass diffusivity was computed for the deficient species, relative to $N_2$, where $C_2H_4$ was the deficient species for the lean mixture condition and $O_2$ was the deficient species for the stoichiometric and rich mixture conditions. The resulting *Le* for the T = 300 K, $\phi_j$=0.8, 1.0, and 1.2 mixtures were 1.33, 1.01, and 1.00, respectively.

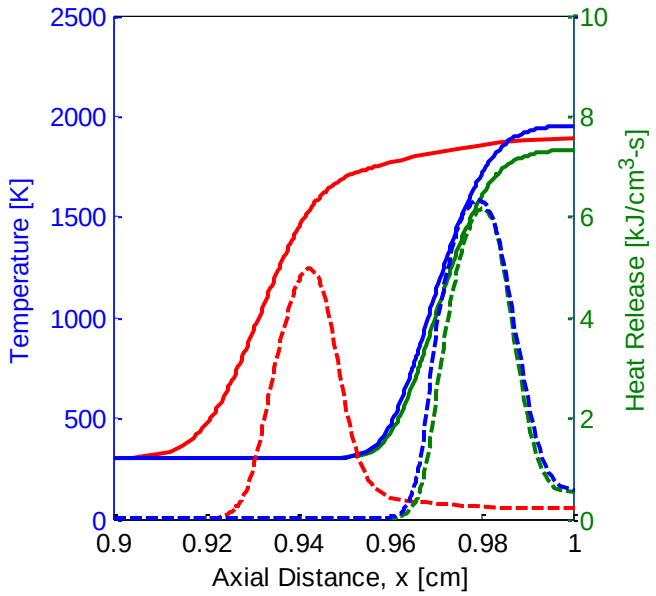


**Fig. 5.6: Temperature (solid lines) and heat release (dashed lines) profiles for premixed ethylene-air counterflow flames at $\kappa_{ext}$: $\phi_j$ = 0.8 (red), 1.0 (green), and 1.2 (blue). The stagnation plane is located at *x* = 1 cm.**

In Fig. 5.6 the profiles of temperature and heat release are shown for the lean, stoichiometric, and rich mixtures at near extinction strain-rates. All three flames were observed to extinguish before the

flame reached the stagnation plane, which was located at $x$ = 1 cm. Because $Le$ > 1 for the $\phi_j$ = 0.8 mixture, it is expected that this flame extinguished farthest from the stagnation plane. The lean jet mixture also had significantly lower flame speed than the stoichiometric and rich jet mixtures, and thus extinction was reached at a much lower strain rate condition. The stoichiometric and rich jets extinguished at nearly the same location spatially, closer to the stagnation plane than the lean jet. For these mixtures $Le$~1; thus the flame was able to survive closer to the stagnation plane. Though the laminar flame speeds were nearly identical for the stoichiometric and rich mixtures, $Le$ for the stoichiometric jet was greater than the rich jet, which most likely allowed the rich flame to survive the slightly higher strain-rate conditions.

For dilatation calculation of the counterflow flames, the necessary velocity field information provided from CHEMKIN was insufficient. For the 2-D counterflow flame $\nabla \cdot \vec{u} = \frac{\partial u}{\partial x} + \frac{\partial v}{\partial y}$; however, velocity information in the *y-direction* was unknown. Thus, dilatation from the counterflow flame simulations was computed using the relation $\nabla \cdot \vec{u} = \frac{1}{T}\frac{DT}{Dt} - \frac{1}{\bar{W}}\frac{D\bar{W}}{Dt}$. Confidence in using this relation was established first using the 1-D premixed flame simulations. In Fig. 5.7 profiles of temperature, *du/dx*, and $\nabla \cdot \vec{u} = \frac{1}{T}\frac{DT}{Dt} - \frac{1}{\bar{W}}\frac{D\bar{W}}{Dt}$ are shown. From these profiles it is clear that there is disagreement between *du/dx* and $\frac{1}{T}\frac{DT}{Dt} - \frac{1}{\bar{W}}\frac{D\bar{W}}{Dt}$, as expected since *dv/dy* also contributes to the dilatation in the counterflow flame configuration. Once again it is also confirmed that the contribution from $\frac{1}{\bar{W}}\frac{D\bar{W}}{Dt}$ toward dilatation is significantly less than the contribution from $\frac{1}{T}\frac{DT}{Dt}$.

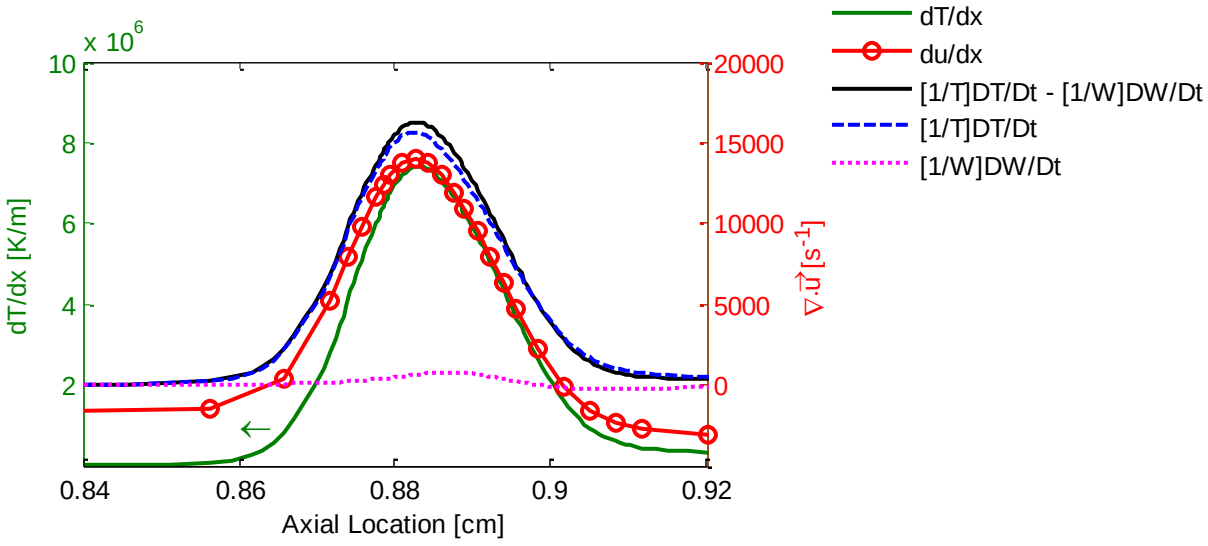


**Fig. 5.7: Temperature and dilatation profiles for the counterflow flame configuration. The case shown is for $\phi_j$ = 1.2, $\kappa_x$ = 1725 $s^{-1}$.**

In Fig. 5.8 plots are shown for the peak $\nabla \cdot \vec{u}$, $\frac{1}{T}\frac{q}{\rho c_p}$, and $\frac{1}{T}\frac{\nabla\cdot(\lambda\nabla T)}{\rho c_p}$ terms for the varying global strain-rate conditions for the three mixture equivalence ratios. The terms in Fig. 5.8 have been normalized by the unstretched, laminar flame peak dilatation (shown in Table 5.1) at the corresponding equivalence ratio. For the three equivalence ratios, peak heat release was observed to decrease with increasing strain-rate. This behavior is consistent with what is expected for the given *Le* mixtures. At low strain-rate conditions, the decrease in $\nabla \cdot \vec{u}$ appears proportion to the decrease in $\frac{1}{T}\frac{q}{\rho c_p}$. Beyond the region of proportionality (approximate $\kappa_x$ = 1273, 1714, and 2121 $s^{-1}$ for $\phi_j$=0.8, 1.0, and 1.2, respectively) there is an increase in dilatation, despite the continual decrease in heat release. The rise in dilatation coincides with a sharp increase in $\frac{1}{T}\frac{\nabla\cdot(\lambda\nabla T)}{\rho c_p}$. For the lean flame condition, this rise in dilatation continues until flame extinction; however, for the lean and rich flames the dilatation once again decreases with increasing strain-rate as the flame approaches extinction.

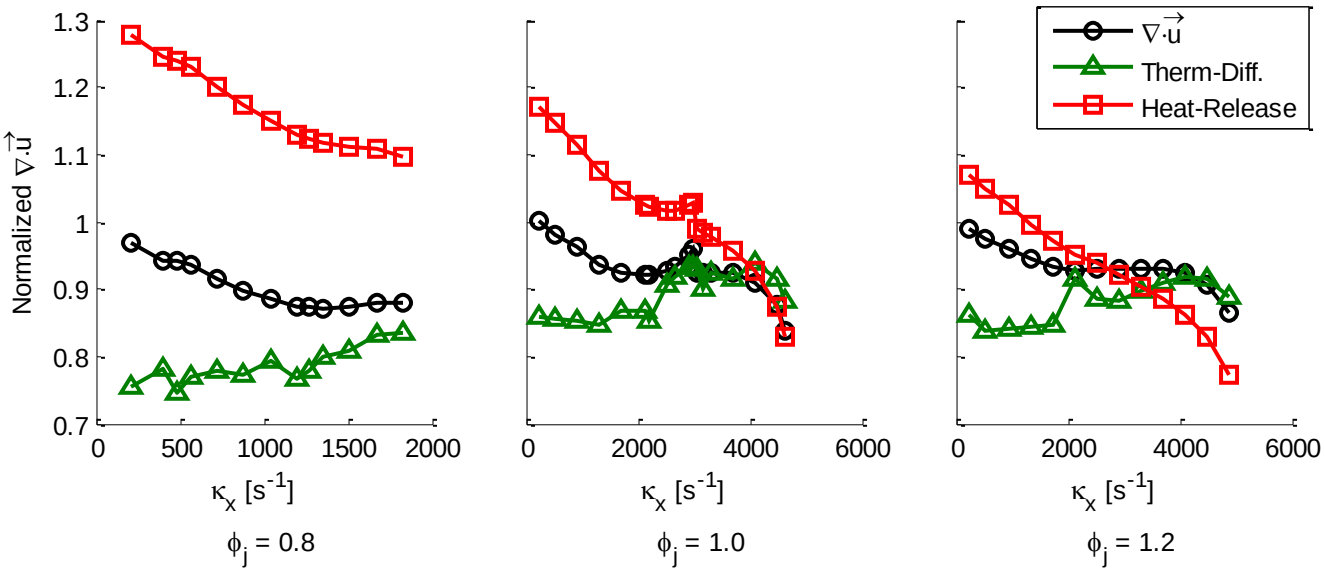


**Fig. 5.8: Plots of peak $\nabla \cdot \vec{u}$, $\frac{1}{T}\frac{q}{\rho c_p}$, and $\frac{1}{T}\frac{\nabla\cdot(\lambda\nabla T)}{\rho c_p}$ that have been normalized by the peak dilatation for the unstretched, laminar flame condition (Table 5.1).**

Plots of temperature profiles for specified global strain rates are shown in Fig. 5.9(a) for the $\phi_j$=1.2 counterflow flames. As expected, the increasing strain-rate (and thus nozzle exit velocity) forces the premixed flame to stabilize closer to the stagnation plane (located at 1 mm). While the change in strain-rate between each of the six temperature profiles shown was 500s$^{-1}$, it is clearly shown that the distance the flame moved between each of the strain-rate conditions was not constant. As the strain-rate increased, the flame location became more restrained, and thus the flame moved less with increasing strain. As shown in figure 5.9b, restraining of the flame led to a sharper decrease in flame thickness as compared to max temperature variation. In comparison to Fig. 5.8, the strain-rate at which $\delta_T/\delta_T^0$ begins to decrease faster than $T_{ad}/T_{ad}^0$ coincides with the strain-rate at which there is a slight increase in $\nabla \cdot \vec{u}$. Since $[T_{ad}/T_{ad}^0]\ /[\delta_T/\delta_T^0]$ is a rough approximation of the maximum temperature gradient, the results in Fig. 5.9 confirm that the heat loss from the flame increased as the strain-rate increased.

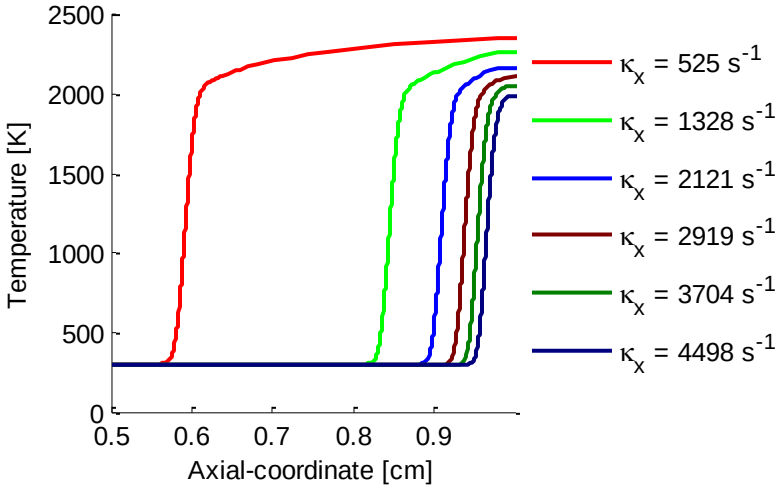


(a)

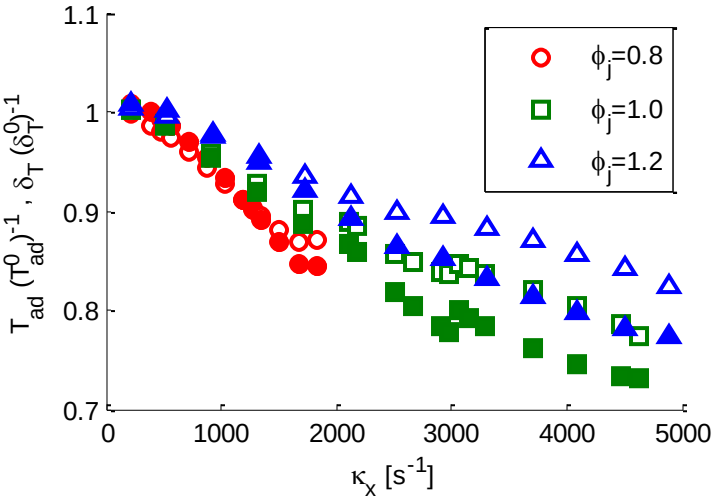


(b)

**Fig. 5.9: a) Temperature profiles for the $\phi_j$ = 1.2 counterflow flame at the specified $\kappa_x$. b) Plots of counterflow flame temperature (open symbols) and flame thickness (closed symbols) vs. $\kappa_x$. Quantities have been normalized by the respective unstretched, laminar flame values.**

In Fig. 5.10 profiles of heat release, $\nabla \cdot \vec{u}$, $\frac{1}{T}\frac{q}{\rho c_p}$, and $\frac{1}{T}\frac{\nabla\cdot(\lambda\nabla T)}{\rho c_p}$ for $\phi_j$=1.2 counterflow flame are shown for global strain-rate conditions of 250, 1250, and 1750 $s^{-1}$, respectively. The profiles at the lowest global strain-rate 250 $s^{-1}$ resemble those shown in Fig. 5.2 for the unstretched laminar flame. The spatial location of the peak in dilatation at this low strain condition falls between the peak locations for $\frac{1}{T}\frac{q}{\rho c_p}$, and $\frac{1}{T}\frac{\nabla\cdot(\lambda\nabla T)}{\rho c_p}$. The peak in $\frac{1}{T}\frac{q}{\rho c_p}$ is greater than the peak in $\frac{1}{T}\frac{\nabla\cdot(\lambda\nabla T)}{\rho c_p}$, such that $\nabla \cdot \vec{u}$ is dominated by the contribution from heat release. As, strain-rate is increased the peak in $\frac{1}{T}\frac{q}{\rho c_p}$ decreases more rapidly than the peak in $\frac{1}{T}\frac{\nabla\cdot(\lambda\nabla T)}{\rho c_p}$. This behavior is in agreement with the results shown in Fig. 5.7. The increase in contribution from $\frac{1}{T}\frac{\nabla\cdot(\lambda\nabla T)}{\rho c_p}$ also causes the peak location of $\nabla \cdot \vec{u}$ to move spatially, such that it overlaps with the peak location of $\frac{1}{T}\frac{\nabla\cdot(\lambda\nabla T)}{\rho c_p}$. Similar findings were reported in [54], for a strained v-shaped flame.

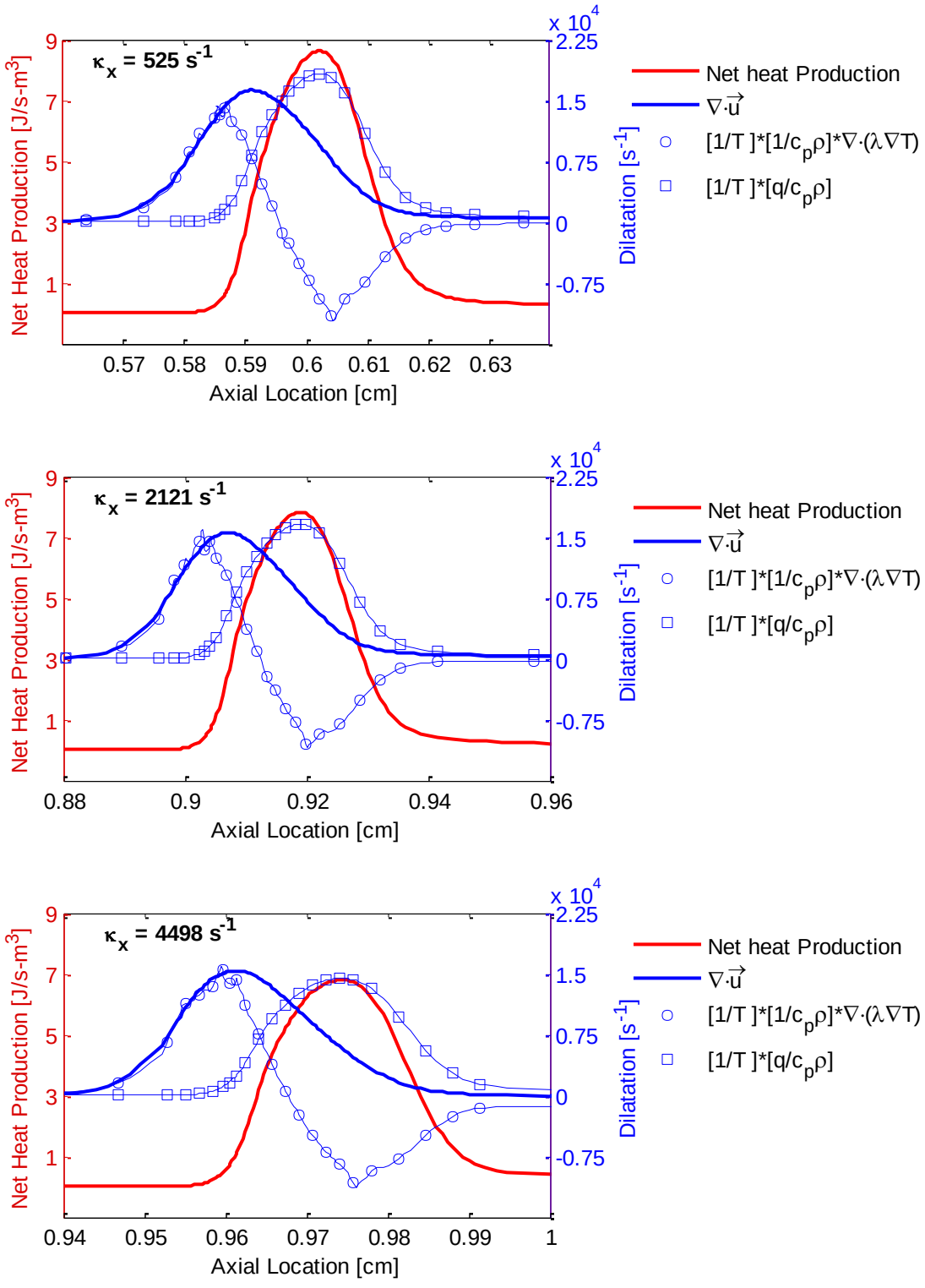


**Fig. 5.10: Profiles of heat release, $\nabla \cdot \vec{u}$, $\frac{1}{T}\frac{q}{\rho c_p}$, and $\frac{1}{T}\frac{\nabla\cdot(\lambda\nabla T)}{\rho c_p}$ for $\phi_j$ = 1.2 counterflow flame for three different $\kappa_x$.**

The dilatation results provided by the laminar counterflow flame simulations show that dilatation is not proportional to heat release for varying flame strain conditions. This is an important observation as it suggests that dilatation is not an appropriate marker for heat release from a flame undergoing high flame strain. At low strain-rate conditions heat release and dilatation are proportional; however, at high strain-rate conditions strong thermal diffusion dominates the contribution from heat release, such that heat release and dilatation are no longer proportional.

### 5.3 Plug Flow Reactor

The plug flow reactor simulations were conducted to analyze the effect of jet and crossflow mixing on jet ignition behavior. Similar techniques have been employed for JICF auto-ignition analysis by Fleck et al. [35] and Sullivan et al. [45]. In [45] auto-ignition of a fuel jet was examined numerically by varying the amount of crossflow and jet - crossflow mixing in order to determine the mixture conditions with the fastest ignition time, known as the most reactive mixture fraction. This method of determining auto-ignition time was described in detail in the Introduction, *Section 1.3*. The auto-ignition analysis of a premixed fuel-air jet was conducted similarly to that described in [45], in that the amount of crossflow dilution of the premixed jet reactants was varied in order to determine the most reactive mixture fraction and shortest ignition delay time. The dilatation behavior was also examined for the mixture conditions near the most reactive mixture fraction. Dilution of the premixed reactants by crossflow fluid composed of hot products of lean combustion was observed to affect the adiabatic flame temperature and total heat release, both of which, have been shown to affect the dilatation measurement.

The plug flow reactor calculations were conducted using CHEMKIN-PRO software. Three main components were required to simulate the JICF auto-ignition, as pictured in Fig. 5.11: 1) jet and crossflow inlets, 2) adiabatic, non-reactive homogenous mixer, and 3) plug flow reactor. As described in *Section 2.2*, the equilibrium solver was used to determine the composition of the crossflow. The inlet

temperature of the crossflow mixture was adjusted to 1500K to maintain agreement with the experimental conditions. The jet and crossflow were mixed in the adiabatic, non-reactive homogenous mixer. Dilution of the jet mixture was varied by maintaining constant jet mass flow rate and varying the crossflow mass flow rate entering the mixer. The resulting jet-crossflow mixture exiting the mixer was sent to the plug flow reactor for determination of the auto-ignition behavior.

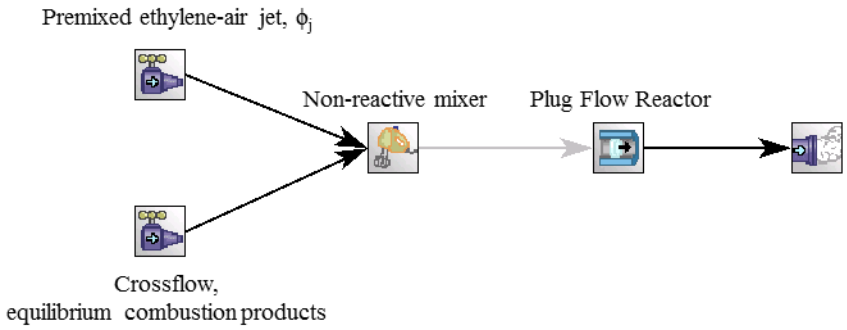


**Fig. 5.11: Configuration for plug flow reactor calculation.**

In Fig. 5.12 plot of ignition delay time are shown for the lean, stoichiometric, and rich jet conditions at various crossflow dilution levels. The dilution level corresponds to the fraction of crossflow mass flow in the total jet and crossflow mixture, such that $Z = \dot{m}_{\infty}/(\dot{m}_{\infty} + \dot{m}_{j})$. The ignition delay time was computed using the same method described in [45]; $\tau_{ign}$ is the time at which the temperature is equivalent to $T_{ign} = T_{mix,in} + 0.5 * (T_{max} - T_{mix,in})$, where $T_{mix,in}$ is the initial temperature of the diluted jet mixture entering the plug flow reactor and $T_{max}$ is the maximum temperature reached in the plug flow reactor for the given mixture. As shown in Fig. 5.12(a), there is a steady decrease in $\tau_{ign}$ from $Z$ = 0.4 to 0.8. For $Z$ < 0.4, auto-ignition was still possible; however $\tau_{ign}$ was beyond any practical time scale. For Z > 0.8, the change in $\tau_{ign}$ with $Z$ became much less drastic; this is shown more clearly in Fig. 5.12(b). For each jet equivalence ratio there is a $Z$ at which $\tau_{ign}$ is minimum,

this is referred to as the most reactive mixture fraction, or $Z_{MR}$. Table 5.2 shows the results for $Z_{MR}$ and $\tau_{ign,min}$ for the different $\phi_j$.

**Table 5.2: Results from plug flow reactor calculations for JICF auto-ignition analysis.**

| $\phi_j$ | $Z_{MR}$ | $\tau_{ign,MR}$ [ms] |
|---|---|---|
| 0.8 | 0.877 | 0.104 |
| 1 | 0.895 | 0.108 |
| 1.2 | 0.911 | 0.111 |

For determination of $Z_{MR}$ a 2$^{nd}$-order polynomial function was fitted to $\tau_{ign}$ for $0.84 \leq Z \leq 0.94$. The polynomial fit was differentiated to determine the location of the minimum and thus $Z_{MR}$ and then $\tau_{ign,MR}$ was calculated. The polynomial fits are overlaid on the CHEMKIN data in Fig. 5.12(b). The fastest ignition time occurred for the lean jet mixture and the fastest ignition delay time for the stoichiometric and rich jet conditions was approximately 4% and 7% longer, respectively. As expected, $Z_{MR}$ occurred at highly diluted jet mixtures, where mixture initial temperatures were high due to high crossflow fluid concentration. This behavior is in agreement with [21], [45]. With increasing $\phi_j$ the most reactive mixture fraction moved toward more diluted jet mixtures, such that $Z_{MR,\phi=0.8} < Z_{MR,\phi=1.0} < Z_{MR,\phi=1.2}$.

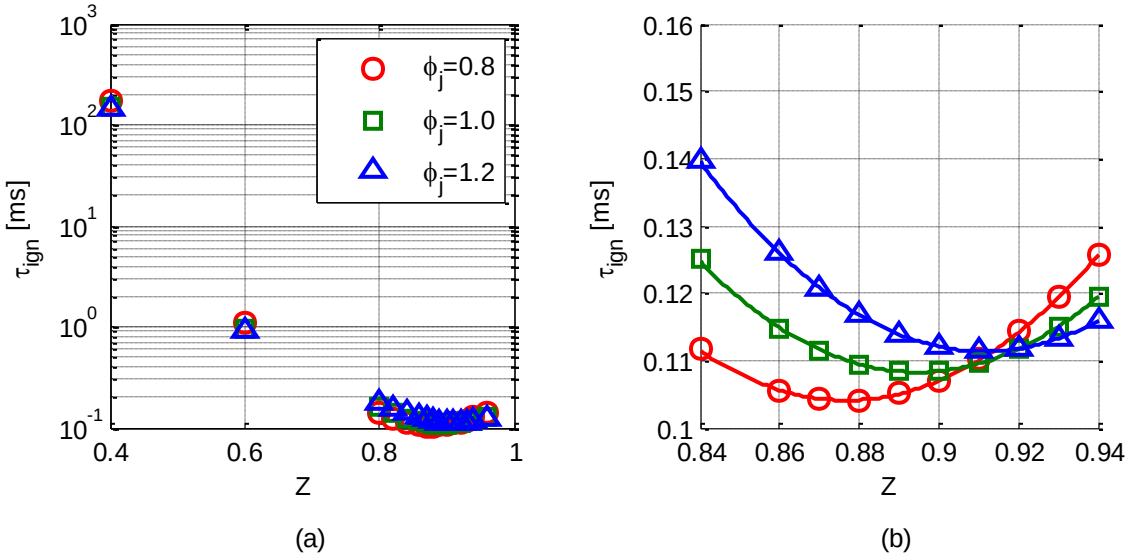


**Fig 5.12: (a) Ignition delay time $\tau_{ign}$ for the varying $\phi_j$ vs. *Z*. (b) Zoomed in view of $\tau_{ign}$ overlaid with 2$^{nd}$-order polynomial line fits.**

Analysis of the inlet mixture temperature as a function of Z revealed that the lean jet mixture had higher inlet temperature. Because $c_p$ of ethylene (1.53 kJ/kg-K at 300 K [77]) is higher than $c_p$ of air (1.01 kJ/kg-K at 300 K) more heat is required to increase the temperature of the richer jet mixtures. Because the enthalpy of the crossflow mixture was maintained constant for varying $\phi_j$ it is appropriate that the inlet temperature of the lean jet-crossflow mixture was higher at each *Z*. The shift to higher *Z* with increased equivalence ratio is a result of this behavior. Table 5.3 shows the predicted flame liftoff heights using $y_{flame} = V_j * \tau_{ign}$ at *J* = 5.2 and *J* = 22.7. The results show that the predicted liftoff heights vary by only $0.006d_j$ at *J* = 5.2 and $0.012d_j$ at *J* = 22.7. The change in $\tau_{ign}$ with $\phi_j$ was thus, insignificant relative to the change in $\tau_{ign}$ with *Z*.

**Table 5.3: Predicted flame liftoff height using $\tau_{ign}$. Liftoff heights have been normalized by jet diameter $d_j$.**

| $\phi_j$ | $J$ = 5.2 $y_{flame}/d_j$ | $J$ = 22.7 $y_{flame}/d_j$ |
|---|---|---|
| 0.8 | 0.086 | 0.179 |
| 1 | 0.089 | 0.186 |
| 1.2 | 0.092 | 0.191 |

In analysis of the high speed chemiluminescence images in Chapter 4, there was no noticeable difference between the location at which ignition kernels formed for the lean, stoichiometric, and rich jet conditions. This is consistent with the $\tau_{ign}$ calculations. The formation of these kernels were instead, affected more strongly by windward flame liftoff height. As previously explained, for increased flame liftoff heights, more jet and crossflow mixing upstream of the stable flame base allowed for auto-ignition. For the windward flame, the liftoff height was consistently higher and windward flame blowoff occurred more frequently, and as a result ignition kernel formation appeared more frequently for the lean JICF.

From the PLIF-PIV results presented in Chapter 4, it was observed that the rich and stoichiometric flames were able to stabilize away from the shear layer in the bulk jet flow. In this region of flame stabilization, it is safe to assume that $Z$ is close to zero, as the combusting mixture will contain mostly jet reactants. From the plot in Fig. 5.12(a) it is shown that as $Z$ moves toward zero, $\tau_{ign}$ can becomes exceedingly large and eventually auto-ignition is no longer possible. At these low $Z$ values it is then appropriate to compare timescales between auto-ignition and flame propagation [78]. A flame propagation timescale was determined using the relation $\tau_{prop} = \alpha/(S_L^0)^2$, where α is the thermal diffusivity evaluated at the location of maximum temperature gradient in the premixed laminar flame solution. The respective $\tau_{prop}$ for the $\phi_j$ = 0.8, 1.0, 1.2 conditions are 0.768, 0.486, 0.477 ms,

respectively. Assessment of $\tau_{ign}$ in Fig. 5.12(b) confirms that $\tau_{prop}$ becomes faster than $\tau_{ign}$ when $0.6 \leq Z \leq 0.8$. This analysis confirms that premixed flame propagation is most likely the dominant flame stabilization mechanism as the flame moves away from the shear layer. Furthermore, $\tau_{prop}$ for the $\phi_j$=0.8 conditions is approximately 60% slower than it is for the stoichiometric and rich jet mixtures. The stoichiometric and rich jet flame are able to move away from the shear layer faster, due to faster $\tau_{prop}$; whereas, for the lean flame jet flow velocities are still too high relative to $\tau_{prop}$, and so the lean flame remains anchored in the shear layer longer, where $\tau_{ign}$ dominates.

Experimentally measured values of ignition delay time have been shown vary in comparison to $\tau_{ign}$ computed using homogenous reactor simulations. Experimental $\tau_{ign}$ has been shown to vary significantly from $\tau_{ign}$ computed using $Z_{MR}$ [35], [78]. In Table 5.2, the value of $\tau_{ign,MR}$ is in good agreement with the experimental ignition time shown in Chapter 3 for the $J > 5.2$, $\phi_j$=1.2 JICF. The experimental ignition delay time for the J > 5.2 JICF is approximately 0.04 ms longer. In Chapter 3, dilatation was used to determine the flame location and it has since been shown that dilatation is not accurate for determining flame location when the flame resides in the shear layer. Thus the slightly higher experimental ignition delay time is most likely a result of error associated with using dilatation. Re-evaluation of experimental $\tau_{ign}$ could not be determined using the PLIF-PIV results, as the entire JICF flow field was not imaged; however, resolving the flame in the shear layer with PLIF imaging would lower $\tau_{ign}$ such that it is possible that the experimentally and numerically computed values of $\tau_{ign}$ may even be in closer agreement.

Analysis of the auto-ignition and plug flow reactor simulations also confirm why the JICF liftoff height cannot be determined by simple scaling, as conducted in Chapter 3. The wide range of ignition timescales with varying $Z$ suggest that the timescale associated with flame liftoff is highly dependent on the local flow conditions at the leading flame edge. Similarly, flame propagation timescales must also

be considered; proper characterization of the JICF flame propagation time scale also requires knowledge of the local mixture conditions as well as flame stretch behavior. As stated in [53], development of liftoff correlations for jet flames in highly heated vitiated crossflow is a difficult task and cannot be accomplished by considering only the global flow/mixture conditions. The JICF flame stabilization is highly coupled with local flow conditions and thus scaling of liftoff requires consideration of these instantaneous conditions.

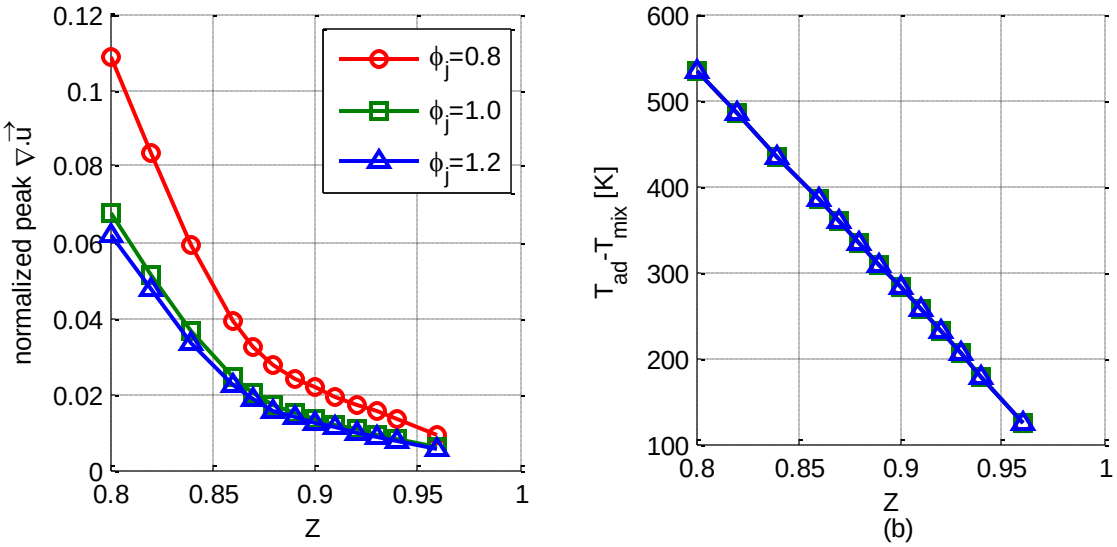


**Fig. 5.13: (a) Plot of peak $\nabla \cdot \vec{u}$ versus *Z* and (b) $T_{ad}$ - $T_{mix}$ versus *Z*. The peak $\nabla \cdot \vec{u}$ has been normalized by peak dilatation from the laminar, unstretched flame calculations (Table 5.1).**

In Fig. 5.13(a), peak dilatation profiles, normalized by unstretched, laminar flame peak dilatation, are shown as a function of *Z* for the varying $\phi_j$ conditions. As expected, peak dilatation decreases with increasing *Z*. This is due to decreasing heat release and $T_{ad}$ caused by decreasing fuel mass fraction with increasing crossflow dilution. For analysis of $\nabla \cdot \vec{u}$, plots of normalized $\delta_T$ and $q_{max}$ are shown in Fig. 5.14. The thermal component of diffusion was examined using $\delta_T$. As shown from the counterflow simulations, smaller $\delta_T$ corresponded to higher thermal diffusion effects. For the auto-

igniting mixture, $\delta_T$ increased significantly with increasing dilution. The overall temperature increase of these highly diluted mixtures was small 100 K < ΔT < 600 K, so that the resulting temperature gradient was also small. The decrease in peak heat release was also drastic at low Z, such that near $Z_{MR}$ peak heat release was nearly reduced by 80% from the laminar flame condition. The increase in $\delta_T$ was more significant than the decrease in $q_{max}$; and thus, for Z near $Z_{MR}$ $\nabla \cdot \vec{u}$ dominated by heat release such that peak $\nabla \cdot \vec{u}$ and $q_{max}$ were proportional.

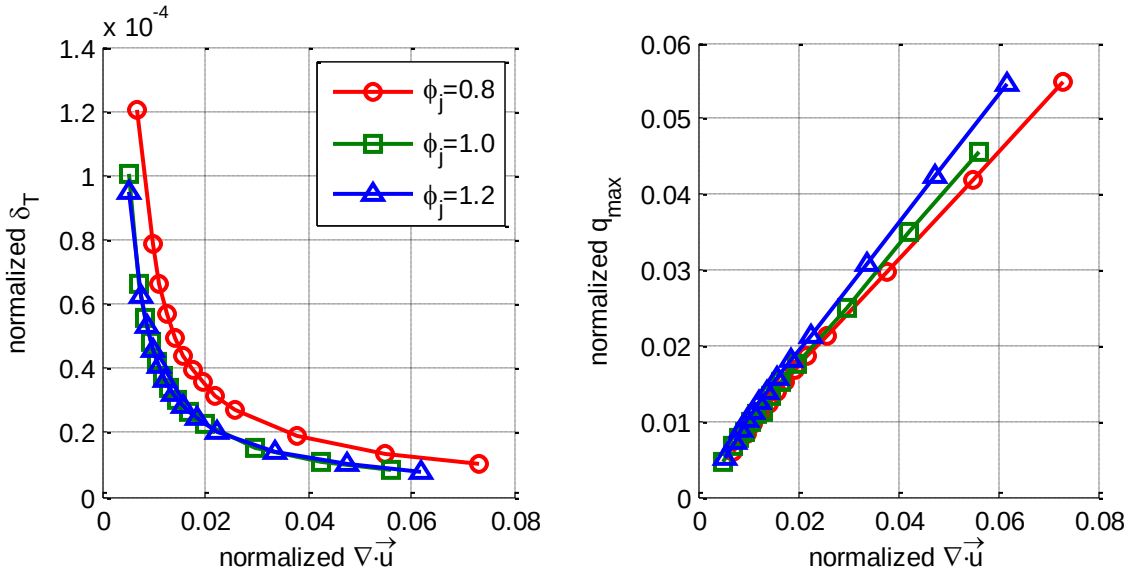


**Fig. 5.14: (a) Plot of $\delta_T$ versus *Z* and (b) Plot of $q_{max}$ versus *Z*. All quantities have been normalized by corresponding laminar, unstretched flame quantities (Table 5.1).**

### 5.4 Conclusions

In this chapter laminar flame computational analyses were performed for analysis of dilatation and auto-ignition for the premixed reacting JICF. One-dimensional premixed flame simulations were performed to validate the dilatation-ideal gas relation presented in *Section 2.4.2*. The dilatation of the 1-D unstretched premixed flame was observed to peak, spatially, before the location of peak heat release. High heat loss from the flame at the location of peak heat release was the cause for the offset in peak location. Dilatation from counterflow flame simulations was calculated after establishing confidence in

the dilatation equation from the premixed flame simulations. The strain-rate was increased for the counterflow flame configuration to determine the effect of strain-rate on dilatation. Increasing strain-rate caused the flame to move toward the stagnation plane. As the flame location became more restricted with increasing strain-rate, temperature gradients increased significantly such that thermal diffusion effects dominated heat release effects in the calculation of dilatation. Thus, at low strain heat release and dilatation were proportional, however at high strain rate locations this was not the case.

Analysis of JICF auto-ignition behavior was conducted using plug flow reactor simulations. The results showed that auto-ignition delay time was minimally affected by jet mixture equivalence ratio at highly diluted mixture conditions, where the mixture was approximately 90% crossflow. The minimum ignition delay time slightly increased with increasing equivalence ratio, however, between the lean and rich conditions minimum ignition delay time varied by only 7%. The most significant changes in ignition delay time occurred for varying crossflow dilution levels. At low crossflow dilution levels, the flame propagation time scale was faster than the ignition time scale. For the lean jet mixture, the flame propagation timescale was approximately 60% slower than for the stoichiometric and rich jet conditions. This confirmed why the stoichiometric and rich jet flames moved away from the shear layer and the lean jet flame did not. Experimental ignition delay times calculated for the $\phi_j$=1.2 JICF were in close agreement with the numerically calculated values. Difference between the two can be attributed to errors associated with using 2-D dilatation for identifying flame location.

Crossflow dilution also affected dilatation; high crossflow dilution led to low heat release, and thus low dilatation. In the region near the most reactive mixture, dilatation and heat release were proportional, as thermal diffusion effects were minimal. The dilatation results provided insight into the flame behavior for the JICF configuration. Ultimately, both dilatation and crossflow dilution reduced dilatation. For flame anchoring in the shear layer, where agreement between heat release and dilatation

was not observed, strain-rates and jet-crossflow mixing rates are expected to be high. At these conditions, decrease in dilatation, in combination with out-of-plane effects (flow divergence in the out of plane z-direction), both contribute to the lower dilatation measurements along the JICF shear layer. While the three-dimensional dilatation measurements would help to improve the accuracy of dilatation measurements, local strain-rate and mixture conditions must be characterized at the flame location in order to accurately determine the heat release behavior from dilatation.

# CHAPTER SIX

# 6. Conclusions & Future Work

## 6.1 Summary

Increased awareness of global climate change has led to a strong initiative toward developing new low-emission gas turbine combustion technology. The new generation of combustion technology is moving toward lean-premixed systems that operate in regimes where production of harmful $NO_x$ pollutants is low. There are many challenges associated with building such combustors, and so currently, extensive research is being conducted to understand how to safely incorporate LPM combustion into the new gas turbine technology. The premixed reacting JICF configuration presented in this dissertation is one such example of the research being performed on LPM combustion.

In the experiment, a high temperature vitiated crossflow composed of fuel-lean combustion products was used to replicate practical engine conditions. The jet-to-crossflow momentum flux ratio $J$ and jet equivalence ratio $\phi_j$ were the primary jet parameters investigated for characterization of the premixed JICF system. The results shown in this thesis are among the first ever for a premixed JICF. The analysis of the premixed JICF system was divided into three points of interest: (1) flame stabilization behavior, (2) reacting JICF flow field characterization, and (3) computational modeling. The experimental analyses were conducted using a variety of diagnostic techniques, including: high speed chemiluminescence imaging, high speed particle image velocimetry, and simultaneous $CH_2O$, OH planar laser induced fluorescence and particle image velocimetry. Each diagnostic technique provided for flame visualization and the PIV measurements allowed for characterization of flame-flow field interaction. Computational modeling of laminar flame behavior provided insight into flame ignition and

propagation timescales, as well as, provided for assessment of using dilatation as a marker for heat release. In the following sections a summary of the major findings from each research point of interest is presented. Following the result summaries, suggestions for future work on the premixed JICF are provided.

### *6.1.1 JICF Flame Stabilization*

The primary task in this dissertation was to gain a strong understanding of the flame stabilization behavior for the premixed jet in vitiated crossflow. While a high number of similar investigations have been performed for non-premixed JICF, the premixed JICF is still a very novel concept. The premixed flame behavior was analyzed as a function of two parameters: jet-to-crossflow momentum flux ratio $J$ and jet equivalence ratio $\phi_j$. The experimental values of $J$ ranged from 5.2 to 22.7 and lean ($\phi_j$=0.8), stoichiometric ($\phi_j$=1.0), and rich jet ($\phi_j$=1.2) jet equivalence ratios were examined. The high temperature vitiated crossflow conditions provided for auto-ignition of jet reactants, such that the flame stabilization behavior could not be characterized solely by premixed flame propagation. Similarly, differences in flame stabilization behavior at different locations in the flow field mean that there was not a single controlling stabilization mechanism for the entire JICF flame.

High speed chemiluminescence imaging was the first diagnostic technique employed. The time-resolved imaging allowed for visualization of CH* emission from the JICF flame. From these measurements the first observations of different windward and leeward flame stabilizations behaviors were made. The leeward (downstream) flame stabilization was consistent, as the flame anchored to, or slightly lifted from the jet exit. The windward (upstream) flame stabilization exhibited highly unsteady behavior; including full flame attachment, lifted flame behavior, and windward flame behavior. The unsteady windward flame showed a stronger dependence on $J$ and $\phi_j$ than the leeward flame. Increasing $J$ led to increased flame liftoff height and increased frequency of auto-ignition kernel formation

upstream of the windward flame edge. Increasing $\phi_j$ resulted in more slightly more stable flame behavior, as windward blowoff occurred most frequently for the lean flame condition. An attempt was made to determine a timescale for the $\phi_j = 1.2$ windward flame liftoff; however no trends was observed.

Further flame analysis was performed on the $\phi_j$=1.2 JICF using high speed particle image velocimetry. The flame location was identified using the 2-D dilatation computed from the velocity field. Strong flow recirculation in the jet wake suggested that stabilization of the leeward flame was supported by the presence of high temperature crossflow and combustion products. Alignment of the leeward flame shear strain-rate probability distributions at varying *J* supported previous observations that leeward flame stabilization has similarities to counterflow flame behavior. The windward flame stabilization behavior could not be characterized by average flame behavior like the leeward flame; instead, analysis of instantaneous flame and flow field behavior was required for windward flame stabilization characterization. Alignment of experimental ignition delay time and strain-rate probability distributions suggested that auto-ignition was the most likely stabilization mechanism for the $J > 5$ JICF. At the $J = 5$ condition, a narrower probability distribution in experimental flame propagation time suggested that both premixed flame propagation and auto-ignition assisted in flame stabilization. This lower *J* condition was also the only condition at which the jet could fully attach to the jet exit; confirming the premixed propagating flame observations.

Detailed visualization of the lean, rich, and stoichiometric JICF flame structure was accomplished using simultaneous $CH_2O$ and OH PLIF. Pixel-by-pixel multiplication of the $CH_2O$ and OH PLIF images allowed for identification of the heat release zone. Along the windward flame branch three different behaviors were observed: (1) attached flame, (2) lifted flame, and (3) lifted flame with extended upstream $CH_2O$ formation. The presence of $CH_2O$ well upstream of the lifted windward flame further confirmed that auto-ignition assisted in windward flame stabilization. Thickened preheat regions

and thickened flame regions were also observed along the windward flame branch. The thickened preheat regions suggested buildup of $CH_2O$ in vortex cores where jet and crossflow mixing times were long. The thickened heat release regions suggested flame folding around vortex structures, as well as possible merging between ignition kernels and thin flame branches. Along the leeward flame branch the flame structure was more consistent, with no observations of localized preheat/heat release zone thickening.

Simultaneous $CH_2O$, OH PLIF and PIV measurements confirmed the interaction between the windward flame and jet shear layer vortices. Large vortex structures had a stronger effect on heat release zone thickening, while smaller vortices often only caused thickening of the preheat zone. Along the thickened heat release zone flame strain was low; however along the thin flame braids that extended from the thickened heat release region flame strain was significantly higher. Cusp formation was also observed along the flame surface during the flame-vortex interaction, and resulted in strong negative curvature. Both the windward and leeward flames anchored in the shear layer; and observation not previously realized from high speed chemiluminescence or high speed PIV measurements. Away from the flame anchoring locations the leeward flame and rich and stoichiometric windward flames were able to separate from the shear layer such that they resided in the bulk jet flow. This suggested that flame stabilization was divided into two different regimes. In the first regime, flame anchoring in the shear-layer, jet and crossflow mixing is important for flame stabilization suggesting auto-ignition is most likely the dominant flame stabilization mechanism. In the second regime, flame anchoring in the bulk jet flow, jet and crossflow mixing is low, such that premixed flame propagation is the dominant flame stabilization mechanism.

### *6.1.2 JICF Reacting Flow Field*

High speed particle image velocimetry measurements were conducted to analyze the differences between the non-reacting and $\phi_j$=1.2 reacting jet in vitiated crossflow. For non-reacting JICF, the velocity decay along the jet centerline was steady, and scaled well with free jet centerline velocity decay. For reacting JICF, there was a distinct location along the jet centerline at which high dilatation generated by heat release led to an increase in jet centerline velocity; this resulted in increased penetration for reacting jets relative to the non-reacting jets. Until the centerline streamline crossed the flame front, the non-reacting and reacting jet trajectories aligned. Velocity increase due to heat release also led to higher vorticity along the reacting windward and leeward shear layers. The presence of combustion products in the jet wake affected the formation of the upright wake vortices that are characteristic of non-reacting JICF. At the higher *J* values, increased flame liftoff resulted in jet near field behavior that resembled the non-reacting flow field. Thus, at these high *J* upright vortices were observed in the jet wake.

Confinement effected jet penetration; as *J* increased, and jet penetration increased, differences between non-reacting and reacting jet penetration were minimized. Classic JICF trajectory correlations, developed from non-reacting JICF experiments, were unable to properly predict the highly confined non-reacting and reacting JICF penetration behavior. Two new experimental correlations were developed to describe the trajectory behavior of the non-reacting and reacting JICF, respectively. Both correlations were asymptotic to account for the maximum jet penetration set by the lateral confinement. In all, the flowfield analysis results confirmed that non-reacting JICF scaling laws cannot be used for characterization of reacting JICF behavior and that confinement has a strong effect on the JICF flowfield.

### *6.1.3 Computational Modeling*

Simulations for analysis of JICF auto-ignition and flame propagation behavior were conducted using CHEMKIN-PRO. The auto-ignition behavior was examined by changing the amount of crossflow dilution in the jet mixture and then determining the time it took the diluted mixture to ignite. The results showed that fastest ignition delay times were for mixtures with high crossflow dilution, were crossflow fluid made up approximately 90% of the total mixture mass flow rate. The lean jet had the overall fastest ignition time; however, the change in ignition delay time between the varying equivalence ratios was insignificant compared to the change in ignition time with dilution level. A flame propagation timescale was also determined for each jet mixture using one-dimensional premixed flame computations. These analyses showed that the stoichiometric and rich jet mixtures had much faster propagation timescales than the lean jet, by approximately 60%. The faster propagation timescales confirm that flame stabilization away from the shear layers is a result of premixed flame propagation. These timescales also suggest that the lean flame is more coupled with the shear layer, because of its slower propagation speed.

Computational analyses were also performed to examine if dilatation can accurately be used as a marker for heat release. In the JICF experimental results it was shown that there was generally good agreement between heat release and dilatation when the flame resided away from the shear layer. However, when the flame stabilized in the shear layer the dilatation was not representative of the heat release. Computational analyses were first conducted for a one-dimensional premixed flame, which confirmed that both thermal diffusion effects and heat release contribution to dilatation in reacting flows. The dilatation aligned spatially with the temperature gradient; however at low flame strain conditions dilatation and heat release decay were proportional. At higher flame strain conditions, the increase in temperature gradient (and subsequent thermal diffusion) dominated the effects of heat release

such that heat release and dilatation were no longer proportional. Overall, high strain led to a decrease in peak dilatation compared to the unstretched laminar flame condition. At high jet dilution levels, where auto-ignition time scales were fastest, dilatation and heat release were proportional; as temperature gradients were very low. Peak dilatation in these highly diluted mixtures was greatly reduced, relative to the undiluted jet reactant mixture. In the experiment, strain-rate and reactant dilution was high when the flame stabilized in the shear layer, and as a result the dilatation caused by combustion is low. In the windward region, the low dilatation generated by combustion was dominated by strong out-of-plane flow effects which resulted in negative dilatation.

## 6.2 Future Work

Suggestions for future work on the premixed JICF configuration are divided into two sections: suggestions for future experimental measurements on the existing configuration and suggestions for future studies of different experimental parameters.

### *6.2.1 Additional Measurements*

- The simplest measurements that could be taken to improve the premixed JICF analysis are full field of view simultaneous $CH_2O$, OH, and PIV measurements. In the work conducted for this dissertation, laser scatter off the test section floor did not allow for PLIF measurements close to the jet exit. Though the PLIF ROI used was well within the region where auto-ignition kernels were observed, it would still be beneficial to have imaging closer to the jet exit. Full field of view images would also allow for simultaneous imaging of the windward flame branch and leeward flame branch. These images would be useful for analysis of behavior near the flame tip.
- Further understanding of the jet flame stabilization behavior could be accomplished by obtaining measurements of the local mixing behavior between the jet reactants and crossflow fluid. Such measurements would help to determine how different *J* values affect the jet and crossflow

mixing prior to combustion. Additionally, quantification of local mixtures would help to determine what mixture conditions lead to auto-ignition. These measurements would be useful for comparing with the computational auto-ignition analysis.

- Dual-plane PIV measurements would also be useful for the premixed JCIF experiment. Characterization of the out-of-plane flow behavior along the jet centerline would allow for a more detailed analysis of the dilatation generated by the reacting flame. These measurements would provide a useful counterpart to the computational analysis performed for analysis of dilatation as a marker for heat release.

### *6.2.2 Flame Stabilization Experiments*

The novelty of the premixed JICF means that there are still many different experiments that would make for useful investigations. Some of these ideas include:

- Characterization of the flame stability limits. In this thesis one lean, one rich, and stoichiometric jet conditions were examined. Investigation of the JICF flame stability limits could be conducted by decreasing equivalence ratio beyond 0.8 to determine the equivalence ratio at which flame stabilization is no longer possible. In addition, characterization of the flame stabilization location at these leaner jet equivalence ratios would be useful for understanding LPM combustion behavior.
- Varying jet turbulence intensity to determine how auto-ignition and flame propagation behavior are affected. It is possible that increased mixing between jet and crossflow as a result of increased turbulence would assist in flame anchoring. Similarly, turbulence intensity could improve the propagation characteristics when the flame resides away from the shear layer. It would be interesting to determine if, at high turbulence levels, local flame extinction events occur.

- Examination of jets with higher inlet temperature. Preliminary results, not presented in this thesis, suggest that increasing jet inlet temperature can significantly decrease flame propagation timescales, while minimally affecting ignition delay time, from the jet ambient conditions. Thus, heated jet conditions would help to isolate the effect of propagation speed on flame stabilization.

# References


[1] M.J. Foust, D. Thomsen, R. Stickles, C. Cooper, W. Dodds, "Development of the GE Aviation Low Emissions TAPS Combustor for Next Generation Aircraft Engines", *50th AIAA Aerosp. Sci. Meet. Incl. New Horizons Forum Aerosp. Expo.* Nashville, Tennessee, January 2012, Paper No. AIAA 2012-0936.

[2] S. Samuelsen, "Rich Burn, Quick-Mix, Lean Burn (RQL) Combustor." *The Gas Turbine Handbook*, National Energy Technology Laboratory, pp. 227–233, Retrieved 2016.

[3] W. R. Bender, "Lean Pre-Mixed Combustion." *The Gas Turbine Handbook*, National Energy Tchnology Laboratory, pp. 217–227, Retrieved 2016.

[4] A. R. Karagozian, *Prog. Energy Combust. Sci.*, vol. 36, no. 5, pp. 531–553, 2010.

[5] R. J. Margason, "Fifty Years of Jet in Cross Flow Research," AGARD Computational and Experimental Assessment of Jets in Cross Flow (1993) 41.

[6] T.F. Fric, A. Roshko, *J. Fluid Mech*. 279 (1994) 1-47.

[7] K.E. Meyer, J.M. Pedersen, O. Ozcan, *J. Fluid Mech*. 583 (2007) 199-227.

[8] J. A. Wagner, S. W. Grib, M. W. Renfro, B. M. Cetegen, *Combust. Flame*, vol. 162, no. 10, pp. 3711–3727, 2015.

[9] W. D. Pratte, B. D. Baines, *J. Hydraul. Div. Proc. Am. Soc. Civ. Eng.*, vol. 93, no. 6, pp. 53–64, 1967.

[10] E.F. Hasselbrink, M.G. Mungal, *J. Fluid Mech.* 443 (2001) 1-25.

[11] Y. Kamotani, I. Greber, *AIAA Journal* 10 (1972) 1425-1429.

[12] Y. Kamotani, I Greber, "Experiments on Confined Turbulent Jets in Cross Flow," *NASA CR-2392* (1974).

[13] R. Kee, J. Grcar, M. Smooke, J. Miller, E. Meeks, "PREMIX : A FORTRAN Program for Modeling Steady Laminar One-Dimensional," *Sandia National Laboratories: Livermore.* pp. 85–8240, 1985.

[14] H. Wang, X. You, A. V. Joshi, S. G. Davis, A. Laskin, F. Egolfopoulos. C. K. Law, USC Mech Version II. High-Temperature Combustion. Reaction Model of H2/CO/C1-C4 Compounds. http://ignis.usc.edu/USC_Mech_II.htm, May 2007.

[15] C. K. Law, Combustion Physics, Cambridge University Press, New York, NY, 2006.

[16] C. K. Law, C. J. Sung, *Prog. Energy Combust. Sci.*, vol. 26, no. 4, pp. 459–505, 2000.

[17] S. M. Candel, T. J. Poinsot, *Combust. Sci. Tech.*, vol. 70, no. 1-3, pp. 1-15, 1990

[18] A. M. Steinberg, J. F. Driscoll, *Combust. Flame*, vol. 156, no. 12, pp. 2285–2306, 2009.

[19] S. Chaudhuri, S. Kostka, M. W. Renfro, B. M. Cetegen, *Combust. Flame*, vol. 157, no. 4, pp. 790–802, 2010.

[20] S. G. Tuttle, S. Chaudhuri, S. Kostka, K. M. Kopp-Vaughan, T. R. Jensen, B. M. Cetegen, M. W. Renfro, *Combust. Flame*, vol. 159, no. 1, pp. 291–305, 2012.

[21] E. Mastorakos, *Prog. Energy Combust. Sci.*, vol. 35, no. 1, pp. 57–97, 2009.

[22] R. L. Gordon, A. R. Masri, E. Mastorakos, *Combust. Flame*, vol. 155, no. 1–2, pp. 181–195, 2008.

[23] C. M. Arndt, J. D. Gounder, W. Meier, M. Aigner, *Appl. Phys. B Lasers Opt.*, vol. 108, no. 2, pp. 407–417, 2012.

[24] J. Fleck, P. Griebel, A. M. Steinberg, M. Stöhr, M. Aigner, A. Ciani, *J. Eng. Gas Turbines Power*, vol. 134, no. 4, p. 041502, 2012.

[25] A. Schönborn, P. Sayad, A. A. Konnov, J. Klingmann, *Combust. Flame*, vol. 160, no. 6, pp. 1033–1043, 2013.

[26] H. G. Im, J. H. Chen, C. K. Law, *Symp. Combust.*, vol. 27, no. 1, pp. 1047–1056, 1998.

[27] E. Mastorakos, T. A. Baritaud, T. J. Poinsot, *Combust. Flame*, vol. 109, no. 96, pp. 198–223, 1997.

[28] R. Cabra, J. Y. Chen, R. W. Dibble, A. N. Karpetis, R. S. Barlow, *Combust. Flame*, vol. 143, no. 4, pp. 491–506, 2005.

[29] R. Cabra, T. Myhrvold, J. Y. Chen, R. W. Dibble, A N. Karpetis, R. S. Barlow, *Proc. Combust. Inst.* vol. 29, pp. 1881–1888, 2002.

[30] P. R. Medwell, P. A. M. Kalt, B. B. Dally, *Combust. Flame*, vol. 152, no. 1–2, pp. 100–113, 2008.

[31] M. J. Dunn, A. R. Masri, R. W. Bilger, "Lifted Turbulent Premixed flames issuing into a hot coflow, imaging of temperature and OH," *Proc. of the 16th Australasian Fluid Mechanics Conference*, December 2007, paper no. 16AFMC.

[32] K. A. Ahmed, D. J. Forliti "On the Flame and Vorticity Characteristics of a Fluidically Stabilized Premixed Turbulent Flame" *48th AIAA Aerospace Sciences Meeting Including the New Horizons Forum and Aerospace Exposition*, Orlando, Florida, January 2010, paper no. AIAA 2010-1522.

[33] R. V. Bandaru, S. R. Turns, *Combust. Flame*, vol. 121, no. 1–2, pp. 137–151, 2000.

[34] M. Boutazakhti, M. J. Thomson, M. Lightstone, *Combust. Sci. Technol.*, vol. 163, no. 1, pp. 211–228, 2001.

[35] J. M. Fleck, P. Griebel, A. M. Steinberg, C. M. Arndt, C. Naumann, M. Aigner, *Proc. Combust. Inst.*, vol. 34, no. 2, pp. 3185–3192, 2013.

[36] J. D. Holdeman C. T. Chang, *J. Fluids Eng.*, vol. 129, no. 11, p. 1460, 2007.

[37] J. D. Leong, M.Y. Samuleson, G.S. Holdeman, *J. Propuls. Power*, vol. 16, no. 5, pp. 729–735, 2000.

[38] K. C. Marr, N. T. Clemens, and O. A. Ezekoye, *Combust. Flame*, vol. 159, no. 2, pp. 707–721, 2012.

[39] D. J. Micka and J. F. Driscoll, *Combust. Flame*, vol. 159, no. 3, pp. 1205–1214, 2012.

[40] P. P. Panda, M. Roa, C. D. Slabaugh, S. Peltier, C. D. Carter, W. R. Laster, R. P. Lucht, *Combust. Flame*, vol. 163, pp. 241–257, 2016.

[41] B. Popovic, M. J. Thomson, M. F. Lightstone, *Combust. Sci. Technol.*, vol. 155, pp. 31–49, 2000.

[42] M. Roa, W. G. Lamont, S. E. Meyer, P. Szedlacsek, R. P. Lucht, "Emission Measurements and

OH-PLIF of Reacting Hydrogen Jets in Vitiated Crossflow for Stationary Gas Turbines," *Proceedings of the ASME Turbo Expo*, Copenhagen, Denmark, June 2012, paper no. GT2012-68711.

[43] J. Sidey, E. Mastorakos, *Proc. Combust. Inst.*, vol. 35, no. 3, pp. 3537–3545, 2014.

[44] Q. Wang, L. Hu, S. H. Yoon, S. Lu, M. Delichatsios, S. H. Chung, *Combust. Flame*, vol. 000, pp. 1–7, 2015.

[45] R. Sullivan, B. Wilde, D. R. Noble, J. M. Seitzman, T. C. Lieuwen, *Combust. Flame*, vol. 161, no. 7, pp. 1792–1803, 2014.

[46] A. M. Steinberg, R. Sadanandan, C. Demb, P. Kutne, W. Meier, *Proc. Combust. Inst.*, vol. 34, no. 1, pp. 1499–1507, 2013.

[47] D. Han, M. G. Mungal, *Combust. Flame*, vol. 133, no. 1–2, pp. 1–17, 2003.

[48] E. F. Hasselbrink, M. G. Mungal, *J. Fluid Mech.*, vol. 443, pp. 27–68, 2001.

[49] E. F. Hasselbrink, M. G. Mungal, R. K. Hanson, *J. Vis.*, vol. 1, no. 1, pp. 65–77, 1998.

[50] R. W. Grout, A. Gruber, C. S. Yoo, J. H. Chen, *Proc. Combust. Inst.*, vol. 33, no. 1, pp. 1629–1637, 2011.

[51] H. Kolla, R. W. Grout, A. Gruber, J. H. Chen, *Combust. Flame*, vol. 159, no. 8, pp. 2755–2766, 2012.

[52] D. Schmitt, M. Kolb, J. Weinzierl, C. Hirsch, T. Sattelmayer, "Ignition and Flame Stabilization of a Premixed Jet in Hot Cross Flow," *Proceedings of the ASME Turbo Expo*, San Antonio, Texas, June 2013, paper no. GT2013-94763.

[53] M. Kolb, D. Ahrens, C. Hirsch, T. Sattelmayer, "A Model for Predicting the Lift-Off Height of Premixed Jets in Vitiated Cross Flow," *Proceedings of the ASME Turbo Expo*, Montreal, Canada June 2015, paper no. GT2015-42225.

[54] H. N. Najm, P. H. Paul, C. J. Mueller, P. S. Wyckoff, *Combust. Flame*, vol. 113, pp. 312–332, 1998.

[55] P. H. Paul, H. N. Najm, *Symp. Combust.*, vol. 27, no. 1, pp. 43–50, 1998.

[56] Z. S. Li, B. Li, Z. W. Sun, X. S. Bai, M. Alden, *Combust. Flame*, vol. 157, no. 6, pp. 1087–1096, 2010.

[57] T. M. Wabel, A. W. Skiba, J. E. Temme, J. F. Driscoll, "Measurements of Premixed Turbulent Combustion Regimes of High Reynolds Number Flames," *AIAA Aerospace Sciences Meeting*, Kissimmee, Florida, January 2015, paper no. 0168.

[58] P. R. Medwell, D. L. Blunck, B. B. Dally, *Combust. Flame*, vol. 161, no. 2, pp. 465–474, 2014.

[59] G. M. Lapaan, "Flow Field And Mixing Characteristics of Multiple Reacting Jets In Vitiated Crossflow Flow Field And Mixing Characteristics Of Multiple Reacting Jets In Vitiated Crossflow," Masters Thesis, UCONN, Storrs, CT, 2014.

[60] S. G. Tuttle, "Blowoff Behavior of Bluff Body Stabilized Flames in Vitiated and Partially Premixed Flows," Ph.D. Dissertation, UCONN, Storrs, CT, 2010.

[61] M. G. Mungal, L. M. Lourenco, A. Krothapalli, *Combust. Sci. and Tech.*, vol. 106, pp. 239-265, 1995.

[62] C. J. Mueller, J. F. Driscoll, D. L. Reuss, M. C. Drake, *Symp. Combust.*, vol. 26, no. 1, pp. 347–

355, 1996.

[63] H. Malm, G. Sparr, J. Hult, C. F. Kaminski, *J. Opt. Soc. Am. A. Opt. Image Sci. Vis.*, vol. 17, no. 12, pp. 2148–2156, 2000.

[64] J. Kariuki, A. Dowlut, R. Yuan, R. Balachandran, E. Mastorakos, *Proc. Combust. Inst.*, vol. 35, no. 2, pp. 1443–1450, 2015.

[65] D. Han, M. G. Mungal, *Combust. Flame*, vol. 124, no. 3, pp. 370–386, 2001.

[66] N. T. Clemens, P. H. Paul, *Combust. Flame*, vol. 102, no. 3, pp. 271–284, 1995.

[67] L. K. Su, O. S. Sun, M. G. Mungal, *Combust. Flame*, vol. 144, no. 3, pp. 494–512, 2006.

[68] S. Lyra, B. Wilde, H. Kolla, J. M. Seitzman, T. C. Lieuwen, J. H. Chen, *Combust. Flame*, vol. 162, no. 4, pp. 1234–1248, 2015.

[69] S. H. Smith, M. G. Mungal, *J. Fluid Mech.*, vol. 357, pp. 83–122, 1998.

[70] S. G. Tuttle, S. Chaudhuri, K. M. Kopp-Vaughan, T. R. Jensen, B. M. Cetegen, M. W. Renfro, J. M. Cohen, *Combust. Flame*, vol. 160, no. 9, pp. 1677–1692, 2013.

[71] V. Giovangigli, M. D. Smooke, *J. Comp. Phys.*, pp. 327–345, 1987.

[72] S. R. Turns, An Introduction To Combustion: Concepts and Applications, McGraw-Hill, Boston, MA, 2000.

[73] A. Upatnieks, J. F. Driscoll, C. C. Rasmussen, S. L. Ceccio, *Combust. Flame*, vol. 138, no. 3, pp. 259–272, 2004.

[74] J. F. Driscoll, *Prog. Energy Combust. Sci.*, vol. 34, no. 1, pp. 91–134, 2008.

[75] C. S. Panoutsos, Y. Hardalupas, A. M. K. P. Taylor, *Combust. Flame*, vol. 156, no. 2, pp. 273–291, 2009.

[76] R. J. Kee, J. A. Miller, G. H. Evans, *Symp. Combust*, vol. 22, no. 1, pp. 1479-1494, 1989.

[77] D.R. Burgess, "Thermochemical Data" in NIST Chemistry WebBook, NIST Standard Reference Database Number 69, Eds. P.J. Linstrom and W.G. Mallard, *National Institute of Standards and Technology*, Gaithersburg MD, 20899, http://webbook.nist.gov, (retrieved April 3, 2016).

[78] T. F. Lu, C. S. Yoo, J. H. Chen, C. K. Law, *J. Fluid Mech.*, vol. 652, pp. 45–64, 2010.